

Structural and Excited State Dynamics in Hybrid Halide Perovskites

Fridriksson, M.B.

DOI

[10.4233/uuid:4d48181b-5429-4bef-976d-95b6c9535825](https://doi.org/10.4233/uuid:4d48181b-5429-4bef-976d-95b6c9535825)

Publication date

2020

Document Version

Final published version

Citation (APA)

Fridriksson, M. B. (2020). *Structural and Excited State Dynamics in Hybrid Halide Perovskites*. [Dissertation (TU Delft), Delft University of Technology]. <https://doi.org/10.4233/uuid:4d48181b-5429-4bef-976d-95b6c9535825>

Important note

To cite this publication, please use the final published version (if applicable).
Please check the document version above.

Copyright

Other than for strictly personal use, it is not permitted to download, forward or distribute the text or part of it, without the consent of the author(s) and/or copyright holder(s), unless the work is under an open content license such as Creative Commons.

Takedown policy

Please contact us and provide details if you believe this document breaches copyrights.
We will remove access to the work immediately and investigate your claim.

Structural and Excited State Dynamics in Hybrid Halide Perovskites

Magnús Borgar Friðriksson

Structural and Excited State Dynamics in Hybrid Halide Perovskites

Dissertation

for the purpose of obtaining the degree of doctor
at Delft University of Technology
by the authority of the Rector Magnificus *Prof. dr.ir. T. H. J. J. van der Hagen*;
Chair of the Board for Doctorates

to be defended publicly on
Monday 11th of January 2021 at 10:00 o'clock

by
Magnús Borgar FRÍÐRIKSSON

*Chemical engineer
Delft University of Technology
born in Reykjavík, Iceland*

This dissertation has been approved by the promotor.

Prof. dr. F. C. Grozema
Prof. dr. A. J. Houtepen

Delft University of Technology, promotor
Delft University of Technology, promotor

Composition of the doctoral committee:

Rector Magnificus,
Prof. dr. F. C. Grozema
Prof. dr. A. J. Houtepen

chairperson
Delft University of Technology, promotor
Delft University of Technology, promotor

Independent members:

Prof. dr. U. Röthlisberger

École Polytechnique Fédérale de Lausanne,
Switzerland

Dr. L. Leppert

University of Twente

Prof. dr. ir. J. M. Thijssen

Delft University of Technology

Prof. dr. P. Dorenbos

Delft University of Technology

Prof. dr. J. H. van Esch

Delft University of Technology

This work received financial support from the European Research
Council Horizon 2020 ERC Grant Agreement No. 648433

ISBN: 978-94-6332-718-3

Copyright © 2020 Magnús Borgar Friðriksson

Printed by GVO drukkers & vormgevers B.V.

An electronic version of this thesis is freely available at

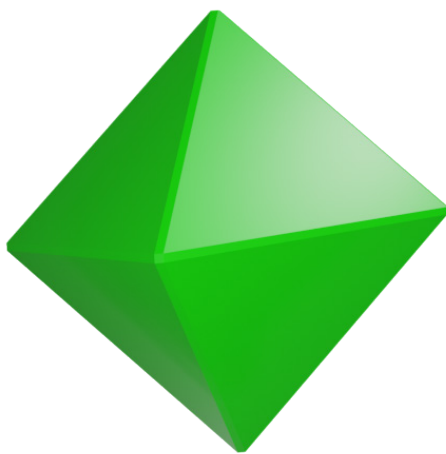
<http://repository.tudelft.nl>

Table of Contents

Chapter 1 - Introduction	1
Chapter 2 - The Relation Between Rotational Dynamics of the Organic Cation and Phase Transitions in Hybrid Halide Perovskites	19
Chapter 3 - Structural Dynamics of Two-Dimensional Ruddlesden-Popper Perovskites: A Computational Study	45
Chapter 4 - Tuning the Structural Rigidity of 2D Ruddlesden-Popper Perovskites Through the Organic Cation	67
Chapter 5 - Trapping and De-Trapping in Colloidal Perovskite Nanoplatelets: Elucidation and Prevention of Non-Radiative Processes Through Chemical Treatment	91
Summary	117
Samenvatting	121
Acknowledgements	125
List of Publications	129
Curriculum Vitae	131

1

Introduction



1

Perovskites are a class of materials that share a name and a crystal structure with the mineral CaTiO_3 , which was discovered in 1839. In 2009 it was first reported that metal-halide perovskite materials could be used as the light-harvesting material in dye sensitized solar cells.¹ In the decade that followed, metal-halide perovskite have become one of the hottest topic in solar-cell research²⁻³ as well as for other semiconductor applications such as light emitting diodes,⁴ Lasers⁵ and x-ray detectors.⁶ In the same time thin film solar cells have replaced dye sensitized solar cells as the design of choice for metal-halide perovskites and the efficiency has risen from 3.8% in 2009¹ to 25.2% in 2020.⁷ That is close to what is achievable with single crystal silicon cells. There are several properties that make perovskites as efficient light absorbers as they are, for instance high absorption coefficient, high tolerance to defects, high static dielectric constant, high charge carrier mobility along with long lifetime and long diffusion length of the charge carriers.⁸⁻¹⁰

The obstacles that remain for perovskite solar cells lie in their environmental instability and the toxicity of lead which is present in majority of metal-halide solar cells. A lot of attention has been allocated to these problems. For instance, in the case of the toxicity problem researcher have tried to substitute lead with tin¹¹ or by a mixture of two different cations for instance silver and bismuth, resulting in so called double-perovskites.¹² To tackle the environmental instability problem many different approaches have been explored, including encapsulating the material to protect from air and moisture.¹³ However, another approach is to make a layered two-dimensional (2D) perovskite structure with large organic cations that protect the inorganic layer,¹⁴ these two-dimensional structures will be discussed in more detail later in this chapter.

1.1 Structure of three-dimensional metal halide perovskites

The general structural formula for perovskites is given by ABX_3 , where A is a monovalent cation, B is a divalent cation and X is a monovalent anion. The crystal structure is characterized by an arrangement of corner-sharing $[\text{BX}_6]^{4-}$ octahedra forming an inorganic lattice. The A-cations occupy the spaces formed by eight neighboring octahedra, as is shown in Figure 1.1. This means that there are strict size-requirements for the A-site cation in order to fit inside the structure, which are described by Goldsmith's tolerance factor (Equation 1.1).¹⁵ In Equation 1.1 r_A , r_B and r_X are the ionic radii of the A, B and X ions respectively and t is a dimensionless number. If t is larger than 1 the A cation is too large for the space in-between the octahedra and a stable three-dimensional (3D) perovskite structure cannot be formed. In practice, because of these size-limitations, the choice of the A cation is very limited in three-dimensional perovskites. In fully inorganic halide perovskites usually a Cs^+ is incorporated, while in hybrid organic/inorganic perovskites the small A-cation is usually either methylammonium (MA) or formamidinium (FA). For the B-cation, Pb^{2+} is the most common choice as the most efficient solar cells included lead-based hybrid perovskites. The X anion is usually a halide, either I⁻, Br⁻ or Cl⁻.

$$t = \frac{r_A + r_X}{\sqrt{2}(r_B + r_X)} \quad 1.1$$

Perovskites usually deviate from the ideal cubic structure depicted in Figure 1.1, where the octahedral tilting angles can deviate. The phase behavior of several perovskites has

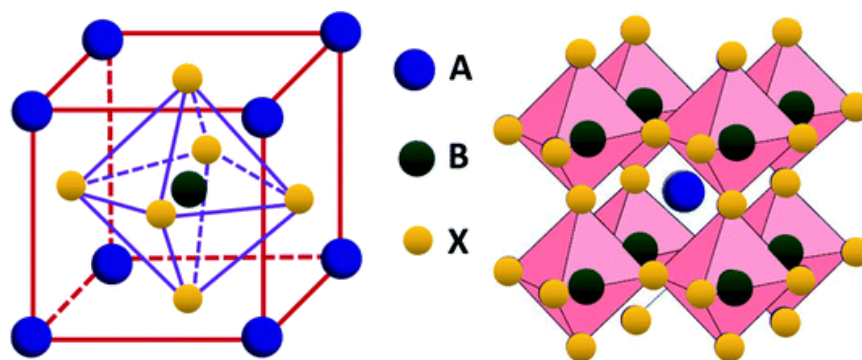


Figure 1.1. The perovskite crystal structure. Reproduced with permission from ref.¹⁶ Published by The Royal Society of Chemistry.

been very well characterized. For example, for MAPbI_3 the (average) structure is cubic at high temperature (> 327 K), but becomes tetragonal at room temperature, while an orthorhombic structure is obtained at low temperatures (< 162 K).¹⁷ These structural phase transitions keep the overall corner-shared structure intact, but the geometric deviations have important implications for the electronic properties.¹⁸ An interesting aspect of these phase transitions is that they can be accompanied by substantial changes in the rotational freedom of the A-cation. In MAPbI_3 the MA cation can rotate more or less freely at room temperature and above, however at temperatures below the phase transition to the orthorhombic structure the orientation becomes fixed.¹⁷ The structure and dynamics of three-dimensional perovskites are discussed in detail in Chapter 2 of this thesis where molecular dynamics simulations on MAPbI_3 and FAPbI_3 are reported.

1.2 Structure of two-dimensional metal halide perovskites

As mentioned above, the size requirements imposed by Goldsmith's tolerance factor severely limit the range of A-site cations that can be included to obtain a lattice of three dimensionally connected $[\text{BX}_6]^{4-}$ octahedra. However, it has been shown that the inclusion of much larger organic cations, such as butylammonium is possible, leading to the formation of two-dimensional layers of corner-shared octahedra, separated by layers of the organic cations, as shown in Figure 1.2.¹⁹ In addition, it is possible to only replace a fraction of the small (organic) cation by large organic cations, which leads to multi-layered structures where multiple layers of $[\text{BX}_6]^{4-}$ octahedra are separated by the large organic cations, see Figure 1.2.²⁰ The general chemical structure formula for these materials becomes $\text{L}_2\text{A}_{n-1}\text{B}_n\text{X}_{3n+1}$, where L is the large organic cation containing an ammonium group to attach to the inorganic layers. In the majority of studies on two-dimensional perovskites, the large organic cation is either butylammonium (BA) or phenylethylammonium (PEA). 2D perovskites with a variety of larger organic cations have also been synthesized, including longer aliphatic chains such as hexyl- and octylammonium²¹⁻²³ and large conjugated molecules.²⁴⁻²⁷ Examples of molecules that have been employed as the L-type cation in 2D perovskites are shown in Figure 1.3.

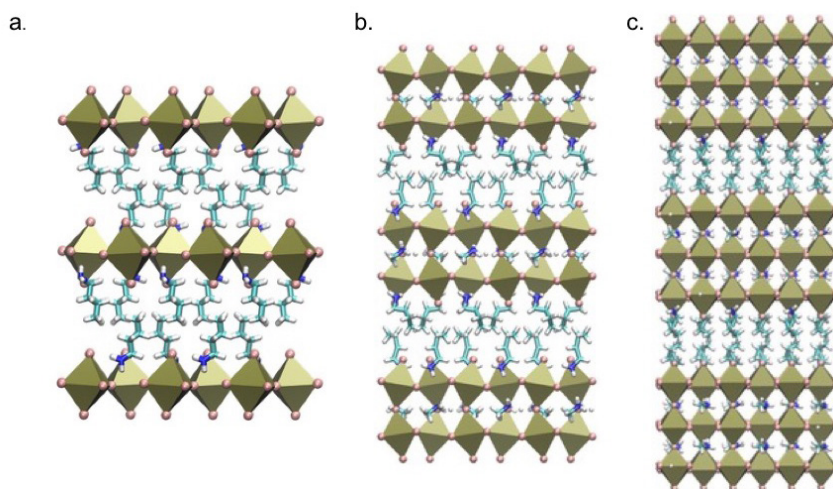


Figure 1.2 Structure of two-dimensional perovskites with varying number of inorganic octahedra layers. (a) One layer of octahedra, $n = 1$. (b) Two layers of octahedra, $n = 2$. (c) Three layers of octahedra, $n = 3$.

An interesting feature of 2D hybrid perovskites is the high tunability of their chemical and physical properties. This can be achieved by exchanging the large organic cation, by exchanging the halogen²⁸ or by introducing both large and small organic cations and controlling the thickness of $[A_{n-1}B_nX_{3n+1}]^{2-}$ slabs through the value of n .²⁹⁻³⁴ Adjusting these factors has a large effect on the electronic properties of the materials, as is discussed in the next session. It has also been shown that larger aromatic organic cations protect the inorganic perovskite layer better from air and moisture than smaller aliphatic ones.²⁴

Thin films of 2D perovskites are solution-processable and exhibit a higher stability than 3D perovskites under ambient conditions.^{31, 34} Highly efficient solar cells (PCE of 12.5%)³⁵ and LEDs³⁶ (EQE of 8.8%) have been reported recently. They also offer the possibility of combining the higher efficiency of the 3D perovskite and the increased environmental stability of the 2D perovskite through tandem solar cells.³⁷ The 3D perovskite is then responsible for majority of the light absorption while the 2D perovskite is placed on the top of the absorbing layer protecting it from air and moisture. The structure and dynamics of two-dimensional perovskites is discussed in Chapters 3 and 4 where molecular dynamics simulations are performed on perovskites with varying value of n and different large organic cations.

1.3 Electronic properties

The band structure of halide perovskite materials is complicated and there are several fundamental aspects that have not been unanimously established. For instance, the nature of the band gap, direct versus indirect, is a subject of considerable debate.³⁸ The electronic structure of the most common halide perovskites is almost exclusively determined by the inorganic metal halide framework. For lead halide perovskites the valence band maximum is mainly made up of p-orbitals on the halide, while the conduction band minimum mainly

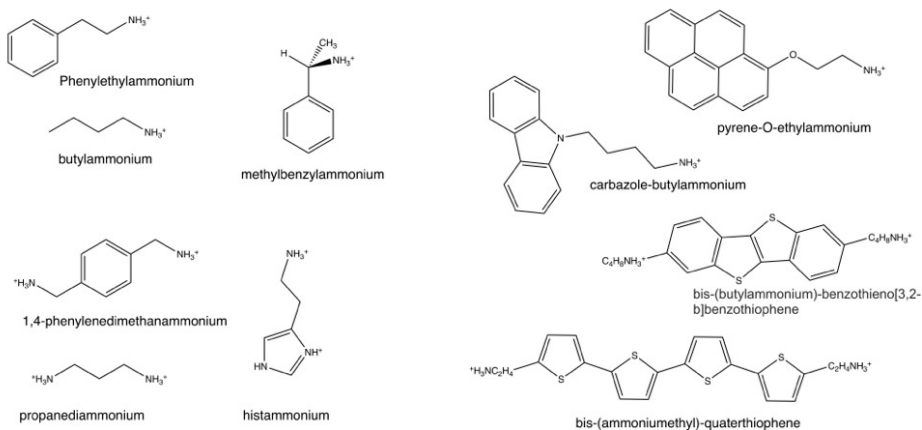


Figure 1.3 Examples of molecules that have been employed as large organic cations in two-dimensional perovskite.

consists of p-orbitals on lead.³⁹ This means that the nature of the halide strongly influences the band gap and hence the electronic properties.⁴⁰ Exchanging the halide from iodide in MAPbI_3 to bromide in MAPbBr_3 leads to a shift in the absorption onset from ~ 800 nm to ~ 550 nm.⁴¹ The A-site cation does not directly affect the electronic structure since its orbitals do not contribute to the valence band maximum and conduction band minimum, but it does have a subtle effect on the structure of the lead halide framework and therefore affect the electronic structure indirectly. For instance, the replacement of MA in MAPbI_3 by the larger formamidinium (FA) results in a shift of the absorption onset to ~ 837 nm,¹⁷ while replacing it by the smaller Cs^+ leads to an opposite shift to shorter wavelengths (~ 742 nm).¹⁷ The strong effect of the nature of the halide on the electronic structure results in a very wide band gap tunability by making so-called mixed halide perovskites in which the bandgap can be almost continuously tuned between the band gaps of the pure-halide materials.^{41–42}

An additional handle to tune the electronic properties, apart from this compositional tuning, is the tuning of the dimensionality. Formation of layered two-dimensional structures results in inorganic metal-halide layers that are separated by layers of large organic cations that generally do not contribute to the electronic properties. These materials were extensively studied in the 1990s for their unique quantum-well structure that enhances exciton confinement beyond predictions for ‘classical’ 2D systems.^{43–44} This additional confinement has been attributed to the large difference between the dielectric constants of the large organic “barrier” (~ 2) and the inorganic “well” (~ 10).^{43, 45–48} The spatial and dielectric confinement results in a much larger band gap than for the three-dimensional analogues, for instance the two-dimensional lead halide perovskite BA_2PbI_4 has a band gap of 2.24 eV,³¹ compared to 1.53 eV for the three-dimensional material. The quantum confinement also has direct consequences for the nature of the excited states in the material. In three-dimensional halide perovskites photoexcitation directly results in the formation of free charges as a result of the very low exciton binding

energy for which estimates range from a few to a few tens of meV. For two-dimensional materials the exciton binding energies are much larger, typically a few hundreds of meVs. This leads to the generation of bound and long-lived (Wannier-Mott) excitons, which renders these materials good candidates for photo-luminescent applications such as lasers and light emitting diodes (LDs and LEDs),⁴⁹⁻⁵⁰ nonlinear optical⁵¹ and polaritonic devices.⁵²⁻⁵⁶ However, in many cases they exhibit inefficient luminescence at room temperature possibly due to thermal quenching of the excitons or strong exciton-phonon interactions.^{36, 57-61} As discussed above, combining the small A-type and the large L-type cations in appropriate ratios can lead to the formation multi-layer structures. It has been shown that the band-gap of the material is very sensitive to the thickness of the inorganic layers between the organic 'spacer' layers.^{28, 31} It was shown in a recent study that also the exciton binding energy can be tuned over a large range by varying this thickness.⁶² This results in strongly bound excitons at room temperature for the pure 2D material ($E_b = 370$ meV), and almost complete formation of free charges for materials with 4 inorganic layers between the organic layers. Such multi-layer structures have been used in devices such as solar cells (with an efficiency up to 12.5%)³⁵ and LEDs³⁶ (EQE of 8.8%) have been reported recently. These devices were based on 2D perovskites with butylammonium and phenylethylammonium as the bulky organic cations, respectively.

1.4 Effect of organic component on the structure of the inorganic part

In the large majority of work on two-dimensional halide perovskites the organic layer does not contribute to the electronic structure direct since the valence and conduction band edges are exclusively made up of orbital on the inorganic part. However, as is clear from the replacement of MA by FA in three-dimensional perovskites, there are pronounced indirect effects of the large organic cation on the electronic structure. For two-dimensional perovskites these effects are a direct consequence of the structure of the L-type cation, which determine the intermolecular interactions in the organic layer. All L-type cations that have been considered contain an ammonium group that anchors them to the inorganic framework. This ammonium group partially enters the inorganic layer and takes the position that is occupied by the A-type cation in three-dimensional structures. However, the shape and steric requirements of the organic part that is attached to the ammonium influences for instance to what extent the ammonium can enter the space between the metal-halide octahedra. This positioning of the ammonium with respect to the inorganic layer has a direct effect on the structure of the inorganic layer as it influences the twisting angles of the neighboring inorganic octahedra. A more pronounced penetration of the ammonium into the inorganic layer was shown to lead to a more cubic structure.⁶³ Through these structural effects, the organic cation indirectly affects the electronic properties as they are strongly dependent on the octahedral twisting angles.⁶⁴

The effect of the organic cation on the inorganic framework is substantially influenced by the dynamics of the material as a whole. In the case of non-functional organic cations such as linear alkyl chains the organic layer is rather 'soft', leading to a large degree of structural disorder in the organic layer, which indirectly results in distortions in the inorganic layers.²⁰ The effect of the softness of the alkylammonium layers results in a complicated phase behavior of some two-dimensional perovskites, with pronounced

changes in the structure and hence the electronic properties.^{21, 65} The extent to which the organic layer induces static and dynamic distortions in the inorganic layer is related to the structural rigidity of the inorganic layer itself. As is discussed in Chapter 3, multi-layer two-dimensional perovskites lead to an enhanced rigidity of the inorganic layers, which diminishes the effect of the organic component on the structure.

The structure and rigidity of the organic layer are to a large extent determined by intermolecular interactions between the organic moieties attached to the ammonium. This introduces a handle to tune the structure and dynamics of the inorganic in a subtle way by changes in the structure of the organic cation. For example, this effect can be expected when the linear alkyl chains are replaced by side chains containing aromatic groups, for instance a phenyl-ring as found in PEA. This introduces the possibility of π - π interactions that can lead to more rigidity in the organic layers, which is transmitted to the inorganic layer that determines the electronic properties. A recent study on the diffusion of excitons in exfoliated two-dimensional perovskites layers revealed that the exciton diffusion length inside the layer is much larger for PEA-based based perovskites than for the BA-based material, which was attributed to a more rigid, ordered structure in the former material.⁶⁶ In Chapter 4 of this thesis the effect of introducing aromatic L-type cations on the structure and dynamics of the inorganic layers is studied in detail by molecular dynamics simulations.

Finally, an interesting recent direction in 2D perovskite research is the introduction of chiral chromophores. In recent studies, it was shown that the introduction of chiral side chains can result in circularly polarized photo-emission without the use of large magnetic fields.⁶⁷ The emission of circularly polarized light originates from the inorganic layers that determine the electronic structure, however, the layer chiral methylbenzylammonium cations transmit their chirality to the organic layers, hence resulting in emission of circularly polarized light. The limited emission efficiencies, up to ~10% are likely to be related to the intrinsically low emission efficiency of pure two-dimensional halide perovskites as a result of the pronounced structural disorder. More recently, it was also shown in conductive probe atomic force microscopy measurements that these two-dimensional chiral hybrid perovskite materials exhibit spin-polarized transport that can be influenced by changing the handedness of the organic molecules.⁶⁸ These examples show that tuning of the structure of the organic cations can introduce new functionality in two-dimensional perovskites in an indirect way due to the relation between the structure of the inorganic framework and the interactions in the inorganic layer.

1.5 Alignment of the inorganic layers

The structure of the organic cation not only affects the internal structure of the inorganic layers but also the mutual alignment of these layers. As discussed above, the intermolecular interactions between the large organic cations directly influence the structure and stability of the inorganic layers. These interactions include the steric requirements related to the packing of the large organic groups from neighboring layers. The most studied two-dimensional perovskites assume a Ruddlesden-Popper (RP) type structure in which a mono-ammonium group attaches to the inorganic layer. In the 'prototype' RP perovskites that contain butylammonium or phenylethylammonium, the steric interactions between

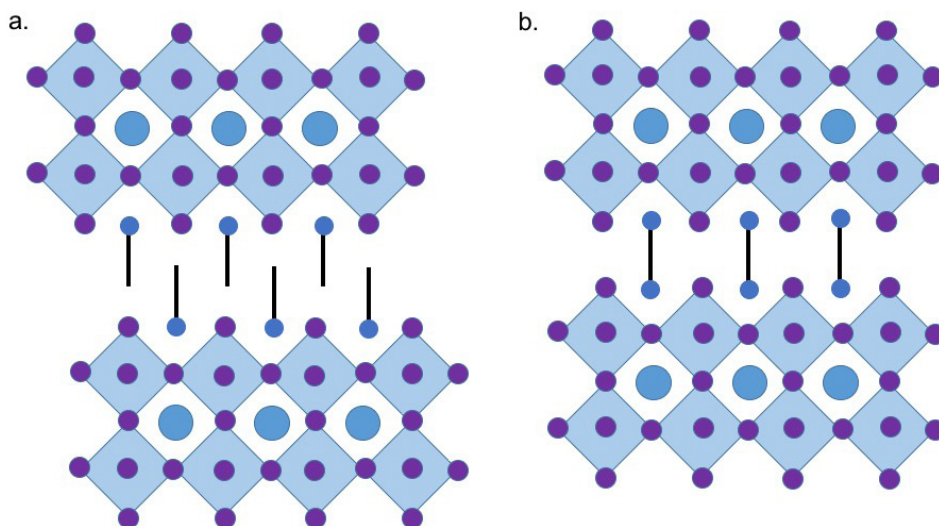


Figure 1.4 Schematic representation of the structure of (a) Ruddlesden-Popper perovskite and (b) Dion-Jacobson perovskite.

the organic moieties lead to a displacement of the inorganic layers by approximately one octahedral unit. This allows the organic chains to avoid each other or to form an interdigitated structure, see Figure 1.4a.

When the monofunctionalized cations are replaced by di-ammonium compounds, these steric requirements are relieved, and the large cation can attach to both of the neighboring inorganic layers. This leads to the formation of so-called Dion-Jacobson (DJ) structures in which the neighboring inorganic layers are stacked on top of each other without an offset, see Figure 1.4b. Due to the bi-functional nature of the organic cation the interlayer interactions do not depend on weak Van der Waals type interactions. The absence of such a Van de Waals gap lead to structures that mechanically more stable, which has been shown to result in significantly more stable solar cell devices, as shown for a propane diamine linker between the inorganic layers.⁶⁹ The DJ structure also affects the electronic properties of the materials. Firstly, the distance between the inorganic layers can be greatly reduced when using bifunctional cations. This leads to an enhanced electronic interaction between the layer, which enhances charge transport in the perpendicular direction. Secondly, the alignment itself also affects the electronic interactions. In RP displaced structure the iodide ion that stick out of the inorganic plane form a staggered conformation, while in the DJ structure they are exactly opposite to each other, leading to enhance electronic interactions.⁶³ It should be noted that a bi-functional by itself is not sufficient for the formation of a DJ structure. If there is a longer flexible linker between the two ammonium groups, there is sufficient freedom for the layers to obtain an offset, and molecular dynamics simulations have indicated that there may even be phase transitions between DJ structures and intermediate RP-DJ structures.⁶³

1.6 Introduction of functional organic chromophores

In the large majority of two-dimensional or quasi-two-dimensional hybrid perovskites studied to date the large organic cations only acts as a spacer, defining the dimensionality of the system. The HOMO-LUMO gap of these organic compounds is generally very large and the electronic properties of the resulting materials are fully determined by the properties of the inorganic layers. However, the organic spacer layer between the inorganic layers offers a lot of freedom to introduce large conjugated chromophores with a much smaller bandgap or with specific functionality. In this way, the electronic states on the of the organic part approach those of the inorganic layers and can have a direct contribution to the electronic structure of the material. In early work on two-dimensional perovskites, a range of more functional conjugated ammonium cations has been explored, most notably by the group of Mitzi, but these studies were largely restricted to structural characterization and basic optical properties.⁷⁰⁻⁷³ In a recent paper by the Mitzi group, short oligothiophenes have been introduced but these only have an indirect impact the electronic structure.⁷⁴

In a recent computational study it was shown that the introduction of conjugated chromophores that are well-known from organic electronics offers a versatile way to influence the electronic properties.²⁶ Introduction of a perylenediimide (PDI) that acts as an electron acceptor leads to a low-lying conduction band located on the PDI molecules, while the highest valence band remains on the inorganic perovskite layer. Alternatively, introduction of a strong conjugated donor (BTBT, Figure 1.3) results in localization of the highest valence band on the organic part, while the lowest conduction band is on the inorganic layer; see Figure 1.5. The energy of the bands on the organic spacer layer and those on inorganic perovskite layers can be tuned independently by modifying the molecular structure of the organic or by changing the thickness of the inorganic layers, respectively. These calculations also show that charge transport perpendicular to the inorganic layers is several orders of magnitude smaller than intra-layer transport for butylammonium spacers. Introduction of chromophores with energy levels close to the conduction band minimum or valence band maximum can significantly enhance the perpendicular transport, as reflected in the effective mass of the charge carriers. Some initial work in this direction was reported in a very recent paper.²⁵

The localization of the valence and conduction band edges in different parts of the materials suggest that interlayer charge separation can occur, if the driving force for charge separation is sufficient. As discussed above, since the exciton binding energy in the thin two-dimensional perovskites is generally very large, very few charges are generated on photoexcitation in the $n = 1$ materials. The engineering of the energy levels in the material in this way can be an approach to strongly enhance the yield of charges formed on photoexcitation. This is beneficial for application of these materials in solar cells or photodetectors where charge separation is an essential first step.

Until date, reports of the formation of long-lived mobile charges resulting from charge transfer between the organic and inorganic parts of the materials are very limited. There a few cases where such charge separation was achieved in colloidal nanoplatelets, showing that long-lived charges actually are formed by time-resolved spectroscopy.^{27, 75-76} In

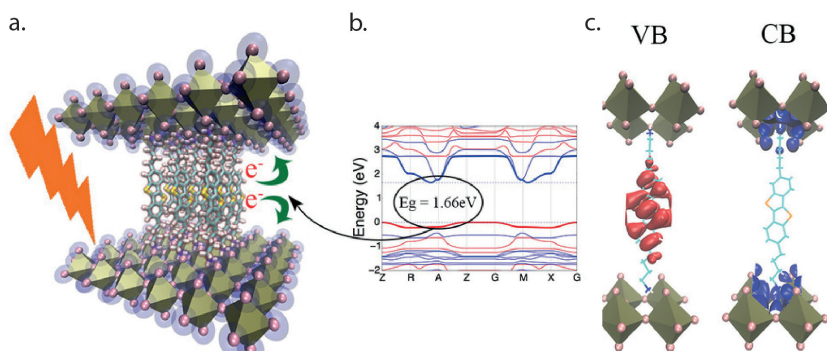


Figure 1.5 (a) Optimized geometry of a 2D lead-iodide-based perovskite where the organic spacer is a conjugated BTBT donor chromophore. Band structure calculations show that the highest valence band is located on the organic part (b) and (c), which may lead to an enhanced probability of charge separation on illumination.

addition, it was demonstrated by time-resolved microwave conductivity experiments that this actually leads to a long-live conductivity signal, indicating that the electron and hole do not form a strongly bound charge-transfer state on the interface.²⁷

The introduction of large organic chromophores in the interlayer region can be taken even further by adding unbound components, for instance very strong electron acceptors such as TCNQ. In this way, it turns out to be possible to incorporate classical organic charge transfer complexes,^{25,77} as shown by specific charge transfer absorption band in the optical absorption spectrum. Apart from the changes in the optical absorption spectrum, it has been shown that this also induces the formation of long-lived charges through microwave conductivity experiments.⁷⁷ These examples show that there are many possibilities to engineer the opto-electronic properties of two-dimensional perovskites if the electronic levels of the organic parts are taken into account.

1.7 Perovskite nanoplatelets

Recently perovskite materials have entered the “nano-world” with synthesis methods for colloidal perovskite nanocrystals and nanoplatelets reported and optimized. Both nanocrystals and nanoplatelets are small crystalline materials where some or all of their dimensions are in the range of a few nanometers. While for nanocrystal all dimensions are on the nano-scale, nanoplatelets are only restricted in one-dimension and form therefore a two-dimensional nano-material. The thickness of the nanoplatelets can be tuned quite easily, which allows synthesis of nanoplatelets with well-defined thickness in the order of few octahedra layers. Because of that, these colloidal perovskite nanoplatelets can be seen as analogous systems to the 2D perovskites discussed in previous sections of this chapter. They have the same general structural formula, $L_2A_{n-1}B_nX_{3n+1}$, the only difference being that now L represents a charged ligand that not only stabilizes the charge of the system but also gives the system colloidal stability and enhances growth of the platelet in the preferred direction.⁷⁸ The fact that perovskite nanoplatelets can be synthesized and kept in a colloidal solution allows often for simpler synthesis and measurements than for the

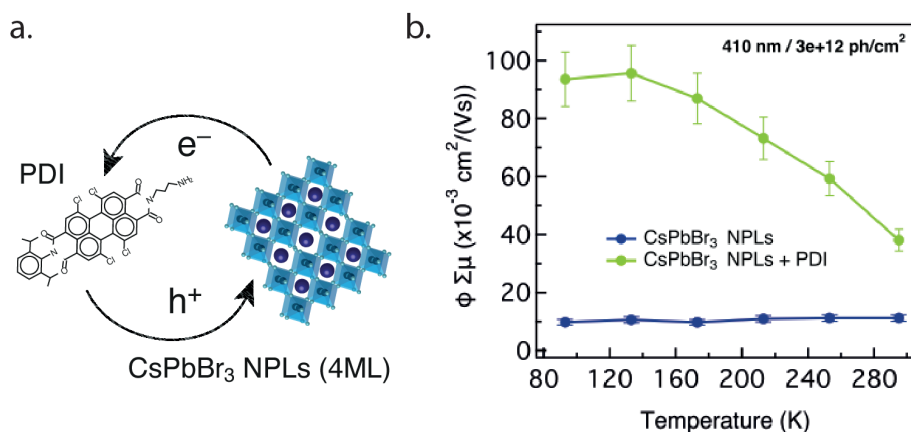


Figure 1.6 (a) Schematic showing the electron and hole transfer occurring between perovskite nanoplalelets and PDI electron acceptors. (b) Maximum photoconductivity as a function of temperature of CsPbBr₃ nanoplalelets and CsPbBr₃ nanoplalelets + PDI hybrid on photoexcitation at 410 nm.

2D perovskite materials. They can therefore be used as model systems for 2D perovskites. Utilized as such we have recently shown that replacing the ligands attached to perovskite nanoplalelets with PDI acceptor molecules it is possible to separate the charges formed when either the PDI molecule or the nanoplalelet is excited. Furthermore, we showed that this separation results in long lived charges (Figure 1.6).²⁷ Similarly other groups have also demonstrated the possibility of performing charge separation in perovskite nanoplalelets using different kind of electron accepting ligands.⁷⁵⁻⁷⁶ In Chapter 5 we look into non-radiative decay pathways of perovskite nanoplalelets. It is important to understand and minimize these non-radiative decay pathways in order to maximize their efficiency in devices such as LEDs.

1.8 Thesis outline

The aim with this thesis is to investigate fundamental properties and processes occurring in perovskite semiconductors, using a combination of computational and spectroscopic methods. These properties include the structure and dynamics of individual parts of the perovskite system at different temperatures, low temperature phase transitions and non-radiative charge-carrier decay pathways. Understanding these properties is important to make it easier to design devices with higher stability and efficiency in the future.

In **Chapter 2** we use molecular dynamics simulations and Monte Carlo simulations to investigate the low temperature phase transition in three dimensional perovskites. We put special emphasis on the relation between slower rotational dynamics of the small organic cations and the deformation of the lead-iodide cage.

In **Chapter 3** we turn our attention to molecular dynamics simulations on two-dimensional perovskites. There we investigate the effect of altering the number of inorganic lead-iodide layers in $\text{BA}_2\text{MA}_{n-1}\text{PbI}_{n-3n+1}$ perovskites on the structure and dynamics of individual parts

of the perovskite system.

In **Chapter 4** we yet again investigate two-dimensional perovskites using molecular dynamics simulations. In this case the number of inorganic layers is kept fixed, at a single layer, while the large organic spacer molecule that separates the layers is altered. The organic molecules tested differ both in their aromaticity as well as the length of their flexible linker. This gives insight into how both aspects affect the dynamics of both the organic molecules as well as the inorganic layer.

Finally, in **Chapter 5** we experimentally investigate the non-radiative charge carrier decay channels in inorganic CsPbBr_3 perovskite nanoplatelets. We use picosecond streak camera measurements as well as nanosecond time-correlated single-photon counting measurements to measure the fluorescence of the platelets over several orders of magnitude in time. We furthermore look at the effect of chemically treating the platelets with additional PbBr_3 .

References

1. Kojima, A.; Teshima, K.; Shirai, Y.; Miyasaka, T., Organometal Halide Perovskites as Visible-Light Sensitizers for Photovoltaic Cells. *J. Am. Chem. Soc.* 2009, 131 (17), 6050-6051.
2. Petrus, M. L.; Schlipf, J.; Li, C.; Gujar, T. P.; Giesbrecht, N.; Müller-Buschbaum, P.; Thelakkat, M.; Bein, T.; Hüttner, S.; Docampo, P., Capturing the Sun: A Review of the Challenges and Perspectives of Perovskite Solar Cells. *Adv. Energy Mater.* 2017, 7 (16), 1700264.
3. Zhaoning, S.; Suneth, C. W.; Adam, B. P.; Michael, J. H., Pathways Toward High-Performance Perovskite Solar Cells: Review of Recent Advances in Organometal Halide Perovskites for Photovoltaic Applications. *J. Photonics Energy* 2016, 6 (2), 1-23.
4. Van Le, Q.; Jang, H. W.; Kim, S. Y., Recent Advances toward High-Efficiency Halide Perovskite Light-Emitting Diodes: Review and Perspective. *Small Methods* 2018, 2 (10), 1700419.
5. Stylianakis, M. M.; Maksudov, T.; Panagiotopoulos, A.; Kakavelakis, G.; Petridis, K., Inorganic and Hybrid Perovskite Based Laser Devices: A Review. *Materials* 2019, 12 (6), 859.
6. Wei, H.; Fang, Y.; Mulligan, P.; Chuirazzi, W.; Fang, H.-H.; Wang, C.; Ecker, B. R.; Gao, Y.; Loi, M. A.; Cao, L., et al., Sensitive X-Ray Detectors made of Methylammonium Lead Tribromide Perovskite Single Crystals. *Nat. Photonics*. 2016, 10 (5), 333-339.
7. National Renewable Energy Laboratory (NREL) Best Research- Cell Efficiencies Chart. <https://www.nrel.gov/pv/cell-efficiency.html> (accessed 2020-08).
8. Stranks, S. D.; Eperon, G. E.; Grancini, G.; Menelaou, C.; Alcocer, M. J. P.; Leijtens, T.; Herz, L. M.; Petrozza, A.; Snaith, H. J., Electron-Hole Diffusion Lengths

- Exceeding 1 Micrometer in an Organometal Trihalide Perovskite Absorber. *Science* 2013, 342 (6156), 341.
9. Brenner, T. M.; Egger, D. A.; Kronik, L.; Hodes, G.; Cahen, D., Hybrid Organic—Inorganic Perovskites: Low-Cost Semiconductors with Intriguing Charge-Transport Properties. *Nat. Rev. Mater.* 2016, 1 (1), 15007.
 10. Jena, A. K.; Kulkarni, A.; Miyasaka, T., Halide Perovskite Photovoltaics: Background, Status, and Future Prospects. *Chem. Rev.* 2019, 119 (5), 3036-3103.
 11. Konstantakou, M.; Stergiopoulos, T., A Critical Review on Tin Halide Perovskite Solar Cells. *J. Mater. Chem. A* 2017, 5 (23), 11518-11549.
 12. Yang, X.; Wang, W.; Ran, R.; Zhou, W.; Shao, Z., Recent Advances in Cs₂AgBiBr₆-Based Halide Double Perovskites as Lead-Free and Inorganic Light Absorbers for Perovskite Solar Cells. *Energy Fuels* 2020.
 13. Uddin, A.; Upama, M. B.; Yi, H.; Duan, L., Encapsulation of Organic and Perovskite Solar Cells: A Review. *Coatings* 2019, 9 (2), 65.
 14. Yan, J.; Qiu, W.; Wu, G.; Heremans, P.; Chen, H., Recent Progress in 2D/Quasi-2D Layered Metal Halide Perovskites for Solar Cells. *J. Mater. Chem. A* 2018, 6 (24), 11063-11077.
 15. Goldschmidt, V. M., Die Gesetze der Krystallochemie. *Naturwissenschaften* 1926, 14 (21), 477-485.
 16. Yi, Z.; Ladi, N. H.; Shai, X.; Li, H.; Shen, Y.; Wang, M., Will Organic–Inorganic Hybrid Halide Lead Perovskites be Eliminated from Optoelectronic Applications? *Nanoscale Adv.* 2019, 1 (4), 1276-1289.
 17. Stoumpos, C. C.; Malliakas, C. D.; Kanatzidis, M. G., Semiconducting Tin and Lead Iodide Perovskites with Organic Cations: Phase Transitions, High Mobilities, and Near-Infrared Photoluminescent Properties. *Inorg. Chem.* 2013, 52 (15), 9019-9038.
 18. Gélvez-Rueda, M. C.; Cao, D. H.; Patwardhan, S.; Renaud, N.; Stoumpos, C. C.; Schatz, G. C.; Hupp, J. T.; Farha, O. K.; Savenije, T. J.; Kanatzidis, M. G., et al., Effect of Cation Rotation on Charge Dynamics in Hybrid Lead Halide Perovskites. *J. Phys. Chem. C* 2016, 120 (30), 16577-16585.
 19. Mitzi, D. B., Synthesis, Crystal Structure, and Optical and Thermal Properties of (C₄H₉NH₃)₂MI₄ (M = Ge, Sn, Pb). *Chem. Mater.* 1996, 8 (3), 791-800.
 20. Stoumpos, C. C.; Cao, D. H.; Clark, D. J.; Young, J.; Rondinelli, J. M.; Jang, J. I.; Hupp, J. T.; Kanatzidis, M. G., Ruddlesden–Popper Hybrid Lead Iodide Perovskite 2D Homologous Semiconductors. *Chem. Mater.* 2016, 28 (8), 2852-2867.
 21. Billing, D. G.; Lemmerer, A., Synthesis, Characterization and Phase Transitions in the Inorganic–Organic Layered Perovskite-Type Hybrids [(C_nH_{2n+1}NH₃)₂PbI₄], n = 4, 5 and 6. *Acta Crystallogr. B* 2007, 63 (Pt 5), 735-47.
 22. Koh, T. M.; Shanmugam, V.; Guo, X.; Lim, S. S.; Filonik, O.; Herzig, E. M.; Müller-Buschbaum, P.; Swamy, V.; Chien, S. T.; Mhaisalkar, S. G., et al., Enhancing Moisture Tolerance in Efficient Hybrid 3D/2D Perovskite Photovoltaics. *J. Mater. Chem. A* 2018, 6 (5), 2122-2128.
 23. Lemmerer, A.; Billing, D. G., Synthesis, Characterization and Phase Transitions of the Inorganic–Organic Layered Perovskite-Type Hybrids [(C_nH_{2n+1}NH₃)₂PbI₄], n = 7, 8, 9 and 10. *Dalton Trans.* 2012, 41 (4), 1146-57.
 24. Gao, Y.; Shi, E.; Deng, S.; Shiring, S. B.; Snaider, J. M.; Liang, C.; Yuan, B.; Song,

- R.; Janke, S. M.; Liebman-Peláez, A., et al., Molecular Engineering of Organic-Inorganic Hybrid Perovskites Quantum Wells. *Nat. Chem.* 2019, 11 (12), 1151-1157.
25. Passarelli, J. V.; Fairfield, D. J.; Sather, N. A.; Hendricks, M. P.; Sai, H.; Stern, C. L.; Stupp, S. I., Enhanced Out-of-Plane Conductivity and Photovoltaic Performance in $n = 1$ Layered Perovskites through Organic Cation Design. *J. Am. Chem. Soc.* 2018, 140 (23), 7313-7323.
 26. Maheshwari, S.; Savenije, T. J.; Renaud, N.; Grozema, F. C., Computational Design of Two-Dimensional Perovskites with Functional Organic Cations. *J. Phys. Chem. C* 2018, 122 (30), 17118-17122.
 27. Gélvez-Rueda, M. C.; Fridriksson, M. B.; Dubey, R. K.; Jager, W. F.; van der Stam, W.; Grozema, F. C., Overcoming the Exciton Binding Energy in Two-Dimensional Perovskite Nanoplatelets by Attachment of Conjugated Organic Chromophores. *Nat. Commun.* 2020, 11 (1), 1901.
 28. Lanty, G.; Jemli, K.; Wei, Y.; Leymarie, J.; Even, J.; Lauret, J.-S.; Deleporte, E., Room-Temperature Optical Tunability and Inhomogeneous Broadening in 2D-Layered Organic-Inorganic Perovskite Pseudobinary Alloys. *J. Phys. Chem. Lett.* 2014, 5 (22), 3958-3963.
 29. Mitzi, D.; Wang, S.; Feild, C.; Chess, C.; Guloy, A., Conducting Layered Organic-Inorganic Halides Containing $\langle 110 \rangle$ -Oriented Perovskite Sheets. *Science* 1995, 267 (5203), 1473-1476.
 30. Smith, I. C.; Hoke, E. T.; Solis-Ibarra, D.; McGehee, M. D.; Karunadasa, H. I., A Layered Hybrid Perovskite Solar-Cell Absorber with Enhanced Moisture Stability. *Angew. Chem. Int. Ed.* 2014, 53 (42), 11232-5.
 31. Cao, D. H.; Stoumpos, C. C.; Farha, O. K.; Hupp, J. T.; Kanatzidis, M. G., 2D Homologous Perovskites as Light-Absorbing Materials for Solar Cell Applications. *J. Am. Chem. Soc.* 2015, 137 (24), 7843-50.
 32. Wu, X.; Trinh, M. T.; Niesner, D.; Zhu, H.; Norman, Z.; Owen, J. S.; Yaffe, O.; Kudisch, B. J.; Zhu, X. Y., Trap States in Lead Iodide Perovskites. *J. Am. Chem. Soc.* 2015, 137 (5), 2089-2096.
 33. Wu, X.; Trinh, M. T.; Zhu, X. Y., Excitonic Many-Body Interactions in Two-Dimensional Lead Iodide Perovskite Quantum Wells. *J. Phys. Chem. C* 2015, 119 (26), 14714-14721.
 34. Tanaka, K.; Kondo, T., Bandgap and Exciton Binding Energies in Lead-Iodide-Based Natural Quantum-Well Crystals. *Sci. Technol. Adv. Mater.* 2003, 4 (6), 599-604.
 35. Tsai, H.; Nie, W.; Blancon, J. C.; Stoumpos, C. C.; Asadpour, R.; Harutyunyan, B.; Neukirch, A. J.; Verduzco, R.; Crochet, J. J.; Tretiak, S., et al., High-Efficiency Two-Dimensional Ruddlesden-Popper Perovskite Solar Cells. *Nature* 2016, 536 (7616), 312-6.
 36. Yuan, M.; Quan, L. N.; Comin, R.; Walters, G.; Sabatini, R.; Voznyy, O.; Hoogland, S.; Zhao, Y.; Beauregard, E. M.; Kanjanaboos, P., et al., Perovskite Energy Funnels for Efficient Light-Emitting Diodes. *Nat. Nanotechnol.* 2016, 11 (10), 872-877.
 37. Gharibzadeh, S.; Abdollahi Nejang, B.; Jakoby, M.; Abzieher, T.; Hauschild, D.; Moghadamzadeh, S.; Schwenzer, J. A.; Brenner, P.; Schmager, R.; Haghighirad, A. A., et al., Record Open-Circuit Voltage Wide-Bandgap Perovskite Solar Cells

- Utilizing 2D/3D Perovskite Heterostructure. *Adv. Energy Mater.* 2019, 9 (21), 1803699.
38. Hutter, E. M.; Gélvez-Rueda, M. C.; Osherov, A.; Bulović, V.; Grozema, F. C.; Stranks, S. D.; Savenije, T. J., Direct-Indirect Character of the Bandgap in Methylammonium Lead Iodide Perovskite. *Nat. Mater.* 2017, 16 (1), 115-120.
 39. Brivio, F.; Butler, K. T.; Walsh, A.; van Schilfgaarde, M., Relativistic Quasiparticle Self-Consistent Electronic Structure of Hybrid Halide Perovskite Photovoltaic Absorbers. *Phys. Rev. B* 2014, 89 (15), 155204.
 40. Buin, A.; Comin, R.; Xu, J.; Ip, A. H.; Sargent, E. H., Halide-Dependent Electronic Structure of Organolead Perovskite Materials. *Chem. Mater.* 2015, 27 (12), 4405-4412.
 41. Noh, J. H.; Im, S. H.; Heo, J. H.; Mandal, T. N.; Seok, S. I., Chemical Management for Colorful, Efficient, and Stable Inorganic-Organic Hybrid Nanostructured Solar Cells. *Nano Lett.* 2013, 13 (4), 1764-1769.
 42. Kulkarni, S. A.; Baikie, T.; Boix, P. P.; Yantara, N.; Mathews, N.; Mhaisalkar, S., Band-Gap Tuning of Lead Halide Perovskites Using a Sequential Deposition Process. *J. Mater. Chem. A* 2014, 2 (24), 9221-9225.
 43. Tanaka, K.; Takahashi, T.; Kondo, T.; Umebayashi, T.; Asai, K.; Ema, K., Image Charge Effect on Two-Dimensional Excitons in an Inorganic-Organic Quantum-Well Crystal. *Phys. Rev. B* 2005, 71 (4), 045312.
 44. Ishihara, T.; Takahashi, J.; Goto, T., Exciton State in Two-Dimensional Perovskite Semiconductor (C₁₀H₂₁NH₃)₂PbI₄. *Solid State Commun.* 1989, 69 (9), 933-936.
 45. Ishihara, T., Optical Properties of PbI-Based Perovskite Structures. *J. Lumin.* 1994, 60, 269-274.
 46. Muljarov, E. A.; Tikhodeev, S. G.; Gippius, N. A.; Ishihara, T., Excitons in Self-Organized Semiconductor/Insulator Superlattices: PbI-Based Perovskite Compounds. *Phys. Rev. B* 1995, 51 (20), 14370-14378.
 47. Yaffe, O.; Chernikov, A.; Norman, Z. M.; Zhong, Y.; Velauthapillai, A.; van der Zande, A.; Owen, J. S.; Heinz, T. F., Excitons in Ultrathin Organic-Inorganic Perovskite Crystals. *Phys. Rev. B* 2015, 92 (4), 045414.
 48. Ishihara, T.; Takahashi, J.; Goto, T., Optical Properties due to Electronic Transitions in Two-Dimensional Semiconductors (C_nH_{2n+1}NH₃)₂PbI₄. *Phys. Rev. B* 1990, 42 (17), 11099.
 49. Hattori, T.; Taira, T.; Era, M.; Tsutsui, T.; Saito, S., Highly Efficient Electroluminescence from a Heterostructure Device Combined with Emissive Layered-Perovskite and an Electron-Transporting Organic Compound. *Chem. Phys. Lett.* 1996, 254 (1-2), 103-108.
 50. Gebauer, T.; Schmid, G., Inorganic-organic Hybrid Structured LED's. *Z. Anorg. Allg. Chem.* 1999, 625 (7), 1124-1128.
 51. Kondo, T.; Iwamoto, S.; Hayase, S.; Tanaka, K.; Ishi, J.; Mizuno, M.; Ema, K.; Ito, R., Resonant Third-Order Optical Nonlinearity in the Layered Perovskite-Type Material (C₆H₁₃NH₃)₂PbI₄. *Solid State Commun.* 1998, 105 (8), 503-506.
 52. Fujita, T.; Sato, Y.; Kuitani, T.; Ishihara, T., Tunable Polariton Absorption of Distributed Feedback Microcavities at Room Temperature. *Phys. Rev. B* 1998, 57 (19), 12428-12434.

53. Yablonskii, Alexander L.; Muljarov, Egor A.; Gippius, Nikolai A.; Tikhodeev, Sergei G.; Fujita, T.; Ishihara, T., Polariton Effect in Distributed Feedback Microcavities. *J. Phys. Soc. Jpn.* 2001, 70 (4), 1137-1144.
54. Brehier, A.; Parashkov, R.; Lauret, J.-S.; Deleporte, E., Strong Exciton-Photon Coupling in a Microcavity Containing Layered Perovskite Semiconductors. *Appl. Phys. Lett.* 2006, 89 (17), 171110.
55. Wenus, J.; Parashkov, R.; Ceccarelli, S.; Brehier, A.; Lauret, J. S.; Skolnick, M. S.; Deleporte, E.; Lidzey, D. G., Hybrid Organic-Inorganic Exciton-Polaritons in a Strongly Coupled Microcavity. *Phys. Rev. B* 2006, 74 (23), 235212.
56. Lanty, G.; Lauret, J.-S.; Deleporte, E.; Bouchoule, S.; Lafosse, X., UV Polaritonic Emission from a Perovskite-Based Microcavity. *Appl. Phys. Lett.* 2008, 93 (8), 081101.
57. Chondroudis, K.; Mitzi, D. B., Electroluminescence from an Organic-Inorganic Perovskite Incorporating a Quaterthiophene Dye within Lead Halide Perovskite Layers. *Chem. Mater.* 1999, 11 (11), 3028-3030.
58. Gauthron, K.; Lauret, J. S.; Doyennette, L.; Lanty, G.; Al Choueiry, A.; Zhang, S. J.; Brehier, A.; Largeau, L.; Mauguin, O.; Bloch, J., et al., Optical Spectroscopy of Two-Dimensional Layered (C₆H₅C₂H₄-NH₃)₂-PbI₄ Perovskite. *Opt. Express* 2010, 18 (6), 5912-5919.
59. Dou, L.; Wong, A. B.; Yu, Y.; Lai, M.; Kornienko, N.; Eaton, S. W.; Fu, A.; Bischak, C. G.; Ma, J.; Ding, T., et al., Atomically Thin Two-Dimensional Organic-Inorganic Hybrid Perovskites. *Science* 2015, 349 (6255), 1518-21.
60. Zhang, S.; Yi, C.; Wang, N.; Sun, Y.; Zou, W.; Wei, Y.; Cao, Y.; Miao, Y.; Li, R.; Yin, Y., et al., Efficient Red Perovskite Light-Emitting Diodes Based on Solution-Processed Multiple Quantum Wells. *Adv. Mater.* 2017, 29 (22), 1606600.
61. Hong, X.; Ishihara, T.; Nurmikko, A. V., Dielectric Confinement Effect on Excitons in PbI₄-Based Layered Semiconductors. *Phys. Rev. B* 1992, 45 (12), 6961-6964.
62. Gélvez-Rueda, M. C.; Hutter, E. M.; Cao, D. H.; Renaud, N.; Stoumpos, C. C.; Hupp, J. T.; Savenije, T. J.; Kanatzidis, M. G.; Grozema, F. C., Interconversion between Free Charges and Bound Excitons in 2D Hybrid Lead Halide Perovskites. *J. Phys. Chem. C* 2017, 121 (47), 26566-26574.
63. Gélvez-Rueda, M. C.; Ahlawat, P.; Merten, L.; Jahanbakhshi, F.; Mladenović, M.; Hinderhofer, A.; Dar, M. I.; Li, Y.; Dučinskas, A.; Carlsen, B., et al., Formamidinium-Based Dion-Jacobson Layered Hybrid Perovskites: Structural Complexity and Optoelectronic Properties. *Adv. Funct. Mater.* 2020, 2003428.
64. Mao, L.; Stoumpos, C. C.; Kanatzidis, M. G., Two-Dimensional Hybrid Halide Perovskites: Principles and Promises. *J. Am. Chem. Soc.* 2019, 141 (3), 1171-1190.
65. Baranowski, M.; Zelewski, S. J.; Kepenekian, M.; Traoré, B.; Urban, J. M.; Surrante, A.; Galkowski, K.; Maude, D. K.; Kuc, A.; Booker, E. P., et al., Phase-Transition-Induced Carrier Mass Enhancement in 2D Ruddlesden-Popper Perovskites. *ACS Energy Lett.* 2019, 4 (10), 2386-2392.
66. Seitz, M.; Magdaleno, A. J.; Alcazar-Cano, N.; Melendez, M.; Lubbers, T. J.; Walraven, S. W.; Pakdel, S.; Prada, E.; Delgado-Buscalioni, R.; Prins, F., Exciton Diffusion in Two-Dimensional Metal-Halide Perovskites. *Nat. Commun.* 2020, 11 (1), 2035.
67. Long, G.; Jiang, C.; Sabatini, R.; Yang, Z.; Wei, M.; Quan, L. N.; Liang, Q.; Rasmita,

- A.; Askerka, M.; Walters, G., et al., Spin Control in Reduced-Dimensional Chiral Perovskites. *Nat. Photonics*. 2018, 12 (9), 528-533.
68. Lu, H.; Wang, J.; Xiao, C.; Pan, X.; Chen, X.; Brunecky, R.; Berry, J. J.; Zhu, K.; Beard, M. C.; Vardeny, Z. V., Spin-Dependent Charge Transport Through 2D Chiral Hybrid Lead-Iodide Perovskites. *Sci. Adv.* 2019, 5 (12), eaay0571.
 69. Ahmad, S.; Fu, P.; Yu, S.; Yang, Q.; Liu, X.; Wang, X.; Wang, X.; Guo, X.; Li, C., Dion-Jacobson Phase 2D Layered Perovskites for Solar Cells with Ultrahigh Stability. *Joule* 2019, 3 (3), 794-806.
 70. Mitzi, D. B.; Dimitrakopoulos, C. D.; Kosbar, L. L., Structurally Tailored Organic–Inorganic Perovskites: Optical Properties and Solution-Processed Channel Materials for Thin-Film Transistors. *Chem. Mater.* 2001, 13 (10), 3728-3740.
 71. Deng, M.; Wu, G.; Cheng, S.-Y.; Wang, M.; Borghs, G.; Chen, H.-Z., Photoconducting hybrid perovskite containing carbazole moiety as the organic layer: Fabrication and characterization. *Materials Science and Engineering: B* 2008, 147 (1), 90-94.
 72. Mitzi, D. B., Organic–Inorganic Perovskites Containing Trivalent Metal Halide Layers: The Templating Influence of the Organic Cation Layer. *Inorg. Chem.* 2000, 39 (26), 6107-6113.
 73. Mitzi, D. B.; Chondroudis, K.; Kagan, C. R., Design, Structure, and Optical Properties of Organic–Inorganic Perovskites Containing an Oligothiophene Chromophore. *Inorg. Chem.* 1999, 38 (26), 6246-6256.
 74. Jana, M. K.; Janke, S. M.; Dirkes, D. J.; Dovletgeldi, S.; Liu, C.; Qin, X.; Gundogdu, K.; You, W.; Blum, V.; Mitzi, D. B., Direct-Bandgap 2D Silver–Bismuth Iodide Double Perovskite: The Structure-Directing Influence of an Oligothiophene Spacer Cation. *J. Am. Chem. Soc.* 2019, 141 (19), 7955-7964.
 75. Deng, S.; Snider, J. M.; Gao, Y.; Shi, E.; Jin, L.; Schaller, R. D.; Dou, L.; Huang, L., Long-Lived Charge Separation in Two-Dimensional Ligand-Perovskite Heterostructures. *J. Chem. Phys.* 2020, 152 (4), 044711.
 76. Li, Q.; Lian, T., Ultrafast Charge Separation in Two-Dimensional CsPbBr₃ Perovskite Nanoplatelets. *J. Phys. Chem. Lett.* 2019, 10 (3), 566-573.
 77. Gélvez-Rueda, M. C.; Van Gompel, W. T. M.; Herckens, R.; Lutsen, L.; Vanderzande, D.; Grozema, F. C., Inducing Charge Separation in Solid-State Two-Dimensional Hybrid Perovskites through the Incorporation of Organic Charge-Transfer Complexes. *J. Phys. Chem. Lett.* 2020, 11 (3), 824-830.
 78. Weidman, M. C.; Goodman, A. J.; Tisdale, W. A., Colloidal Halide Perovskite Nanoplatelets: An Exciting New Class of Semiconductor Nanomaterials. *Chem. Mater.* 2017, 29 (12), 5019-5030.

2



The Relation Between Rotational Dynamics of the Organic Cation and Phase Transitions in Hybrid Halide Perovskites

The rotational dynamics of organic cations in hybrid halide perovskites are intricately linked to the phase transitions that are known to occur in these materials, however, the exact relation is not clear. In this chapter we have performed detailed model studies on methylammonium lead iodide and formamidinium lead iodide to unravel the relation between rotational dynamics and phase behavior. We show that the occurrence of the phase transitions is due to a subtle interplay between dipole-dipole interactions between the organic cations, specific (hydrogen bonding) interactions between the organic cation and the lead-iodide lattice, and deformation of the lead-iodide lattice in reaction to the reduced rotational motion of the organic cations. This combination of factors results in phase transitions at specific temperatures, leading to the formation of large organized domains of dipoles. The latter can have significant effects on the electronic structure of these materials.

This chapter is based on: Maheshwari, S.^{||}; Fridriksson, M. B.^{||}; Seal, S.; Meyer, J.; Grozema, F. C., J. Phys. Chem. C 2019, 123 (23), 14652-14661

^{||} These authors contributed equally to this work

2.1 Introduction

Hybrid halide perovskites are currently among the most studied emerging solar cell materials, with reported device efficiencies well over 20% approximately ten years after the first demonstration of a halide perovskite-based cell.¹⁻³ Hybrid halide perovskites consist of a general ABX_3 structure where B is a doubly charged metal ion such as lead or tin and X is a halide anion. A is a singly charged cation that, in the case of hybrid perovskites, is an organic ammonium compound such as methylammonium (MA) or formamidinium (FA). The metal and the halide ions together form an inorganic octahedral lattice with cages that are filled by the organic cations. The most common organic cation, methylammonium, has an asymmetric charge distribution resulting in a net dipole moment. At room temperature, the dipolar MA cation can rotate almost freely inside the metal-halide lattice. This leads to a high dielectric screening compared to halide perovskites with non-dipolar cations such as Cs^+ .⁴ It has also been proposed that the dipolar nature of MA plays an important role in the opto-electronic properties of hybrid halide perovskites, for instance through the formation of ferro-electric domains that promote formation of free charges on photo excitation or through polaronic effects that enhance the charge carrier lifetime.⁵⁻⁶ The rotational freedom of MA has been found to be highly dependent on temperature and specific phase transitions are known to occur. For instance, methylammonium lead iodide (MAPbI) has a cubic structure at temperatures above 330 K, in which the MA can rotate freely. Between 170 K and 330 K a tetragonal phase is formed, in which the rotational motion is somewhat restricted. At temperatures below 170 K an orthorhombic phase is present where the rotational motion is fully absent.⁷ In previous experimental work it has been shown that the rotational freedom of the organic cation has a direct effect on the mobility and recombination kinetics of charges in MAPbI.⁸ Therefore, the rotational dynamics of organic cations in hybrid perovskites has received considerable attention, both experimentally and theoretically.⁹⁻¹² However, the relation to the phase behavior, and its effect on the opto-electronic properties of hybrid halide perovskites is not fully understood.

Most of the previous work has focused on the rotation of the MA ion in MAPbI as this is the most investigated of the hybrid perovskites in solar cells. Experimentally this includes solid-state NMR measurements,⁹ single crystal x-ray measurements,¹³ Raman spectroscopy¹³ and quasielastic neutron scattering.¹⁰ Theoretically, Monte Carlo simulations have been performed,^{5, 14} as well as density functional theory studies¹⁵⁻¹⁶ and both ab initio molecular dynamics¹⁷⁻¹⁹ and model potential molecular dynamics.^{12, 20-21} Most of these studies agree that at high temperatures the MA ion rotates freely without forming any ferroelectric or anti-ferroelectric domains, while below a certain phase transition temperature an orthorhombic phase is formed where the dipole rotation is frozen. The cause and effect relationship between the dipole dynamics and the phase transition is not fully understood. While most argue that the transfer to orthorhombic phase is the source of the restricted motion of the MA ions, some have suggested that the deformation of the lead iodide cage is caused by formation of ordered domains of dipoles at low temperatures.¹⁵

For formamidinium lead halide perovskites (FAPbI) there is a lot less information. The FA cation is larger than MA, which may restrict its rotational motion by steric interactions.

It also has an almost negligible dipole moment and it contains two nitrogen positions including hydrogens that can form hydrogen bonds with the lead iodide cage. FAPbI exhibits a high temperature cubic perovskite structure²² and a low temperature structure with octahedral tilting.²³ Carignano et al. have performed ab initio molecular dynamics simulations on FAPbI and reported that at high temperatures there are preferential alignments of the FA ion due to hydrogen bonds with the cage.²⁴ They also concluded that FA rotates preferentially around the N-N axis, which has later been supported by other studies.²³⁻²⁴ Weber et al. reported that FA shows a certain ordering at low temperature where they align perpendicular with respect to their nearest neighbor due to the angle tilt of the cage.²⁵

The time scale of the reorientation of the organic cation has been studied both theoretically and experimentally for both MAPbI and FAPbI with varying conclusions.²⁶ Experimentally, methods such as neutron scattering experiments, two-dimension infrared spectroscopy and solid state NMR have been employed, giving timescales of reorientation for MA ranging from 1.7 ps to 108 ps at room temperature^{5, 9, 11, 23, 26-29} and 2.8 ps to 8.7 ps for FA at same conditions.^{23, 26, 29-30} A few papers have studied both MAPbI and FAPbI and therefore given a direct comparison of the timescales. Fabini et al. found timescales of similar magnitude for MA and FA, 7 ps and 8 ps respectively.²³ Kubicki et al. on the other hand found FA to reorient much faster than MA, 8.7 ps and 108 ps respectively.²⁹ Theoretically molecular dynamics simulations have also been performed to investigate the motion of the organic cation, either by ab initio dynamics or using classical force fields. From such simulations a reorientation time of approximately 7 ps has been obtained for MA at room temperature^{17, 19, 21} and values of 4.3 ps²⁴ and 8.8 ps²⁵ for FA at same conditions.

In this chapter we have studied the relation between the reorientation dynamics of MA and FA in MAPbI and FAPbI and their phase transition behavior. Apart from just performing full molecular dynamics simulations, we have also performed a series of model calculations to clarify the role of specific interactions in the system. These model calculations include on-lattice Metropolis Monte Carlo simulations to study domain formation in a system with only dipole-dipole interactions and molecular dynamics simulations with a frozen cage. Together, these calculations give a new picture of the origin of the structural phase transitions in hybrid perovskites, which shows that they are caused by an interplay between dipole-dipole interactions, specific (hydrogen bonding) interactions between the organic cation and the inorganic cage and deformation of the metal halide cage.

2.2 Methods

2.2.1 Molecular dynamics

The molecular dynamics (MD) simulations were performed on a super cell of $10 \times 10 \times 10$ unit cells with periodic boundary conditions for MAPbI and FAPbI. The system size was chosen to access better statistics and independence of motion of dipoles in different parts of the system. Initial configuration was selected as cubic both for MAPbI and FAPbI with lattice constant of 6.21 Å for MAPbI and 6.36 Å for FAPbI as observed experimentally at higher temperatures for both of these materials.^{5, 22} The force field for the interatomic potentials was adopted from the work of Mattoni et. al.¹² The interactions in the force field are defined in form of three components i) inorganic-inorganic(U_{ii}), ii) inorganic-

organic(U_{io}) and iii) organic-organic(U_{oo}) interactions. The U_{ii} and U_{io} are non-bonded interactions which are defined in terms of Buckingham and Lennard-Jones parameters that take into account electrostatic and Van der Waals interactions respectively. U_{oo} interactions are defined as bonded interactions with parameters for bond stretching, angle bending and dihedral rotations for the organic cations. These parameters were obtained from the CHARMM force field using the Swiss-Param tool.³¹⁻³⁴ MD simulations were performed using the LAMMPS molecular dynamics simulation package.³⁵ The equations of motion were evaluated using time step of 1 fs and a cutoff of 17 Å for Lennard-Jones interactions and 18 Å for the Coulombic interactions. Simulations were performed in a sequence of three steps in which first step was annealing of system with an initial configuration of ordered orientations of MA/FA molecules. The annealing was performed from a higher temperature to the temperature required for the system over 3 nanoseconds. The second step was the equilibration of the system at the required temperature until the energy of system comes to an equilibrium. The third step was the production run from which a trajectory file covering 100 ps was obtained. The rotational dynamics of the organic cations in MAPbI and FAPbI were analyzed by examining the rotational autocorrelation function (ACF) as defined in Equation 2.1 in terms of the unit dipole vectors \hat{n} of the MA and FA cations. For MA this vector coincides with the C-N axis, while for FA it is along the C-H bond. The N_{ion} represent the number of MA or FA ions respectively in the system and the N_{t_0} is the number of initial time (t_0) considered in the calculation.

$$A(t) = \langle \hat{n}(t) \cdot \hat{n}(0) \rangle = \frac{1}{N_{ion}} \sum_i \frac{1}{N_{t_0}} \sum_{t_1=t+t_0} \hat{n}_i(t_1) \cdot \hat{n}_i(t_0) \quad 2.1$$

The ACF gives a measure of how fast the orientations of the organic cations change with time. By definition the starting value of the ACF is one and decays to zero on average once the direction of the dipole has become completely random.

2.2.2 Monte Carlo

The Metropolis Monte Carlo (MC) simulations were performed on a system consisting of $20 \times 20 \times 20$ dipoles on a fixed grid with periodic boundary conditions. A cubic structure is assumed for all temperatures with a lattice constant of 6.29 Å. The only energy considered in the simulation is the (electrostatic) dipole-dipole interaction given by Equation 2.2. In this equation, p_i and p_j are the dipole moment vectors for both dipoles considered, r is the distance between the dipoles and \hat{n} is a unitary directional vector between the two dipoles. Permittivity of vacuum is assumed, ignoring any dielectric screening. This will lead to some overestimation of dipole-dipole interaction compared to physical systems. Only interactions between dipoles that are within three lattice distances of one another are considered. This is a reasonable assumption since the interaction energy is inversely proportional to the third power of the distance. The simulations were performed for both MA and FA dipoles at temperatures ranging from 100 K to 350 K with a 10 K interval.

$$E_{dd} = \frac{1}{4\pi\epsilon_0} \left(\frac{p_i \cdot p_j}{r^3} - \frac{3(\hat{n} \cdot p_i)(\hat{n} \cdot p_j)}{r^3} \right) \quad 2.2$$

2.2.3 Domain detection

The domain detection aims to quantify how ordered or disordered the organic cations are at various temperatures in the MC and MD simulations based on dipole-dipole interaction. It does so by ordering all the dipoles in a simulation snapshot on a fixed grid and choosing a random dipole in the system. This dipole is the first dipole in the first domain. Next we evaluate which, if any of the six closest neighbors of the dipole belong in the same domain. This is done by comparing the orientations of those dipoles with the orientations that would minimize the dipole-dipole interaction energy between each of them and our first dipole. If their orientation is close enough to this minimum energy alignment they are added to the domain. The domain is then allowed to grow by evaluating the neighbors of the dipoles that were added to the domain. When all appropriate dipoles have been added to the domain the process is repeated considering all the dipoles in the system that have not been assigned to a domain. Finally, when all the dipoles have been assigned to a domain the average domain size is calculated. A large average domain size will then represent a more ordered system than a small one.

2.3 Results and discussion

Molecular dynamics and Monte Carlo simulations were performed both for MAPbI and FAPbI and we have subdivided the discussion in two parts. First we discuss the dipole dynamics and phase transitions in MAPbI, after which we turn to FAPbI. The results in both materials are compared and some general conclusions are presented after these sections.

2.3.1 Methyammonium lead iodide (MAPbI)

From the molecular dynamics simulation of MAPbI, a trajectory of 100 ps is obtained after equilibration of the system. The ACF over these 100 ps, averaged over the 1000 MA dipoles in the system is shown in Figure 2.1a for temperatures between 100 K and 350 K. The ACF plots show the randomization of the direction of the dipole moments with time. At lower temperatures (100-250 K) the ACF plots show a different trend than those at higher temperature. After an initial rapid decay, an almost constant value is obtained, indicating that no full randomization of the dipole direction occurs on the timescale of the simulations. The rapid initial decay corresponds to a wobbling-like motion where the dipolar molecule can move around in a cone but does not have enough rotational freedom for complete reorientation. The more pronounced initial decay at 150 K and 200 K, as compared to that at 100 K indicates that the cone in which movement takes place widens with temperature. In order to quantify the timescale of dipole relaxation times, the ACF curves were fitted with a bi-exponential function given in Equation 2.3. A_1 and A_2 are the amplitudes of the two decay components characterized by the decay times τ_1 and τ_2 . The two time constants can relate to different processes, e.g. the in-place wobbling motion and the full reorientation mentioned in the introduction. The parameters from fitting Equation 2.3 are summarized in Table 2.1.

$$y = A_1 \cdot e^{-t/\tau_1} + A_2 \cdot e^{-t/\tau_2} \quad 2.3$$

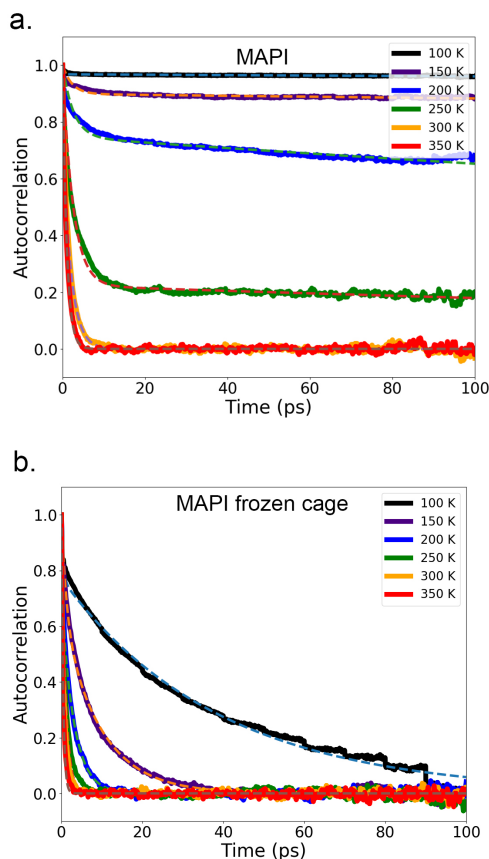


Figure 2.1 ACF for MAPbI. (a) ACF of the dipole direction averaged over 1000 dipoles for MA cations in a flexible lead iodide cage at temperatures ranging from 100 K to 350 K. (b) ACF of the dipole direction averaged over 1000 dipoles for MA cations in a frozen lead iodide cage at temperatures ranging from 100 K to 350 K.

At temperatures of 250 K and lower, two very distinct timescales are found from the bi-exponential fit, a fast one that is typically in the order of 2.5 ps, and a very slow one that exceeds the time scale of the simulations. The fast initial decay corresponds to the in-place wobbling of the MA dipole, while the long-time decay corresponds to the full reorientation. The long-time decay constant of 450 ps and longer for these temperature indicate that the dipole orientation is virtually fixed on the time scale considered. Above 250 K the ACF curves completely decay to zero within ≈ 5 ps. This indicates that at this temperature range, MA dipoles have full rotational freedom and behave almost liquid-like. At these temperatures the decay of the ACF can be described with a single exponential function with characteristic time constants of 0.5 - 2.0 ps. It is interesting to note, that at these temperatures, no distinction can be made between the wobbling motion and full reorientation. If the 300 K time constant is compared with previous experimental and theoretical work the full reorientation is slightly faster than in most cases but is still of

Table 2.1 ACF decay time constants for MA in picoseconds obtained after fitting the decay curves in Figure 2.1 using Equation 2.3. τ_1 corresponds to the faster decay time whereas τ_2 corresponds to the slower decay time constant.

T (K)	Flexible cage		Frozen cage	
	τ_1 (ps) (A1)	τ_2 (ps) (A1)	τ_1 (ps) (A1)	τ_2 (ps) (A1)
100	0.12 (0.03)	> 1000 (0.97)	0.42 (0.23)	38.75 (0.77)
150	2.26 (0.10)	> 1000 (0.90)	1.23 (0.35)	9.54 (0.65)
200	2.62 (0.25)	739.27 (0.75)	0.27 (0.30)	3.10 (0.70)
250	2.52 (0.78)	455.57 (0.22)	1.03 (1.00)	-
300	0.46 (0.25)	2.00 (0.75)	0.63 (1.00)	-
350	1.01 (1.00)	-	0.43 (1.00)	-

same order of magnitude.²⁶ These slight difference can be caused by shortcomings of the MD force field to describe the exact temperature behavior of the structure. The observed changes in rotational dynamics with temperature agree with experimentally observed phase dynamics and with earlier molecular dynamics simulation.^{9, 27, 36}

While the molecular dynamics simulations successfully describe the phase behavior in MAPbI₃, at least qualitatively, the details of the relation between the dynamics of the MA cations and the phase transition is not fully clear. We have identified three possible effects that can play a role in this. The first is the deformation of the Pb-I cages. The reduced rotation of MA at low temperatures can either be caused by the deformation of the cages, or the reduced dipole rotation causes the deformation itself. The second effect is the interaction between the different MA cations in the system, which can lead to ordered domains with restricted rotational dynamics at low temperature. Finally, the third effect is related to specific interactions between the MA cation and the Pb-I cage structure, for instance hydrogen bonds between the ammonium and iodide ions. In order to clarify the importance of these three effects, we have performed a series of model simulations that are outlined below.

2.3.1.1 Effect of cage deformation

In order to establish the importance of the deformation of the Pb-I framework on the rotational dynamics of the MA ions we have performed model calculations in which the positions of Pb and I are frozen in the initial cubic conformation. In this way we can obtain insight in the motion of the organic cations in presence of specific interactions with the Pb-I cage and interactions with different organic cations, but in absence of deformation of the cage. As evident from Figure 2.1b and Table 2.1, the ACF decreases faster than for a flexible cage. The decay time of the ACF decreases uniformly as the temperature is increased from 100 K to 350 K. No sudden change is observed in the rotation time at 200 K for the frozen cage. This shows that the rotational motion of the organic cation is highly influenced by deformation of the Pb-I framework, especially at low temperatures.

2.3.1.2 Effect of dipole-dipole interactions

The second specific interaction we look at is dipole-dipole interactions between the MA ions. To investigate to what extent these interactions affect the alignment of MA, we have performed MC simulations at various temperatures. In these simulations only

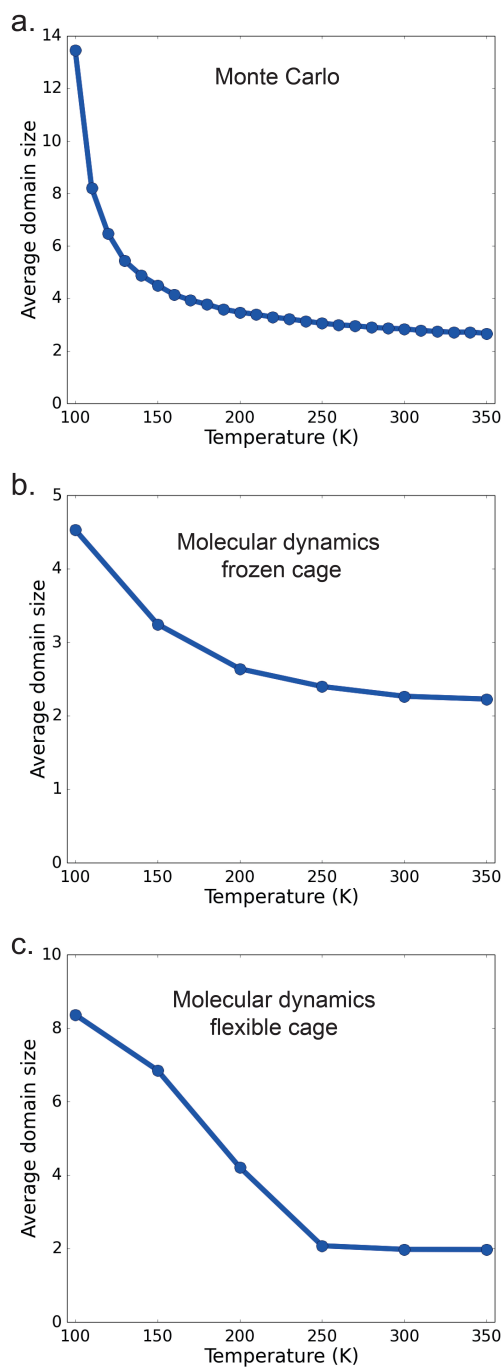


Figure 2.2 Average domain size vs temperature for methylammonium dipoles simulated with (a) Monte Carlo only considering dipole-dipole interaction, (b) molecular dynamics with frozen lead iodide cage, (c) molecular dynamics with flexible lead iodide cage

the dipole-dipole interaction energy is taken into account. Therefore, any formation of organized domains observed is solely due to these electrostatic interactions between MA ions, and not because of cage deformation or, for instance, hydrogen bonding with iodide. A convenient way to quantify the alignment of the MA dipolar ions with respect to each other is to look at snapshots of the simulations and divide all the ions into domains based on close range dipole-dipole interactions. A large domain then represents a certain long range ordering of dipoles. In Figure 2.2a the average domain size in the MC simulations is plotted versus the temperature. As these systems only depend on the dipole-dipole interaction energy, lowering the temperature, forces the dipoles to align more optimally with the other dipoles and especially their closest neighbors. This results in an exponential increase of average domain size as the temperature approaches 100 K, while at higher temperatures the systems is rather disordered as indicated by the smaller average domain size. This can be interpreted as a phase transition of sorts; at the temperature where $k_B T$ becomes comparable to the dipole-dipole interaction energy the ions align together due to their interactions with one another.

Figure 2.2b shows the same domain detection analysis on the MA ions in the MD simulations with a frozen cage. By comparing this to the simulations that only consider dipole-dipole interaction, we gain insight in the relative importance of the dipole-dipole interactions when specific interactions with the Pb-I cage are also taken into account. The frozen cage MD simulations show a similar trend in domain growth as the MC simulations. The increase in average domain size is however a lot smaller in this temperature range. This shows that with a surrounding cage, the MA ions are still affected by interaction with one another at low temperatures. However, the effect is less pronounced because specific interactions between the MA and the cage also play a role here.

To complete the comparison, we show the average size of domains of MA ions in the flexible cage MD simulations as a function of temperature in Figure 2.2c. These systems show a different behavior compared to the other two. First of all, the increase of the average domain size occurs at higher temperatures. Between 250 K and 200 K there is an abrupt increase in the average domain size whereas, for the other systems notable increase was not seen until at roughly 150 K. Furthermore, the nature of the increase is different compared to the MC system. In the case of the flexible MD simulations we do not observe a gradual exponential increase but instead an abrupt linear increase that seems to start saturating at the lowest simulated temperature. These differences are comparable to the difference we saw between the ACF plots for the flexible- and frozen-cage MD simulations. In the ACF decays, an abrupt step was seen between 200 K and 250 K for flexible Pb-I cages, resulting in less reorientation of the methylammonium ions at the lower temperature. This was not seen in the case of the frozen cage.

2.3.1.3 Effect of specific interactions between MA and cage

Having investigated the effect of cage movement and dipole-dipole interaction, the final step is to understand the role of specific interactions between the lead-iodide cage and MA ion. To achieve this we have analyzed the MD simulations above in more detail, paying specific attention to the directions of the MA ions in a single system with respect to the lead iodide cage. This is done by plotting scatter plots with all MA directions obtained from

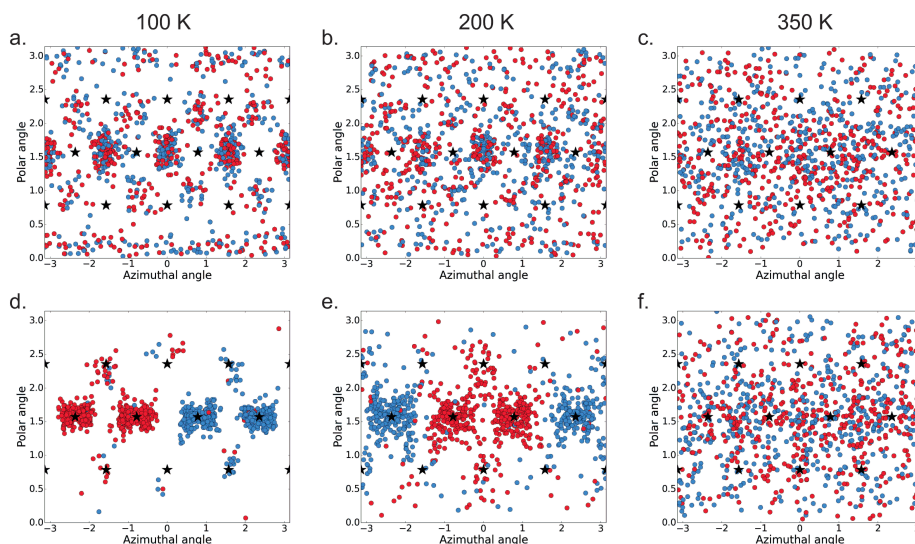


Figure 2.3 Orientations of all methylammonium dipoles in a single molecular dynamics system given in their polar and azimuthal angle. (a-c) frozen cage at 100 K, 200 K and 350 K and (d-f) flexible cage at 100 K, 200 K and 350 K. The stars in the figures represent the orientations where the dipole is oriented directly towards an iodide.

a single simulation snapshot. Each point is then the direction of a single ion represented in its azimuthal and polar angles. We do this to observe whether certain ion directions within the cage become more prominent than others as the temperature is changed. Two different colors are used for the points to evaluate whether there is a difference between the neighboring layers in the system. Odd number layers are portrayed by blue points and even number layers are indicated in red. In these figures, the stars represent the directions that correspond to an MA ion pointing directly towards an iodide atom in a cubic cage. These plots are shown in Figure 2.3 for both MD simulations with flexible and frozen cage at 100 K, 200 K and 350 K. Similar figures were made for the other simulated temperatures and for the dipole-dipole MC simulations, these figures can be found in the appendix. For the MC simulations there is no preferred MA orientation visible at any temperature. This is not surprising as there is no cage to affect the orientation of the MA ions. So even though the MA ions start to align favorably with one another at low temperatures and form domains, they do not necessarily align all in the same direction. Similar trend has been seen before in a two dimensional Monte Carlo study, where very low temperatures were needed to align all the MA ions in a certain way.¹⁴

Figures 2.3a-c show the directional ordering for the frozen-cage MD simulations at 100 K, 200 K and 350 K. At 350 K the alignment of the ions is random over the spherical surface; the reason for higher density at central polar angles is that this is a spherical surface projected on a rectangular graph. As the temperature is lowered to 200 K a structure emerges, with some orientations becoming more prominent than others. At 100 K this is even stronger. Surprisingly, the most common orientations are not directed towards iodides, as one would expect if the MA forms hydrogen bonds with the iodide.

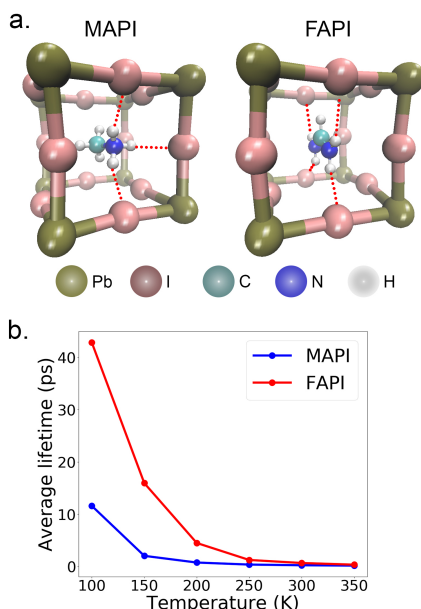


Figure 2.4 Hydrogen bonds. (a) The hydrogen bonds formed in MAPbI₃ and FAPbI₃ between the hydrogens of amine group and iodide atoms of the cage. (b) Hydrogen bond lifetime in picoseconds averaged for the hydrogen bonds formed for MAPbI₃ and FAPbI₃.

Furthermore, no difference is seen between different layers in these simulations.

Figures 2.3d-f represent the flexible cage MD simulations at 100 K, 200 K and 350 K. Again the alignment is random at 350 K and a more organized structure is formed when the temperature is lowered. In this case, however, the effect is much more pronounced with the ions aligning all in the same plane at the lowest temperature, and each adjacent layer aligning anti-parallel to its neighbor. Within each layer there are two main orientations, both where one would assume a hydrogen bond is formed. This is in agreement with previous *ab initio* and model potential molecular dynamics studies where same alignment was seen and attributed to the low temperature orthorhombic phase.^{12, 14}

In order to get some insight on the dynamics of the specific interaction we have analyzed the timescale on which the hydrogen bonds are broken. In this case we consider a hydrogen bond to occur when the distance between a hydrogen and an iodide is less than 3 Å. These hydrogen bond life times are shown in Figure 2.4b as a function of temperature. It is clear from this figure that the time that hydrogen bonds exist in MA is very short, except at 100 K where a lifetime over 10 ps is obtained. This is consistent with the large degree of rotational freedom discussed above, even if the general direction is frozen, the wobbling motion still allows a considerable freedom for the MA to move around.

2.3.2 Formamidinium lead iodide (FAPbI)

In a similar way as for MAPbI₃, full molecular dynamics simulations were performed for

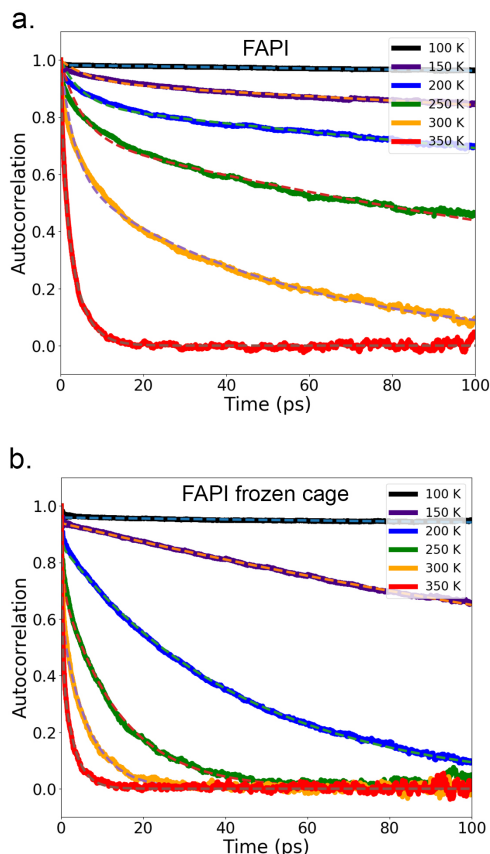


Figure 2.5 ACF for FAPbI. (a) ACF of the dipole direction averaged over 1000 dipoles for FA cations in a flexible lead iodide cage at temperatures ranging from 100 K to 350 K. (b) ACF of the dipole direction averaged over 1000 dipoles for FA cations in a frozen lead iodide cage at temperatures ranging from 100 K to 350 K.

FAPbI. A trajectory of the FA cations is obtained over 100 ps after equilibration of the system. The ACF averaged over the 1000 FA dipoles is shown as a function of time in Figure 2.5a. The simulations were performed at temperatures starting from 100 K to 350 K in steps of 50 K. The trends observed for FAPbI exhibit substantial differences compared to those presented above for MAPbI. The decay of the ACF shows a more gradual variation with temperature, indicating that in the same temperature range no strong phase transitions are observed. At 300 K and 350 K the rotation time for FA is larger than for MA as can be seen in Table 2.2. This contradicts some of the previous experimental and theoretical work where the rotation time for FA was of similar magnitude or smaller than for MA.^{23, 29-30} However, the rotation time at 350 K is already a lot faster implying that these differences could be a result of shortcomings in the force field, as already mentioned above. In order to unravel the different contributions to the observed rotational dynamics of FA in FAPbI we have performed the same model calculations as for MAPbI, as described below.

Table 2.2 ACF decay time constants for FA in picoseconds obtained after fitting the decay curves in Figure 2.5 using Equation 2.3. τ_1 corresponds to the faster decay time whereas τ_2 corresponds to the slower decay time constant.

T (K)	Flexible cage		Frozen cage	
	τ_1 (ps) (A1)	τ_2 (ps) (A1)	τ_1 (ps) (A1)	τ_2 (ps) (A1)
100	0.05 (0.02)	> 1000 (0.98)	0.05 (0.04)	> 1000 (0.96)
150	7.14 (0.08)	> 1000 (0.92)	0.04 (0.06)	271.73 (0.94)
200	5.24 (0.16)	510.27 (0.84)	0.23 (0.14)	45.12 (0.86)
250	5.21 (0.27)	195.40 (0.73)	0.45 (0.28)	14.21 (0.72)
300	3.41 (0.40)	52.63 (0.60)	0.31 (0.41)	6.60 (0.59)
350	0.77 (0.34)	3.62 (0.66)	0.27 (0.54)	2.89 (0.46)

2.3.2.1 Effect of cage deformation

The ACF for the motion of FA in a fixed Pb-I cage structure is shown as a function of time in Figure 2.5b. This figure and the rotation times in Table 2.2 show that also for the fixed cage, a gradual decrease in the rotation times is observed with increasing temperature. No abrupt changes due to phase transitions are formed. Comparison with Figure 2.5a shows that cage deformation leads to overall slower dynamics, as was also the case for MAPbI, however, the effect is not as pronounced as for MAPbI. Nevertheless, these simulations show that the deformation of the Pb-I cage also plays a significant role in the rotation dynamics in FAPbI.

2.3.2.2 Effect of dipole-dipole interactions

The effect of the dipole-dipole interactions on the FA alignment in FAPbI was again evaluated by comparing the size of the ordered domains formed at various temperatures for the three different simulation types. That is, MC simulations considering only dipole-dipole interactions, molecular dynamics with a frozen Pb-I cages and fully flexible molecular dynamics simulations. The average domain size for these three cases is plotted as a function of temperature in Figure 2.6.

In the case of the MC simulations where only dipole-dipole interactions are considered the domain size is unaffected by the temperature in the considered temperature range, implying that the dipole-dipole interactions are not large enough to affect the ion alignments. This is due to the much smaller dipole moment of the FA ion compared to the MA ion. This results in dipole-dipole interactions that are much smaller than $k_b T$ at the temperatures considered, and hence the thermal energy is high enough to prevent the formation of domains. This implies that the phase transition in FAPbI should not be affected by the dipole-dipole interaction of FA ions.

Interestingly, we observe an increase in domain size with lower temperatures for both molecular dynamics systems. This results in large domains at low temperatures, especially in the case of frozen cage. As we have excluded the possibility of a dipole-dipole effect it is likely that this happens due to some interaction between the ion and the cage that causes certain ion alignments to be more prominent than others.

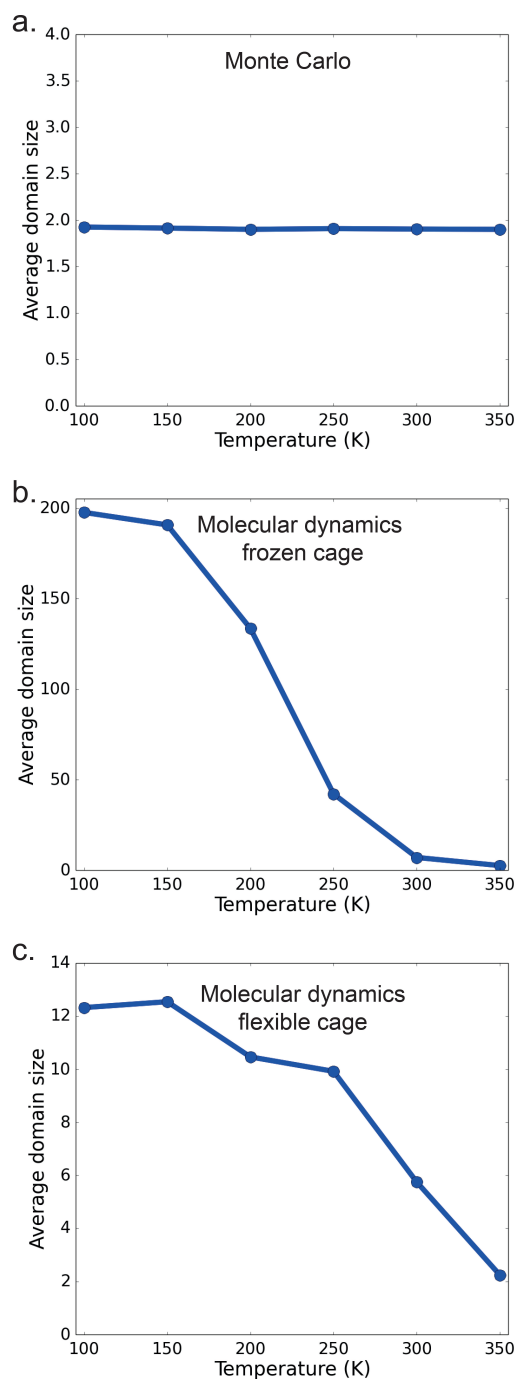


Figure 2.6 Average domain size vs temperature for formamidine dipoles simulated with (a) Monte Carlo only considering dipole-dipole interaction, (b) molecular dynamics with frozen lead iodide cage, (c) molecular dynamics with flexible lead iodide cage.

2.3.2.3 Effect of specific interactions between FA and cage

To further investigate to what extent the FA ions interact with the lead iodide cage we again look at scatter plots with all dipole directions of the FA ions in a single system, both for molecular dynamics simulations with frozen and flexible cage. The obtained results at 100 K, 200 K and 350 K can be observed in Figure 2.7.

For both simulations we can already see that the ion alignment is not completely random at high temperatures as there is higher density at certain angles. In both cases these are angles that lead to the dipole of the FA ion pointing in-between two iodides. This can be explained through hydrogen bonding between iodide and the hydrogens on the nitrogen molecules. If the dipole points between two iodides the nitrogens can point towards the iodides, allowing the hydrogen bonds to form. As the temperature is lowered these alignments become more prominent in both cases. This high degree of order in the FA orientation at low temperatures explains why large domains were observed for these systems above. If the ion alignments are restricted to only few possible orientations, large domains will be obtained even though the dipole-dipole interactions do not play any role in the alignment. One major difference is visible between the low temperature simulations for frozen and flexible cage. For the flexible cage the FA ions align both in the azimuthal plane and perpendicular to it. In the frozen cage simulations, the ions however only align in the azimuthal plane.

To gain insight in the timescale of the specific interaction we have again analyzed the hydrogen bond life-times as shown in Figure 2.4b. The lifetimes observed for FAPbI

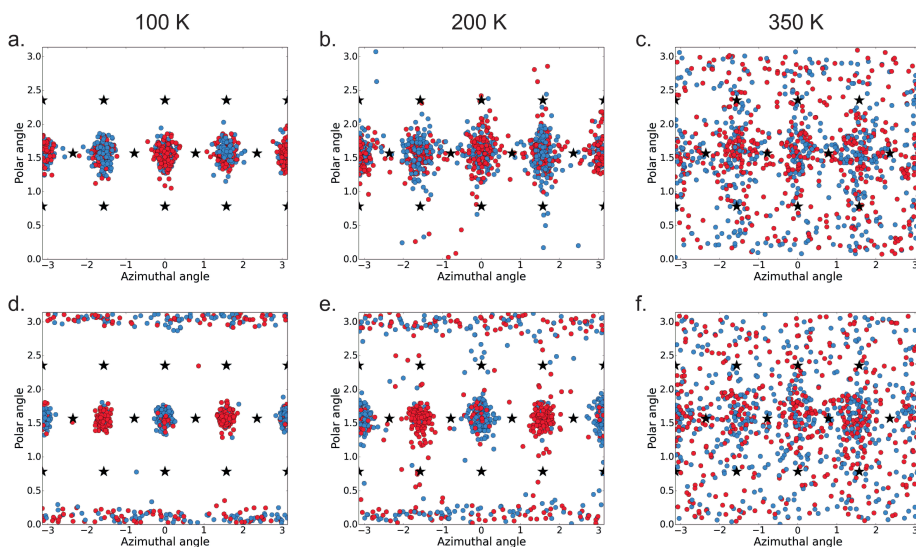


Figure 2.7 Orientations of all formamidinium dipoles in a single molecular dynamics system given in their polar and azimuthal angle. (a-c) frozen cage at 100 K, 200 K and 350 K and (d-f) flexible cage at 100 K, 200 K and 350 K. The stars in the figures represent the orientations where the dipole is oriented directly towards an iodide.

at low temperature are considerably longer than for MAPbI. One may interpret this as an indication of stronger hydrogen bonds, however, the lifetime is affected by all the interactions in the system, including steric hindrance that hampers the rotational motion of FA in the Pb-I cage, and effect due to cage deformation.

2.4 Conclusions

It is clear from the simulations presented above that the phase behavior and the rotational dynamics of the organic cation are intricately linked for both MAPbI and FAPbI. For MAPbI a very clear phase transition is observed at which the MA cation becomes immobilized, and at the same time the Pb-I lattice deforms. The phase transition is accompanied by the formation of domains in which the MA dipoles arrange in an ordered, energetically favorable structure. This domain formation is already observed if only the dipole-dipole interactions are taken into account but the effect becomes much stronger if the cations are embedded in the Pb-I lattice especially when the lattice is allowed to deform in reaction to the alignment. This points to a mechanism where phase transitions are induced by mutual alignment of the dipoles, both by interactions with neighboring dipole and specific interactions between the MA cations and the Pb-I lattice. This happens in a concerted way with the deformation of the Pb-I lattice, which strengthens this effect and makes the transition from freely rotating dipoles to ordered domains with fixed dipole directions more abrupt at certain temperature. This importance of the cage flexibility on the MA dynamics is in good agreement with previous experimental and theoretical work.³⁷⁻³⁸

For FAPbI a very similar picture emerges, however, in this case the dipole-dipole interactions in the non-dipolar FA cation are negligible. Simulations of the dipole dynamics in fixed, cubic Pb-I cage structures show that specific interaction between FA and the Pb and I ions, and between the quadrupolar FA ions, still lead to the formation of ordered domains, even if the Pb-I lattice is not allowed to deform. In the fully flexible MD simulations where full relaxation of the lattice is possible, this effect is strengthened and domain formation is more abrupt at a certain temperature. As discussed above, the formation of hydrogen-bond like conformations plays an important role in FAPbI, which, combined with increased steric interactions leads to slower rotation dynamics of FA in FAPbI.

We conclude that the phase transitions that occur in hybrid halide perovskites are caused by a complex interplay between dipole-dipole interactions, specific electrostatic and steric interactions between the organic cations and the metal halide lattice, and relaxation of the metal halide cage structure. This leads to large organized domains of organic cations, which can have important consequences for the electronic structure of these materials.

References

1. Brauer, J. C.; Lee, Y. H.; Nazeeruddin, M. K.; Banerji, N., Charge Transfer Dynamics from Organometal Halide Perovskite to Polymeric Hole Transport Materials in Hybrid Solar Cells. *J. Phys. Chem. Lett.* 2015, 6 (18), 3675-3681.
2. National Renewable Energy Laboratory (NREL) Best Research- Cell Efficiencies Chart. <https://www.nrel.gov/pv/cell-efficiency.html> (accessed 2020-06).
3. Shin, S. S.; Yeom, E. J.; Yang, W. S.; Hur, S.; Kim, M. G.; Im, J.; Seo, J.; Noh, J. H.; Seok, S. I., Colloidally Prepared La-Doped BaSnO₃ Electrodes for Efficient, Photostable Perovskite Solar Cells. *Science* 2017, 356 (6334), 167-171.
4. Umari, P.; Mosconi, E.; De Angelis, F., Infrared Dielectric Screening Determines the Low Exciton Binding Energy of Metal-Halide Perovskites. *J. Phys. Chem. Lett.* 2018, 9 (3), 620-627.
5. Leguy, A. M. A.; Frost, J. M.; McMahon, A. P.; Sakai, V. G.; Kockelmann, W.; Law, C.; Li, X.; Foglia, F.; Walsh, A.; O'Regan, B. C.; Nelson, J.; Cabral, J. T.; Barnes, P. R. F., The Dynamics of Methylammonium Ions in Hybrid Organic-Inorganic Perovskite Solar Cells. *Nat. Commun.* 2015, 6 (1), 7124.
6. Wu, X.; Trinh, M. T.; Niesner, D.; Zhu, H.; Norman, Z.; Owen, J. S.; Yaffe, O.; Kudisch, B. J.; Zhu, X. Y., Trap States in Lead Iodide Perovskites. *J. Am. Chem. Soc.* 2015, 137 (5), 2089-2096.
7. Weller, M. T.; Weber, O. J.; Henry, P. F.; Di Pumpo, A. M.; Hansen, T. C., Complete Structure and Cation Orientation in the Perovskite Photovoltaic Methylammonium Lead Iodide Between 100 and 352 K. *ChemComm.* 2015, 51 (20), 4180-4183.
8. Gélvez-Rueda, M. C.; Cao, D. H.; Patwardhan, S.; Renaud, N.; Stoumpos, C. C.; Schatz, G. C.; Hupp, J. T.; Farha, O. K.; Savenije, T. J.; Kanatzidis, M. G.; Grozema, F. C., Effect of Cation Rotation on Charge Dynamics in Hybrid Lead Halide Perovskites. *J. Phys. Chem. C* 2016, 120 (30), 16577-16585.
9. Bernard, G. M.; Wasylishen, R. E.; Ratcliffe, C. I.; Terskikh, V.; Wu, Q.; Buriak, J. M.; Hauger, T., Methylammonium Cation Dynamics in Methylammonium Lead Halide Perovskites: A Solid-State NMR Perspective. *J. Phys. Chem. A* 2018, 122 (6), 1560-1573.
10. Whitfield, P. S.; Herron, N.; Guise, W. E.; Page, K.; Cheng, Y. Q.; Milas, I.; Crawford, M. K., Structures, Phase Transitions and Tricritical Behavior of the Hybrid Perovskite Methyl Ammonium Lead Iodide. *Sci. Rep.* 2016, 6 (1), 35685.
11. Poglitsch, A.; Weber, D., Dynamic Disorder in Methylammoniumtrihalogenoplumbates (II) Observed by Millimeter-Wave Spectroscopy. *J. Chem. Phys.* 1987, 87 (11), 6373-6378.
12. Mattoni, A.; Filippetti, A.; Saba, M. I.; Delugas, P., Methylammonium Rotational Dynamics in Lead Halide Perovskite by Classical Molecular Dynamics: The Role of Temperature. *J. Phys. Chem. C* 2015, 119 (30), 17421-17428.
13. Guo, Y.; Yaffe, O.; Paley, D. W.; Beecher, A. N.; Hull, T. D.; Szpak, G.; Owen, J. S.; Brus, L. E.; Pimenta, M. A., Interplay Between Organic Cations and Inorganic Framework and Incommensurability in Hybrid Lead-Halide Perovskite CH₃NH₃PbBr₃. *Phys. Rev. Mater.* 2017, 1 (4), 042401.
14. Frost, J. M.; Butler, K. T.; Walsh, A., Molecular Ferroelectric Contributions to Anomalous Hysteresis in Hybrid Perovskite Solar Cells. *APL Mater.* 2014, 2 (8),

- 081506.
15. Li, J.; Rinke, P., Atomic Structure of Metal-Halide Perovskites from First Principles: The Chicken-and-Egg Paradox of the Organic-Inorganic Interaction. *Phys. Rev. B* 2016, 94 (4), 045201.
16. Bokdam, M.; Lahnsteiner, J.; Ramberger, B.; Schäfer, T.; Kresse, G., Assessing Density Functionals Using Many Body Theory for Hybrid Perovskites. *Phys. Rev. Lett.* 2017, 119 (14), 145501.
17. Lahnsteiner, J.; Kresse, G.; Kumar, A.; Sarma, D. D.; Franchini, C.; Bokdam, M., Room-Temperature Dynamic Correlation Between Methylammonium Molecules in Lead-Iodine Based Perovskites: An Ab Initio Molecular Dynamics Perspective. *Phys. Rev. B* 2016, 94 (21), 214114.
18. Carignano, M. A.; Kachmar, A.; Hutter, J., Thermal Effects on $\text{CH}_3\text{NH}_3\text{PbI}_3$ Perovskite from Ab Initio Molecular Dynamics Simulations. *J. Phys. Chem. C* 2015, 119 (17), 8991-8997.
19. Govinda, S.; Kore, B. P.; Bokdam, M.; Mahale, P.; Kumar, A.; Pal, S.; Bhattacharyya, B.; Lahnsteiner, J.; Kresse, G.; Franchini, C.; Pandey, A.; Sarma, D. D., Behavior of Methylammonium Dipoles in MAPbX_3 (X = Br and I). *J. Phys. Chem. Lett.* 2017, 8 (17), 4113-4121.
20. Selig, O.; Sadhanala, A.; Müller, C.; Lovrincic, R.; Chen, Z.; Rezus, Y. L. A.; Frost, J. M.; Jansen, T. L. C.; Bakulin, A. A., Organic Cation Rotation and Immobilization in Pure and Mixed Methylammonium Lead-Halide Perovskites. *J. Am. Chem. Soc.* 2017, 139 (11), 4068-4074.
21. Handley, C. M.; Freeman, C. L., A New Potential for Methylammonium Lead Iodide. *Phys. Chem. Chem. Phys.* 2017, 19 (3), 2313-2321.
22. Weller, M. T.; Weber, O. J.; Frost, J. M.; Walsh, A., Cubic Perovskite Structure of Black Formamidinium Lead Iodide, α - $[\text{HC}(\text{NH}_2)_2]\text{PbI}_3$, at 298 K. *J. Phys. Chem. Lett.* 2015, 6 (16), 3209-3212.
23. Fabini, D. H.; Siaw, T. A.; Stoumpos, C. C.; Laurita, G.; Olds, D.; Page, K.; Hu, J. G.; Kanatzidis, M. G.; Han, S.; Seshadri, R., Universal Dynamics of Molecular Reorientation in Hybrid Lead Iodide Perovskites. *J. Am. Chem. Soc.* 2017, 139 (46), 16875-16884.
24. Carignano, M.; Saeed, Y.; Aravindh, S. A.; Roqan, I. S.; Even, J.; Katan, C., A Close Examination of the Structure and Dynamics of $\text{HC}(\text{NH}_2)_2\text{PbI}_3$ by MD Simulations and Group Theory. *Phys. Chem. Chem. Phys.* 2016, 18 (39), 27109-27118.
25. Weber, O. J.; Ghosh, D.; Gaines, S.; Henry, P. F.; Walker, A. B.; Islam, M. S.; Weller, M. T., Phase Behavior and Polymorphism of Formamidinium Lead Iodide. *Chem. Mater.* 2018, 30 (11), 3768-3778.
26. Gallop, N. P.; Selig, O.; Giubertoni, G.; Bakker, H. J.; Rezus, Y. L. A.; Frost, J. M.; Jansen, T. L. C.; Lovrincic, R.; Bakulin, A. A., Rotational Cation Dynamics in Metal Halide Perovskites: Effect on Phonons and Material Properties. *J. Phys. Chem. Lett.* 2018, 9 (20), 5987-5997.
27. Bakulin, A. A.; Selig, O.; Bakker, H. J.; Rezus, Y. L. A.; Müller, C.; Glaser, T.; Lovrincic, R.; Sun, Z.; Chen, Z.; Walsh, A.; Frost, J. M.; Jansen, T. L. C., Real-Time Observation of Organic Cation Reorientation in Methylammonium Lead Iodide Perovskites. *J. Phys. Chem. Lett.* 2015, 6 (18), 3663-3669.

28. Chen, T.; Foley, B. J.; Ipek, B.; Tyagi, M.; Copley, J. R.; Brown, C. M.; Choi, J. J.; Lee, S.-H., Rotational Dynamics of Organic Cations in the CH₃NH₃PbI₃ Perovskite. *Phys. Chem. Chem. Phys.* 2015, 17 (46), 31278-31286.
29. Kubicki, D. J.; Prochowicz, D.; Hofstetter, A.; Péchy, P.; Zakeeruddin, S. M.; Grätzel, M.; Emsley, L., Cation Dynamics in Mixed-Cation (MA)_x(FA)_{1-x}PbI₃ Hybrid Perovskites from Solid-State NMR. *J. Am. Chem. Soc.* 2017, 139 (29), 10055-10061.
30. Taylor, V. C. A.; Tiwari, D.; Duchi, M.; Donaldson, P. M.; Clark, I. P.; Fermin, D. J.; Oliver, T. A. A., Investigating the Role of the Organic Cation in Formamidinium Lead Iodide Perovskite Using Ultrafast Spectroscopy. *J. Phys. Chem. Lett.* 2018, 9 (4), 895-901.
31. Zoete, V.; Cuendet, M. A.; Grosdidier, A.; Michielin, O., SwissParam: A Fast Force Field Generation Tool for Small Organic Molecules. *J. Comput. Chem.* 2011, 32 (11), 2359-2368.
32. Vanommeslaeghe, K.; Hatcher, E.; Acharya, C.; Kundu, S.; Zhong, S.; Shim, J.; Darian, E.; Guvench, O.; Lopes, P.; Vorobyov, I.; Mackerell Jr, A. D., CHARMM General Force Field: A Force Field for Drug-Like Molecules Compatible with the CHARMM All-Atom Additive Biological Force Fields. *J. Comput. Chem.* 2010, 31 (4), 671-690.
33. Vanommeslaeghe, K.; MacKerell, A. D., Automation of the CHARMM General Force Field (CGenFF) I: Bond Perception and Atom Typing. *J. Chem. Inf. Model.* 2012, 52 (12), 3144-3154.
34. Vanommeslaeghe, K.; Raman, E. P.; MacKerell, A. D., Automation of the CHARMM General Force Field (CGenFF) II: Assignment of Bonded Parameters and Partial Atomic Charges. *J. Chem. Inf. Model.* 2012, 52 (12), 3155-3168.
35. Plimpton, S., Fast Parallel Algorithms for Short-Range Molecular Dynamics. *J. Comput. Phys.* 1995, 117 (1), 1-19.
36. Frost, J. M.; Walsh, A., What Is Moving in Hybrid Halide Perovskite Solar Cells? *Acc. Chem. Res.* 2016, 49 (3), 528-535.
37. Liao, W.-Q.; Zhang, Y.; Hu, C.-L.; Mao, J.-G.; Ye, H.-Y.; Li, P.-F.; Huang, S. D.; Xiong, R.-G., A Lead-Halide Perovskite Molecular Ferroelectric Semiconductor. *Nat. Commun.* 2015, 6 (1), 7338.
38. Zhang, Q.; Solanki, A.; Parida, K.; Giovanni, D.; Li, M.; Jansen, T. L. C.; Pshenichnikov, M. S.; Sum, T. C., Tunable Ferroelectricity in Ruddlesden-Popper Halide Perovskites. *ACS Appl. Mater. Interfaces* 2019, 11 (14), 13523-13532.
39. Bischak, C. G.; Hetherington, C. L.; Wu, H.; Aloni, S.; Ogletree, D. F.; Limmer, D. T.; Ginsberg, N. S., Origin of Reversible Photoinduced Phase Separation in Hybrid Perovskites. *Nano Lett.* 2017, 17 (2), 1028-1033.

Appendix

Molecular dynamics parameters

The force field used for the molecular dynamics (MD) simulations here is composed of inorganic-inorganic interactions (U_{ii}) which are in between the Pb-I atoms. These parameters are composed of Buckingham potential. The U_{ii} parameters are mentioned in Table A2.1 described by Equation A2.1. The hybrid interactions (U_{io}) which are in between the Pb-I atoms and the organic cations are described by mix of both Buckingham and Lennard-Jones potential described by Equations A2.1 and A2.2. The hybrid interaction parameters are mentioned both in Table A2.1 and A2.2. Parameters for U_{ii} and U_{io} are taken from the previous work of Mattoni et. al. and Bischak et. al.^{12,39} The U_{oo} term contains the intermolecular and intramolecular interactions of the organic cations and is described by the CHARMM force field that includes bonds, angles, dihedrals and impropers where applicable.³²⁻³⁴ U_{oo} interaction parameters for methylammonium are mentioned in Table A2.4 and the parameters for formamidinium are mentioned in Table A2.6. The charges on each of these atoms are mentioned in Table A2.3 for methylammonium lead iodide and in Table A2.5 for formamidinium lead iodide. Both of these molecules have two different species of hydrogen where one is connected to Nitrogen (N) and another is connected to Carbon (C). These two types of hydrogens are named as H_c (connected to C) and H_N (connected to N).

$$E = Ae^{-r/\rho} - \frac{C}{r^6} \quad \text{A2.1}$$

$$E = 4\epsilon \left[\left(\frac{\sigma}{r} \right)^{12} - \left(\frac{\sigma}{r} \right)^6 \right] \quad \text{A2.2}$$

Table A2.1 Buckingham potential coefficients for each atom pair.

Pairs	A (Kcal/mole)	ρ (Å)	C (Å·Kcal/mole)
Pb – Pb	70359906.62970	0.131258	0.00
Pb – I	103496.13301	0.321737	0.00
I – I	22793.33858	0.482217	696.94954
Pb – N	32690390.93800	0.150947	0.00
Pb – C	32690390.93800	0.150947	0.00
I – N	112936.71421	0.342426	0.00
I – C	112936.71421	0.342426	0.00

Table A2.2 Lennard-Jones potential coefficients for each atom pair.

Pairs	ϵ (Kcal/mole)	σ (Å)	Pairs	ϵ (Kcal/mole)	σ (Å)
Pb – H_N	0.01400	2.26454	N – H_N	0.0517	2.60500
Pb – H_c	0.01400	2.70999	C – C	0.10940	3.39970
I – H_N	0.0574	2.75000	C – H_N	0.04140	2.23440
I – H_c	0.0574	3.10000	C – H_c	0.04140	2.67980
N – N	0.17000	3.25000	H_N – H_N	0.01570	1.06910
N – C	0.13640	3.32480	H_N – H_c	0.01570	1.51450
N – H_N	0.0517	2.15950	H_c – H_c	0.01570	1.96000

Table A2.3 Partial charges used for MAPbI.

Atom type	Pb	I	H _s	N	C	H _c
Charge	2.030	-1.130	0.540	-1.100	0.771	0.023

Table A2.4 Molecular parameters used for MA.

Bond Coefficients				
Bonds	K (Kcal/mole/ Å ²)		r ₀ (Å)	
C - H _c	342.991		1.093	
N - H _s	443.528		1.028	
C - N	276.638		1.48	
Angle Coefficients				
Angles	K (Kcal/mole/rad ²)		θ ₀ (°)	
H _c – C – H _c	37.134		108.836	
H _s – N – H _s	41.596		107.787	
H _s – N – C	41.452		111.206	
H _c – C – N	62.754		106.224	
Dihedral Coefficients				
Dihedrals	K (Kcal/mole)	n	d (°)	Weighing factor
H _s – N – C – H _c	0.13	3	0	0

Table A2.5 Partial charges used for FAPbI.

Atom type	Pb	I	H _{N1}	H _{N2}	N	C	H _c
Charge	2.030	-1.130	0.514	0.549	-0.759	0.515	0.238

Table A2.6 Molecular parameters used for FA.

Bond Coefficients				
Bonds	K (Kcal/mole/ Å ²)		r ₀ (Å)	
C - H _c	405.386		1.076	
N - H _n	485.340		1.014	
N - C	520.100		1.319	
Angle Coefficients				
Angles	K (Kcal/mole/rad ²)		θ ₀ (°)	
C - N - H _n	47.713		119.499	
H _n - N - H _n	25.548		117.729	
N - C - H _c	48.505		116.747	
N - C - N	61.531		126.476	
Dihedral Coefficients				
Dihedrals		K (Kcal/mole)	n	d (°)
H _n - N - C - N	1	0.137	1	0
	2	4.013	2	180
	3	0.346	3	0
H _n - N - C - H _c	1	-0.134	1	0
	2	4.038	2	180
	3	-0.403	3	0
Improper Coefficients				
Improper	K (Kcal/mole/rad ²)		χ ₀ (°)	
C - N - N - H _c	2.735		0	
H _n - C - H _n - N	1.439		0	

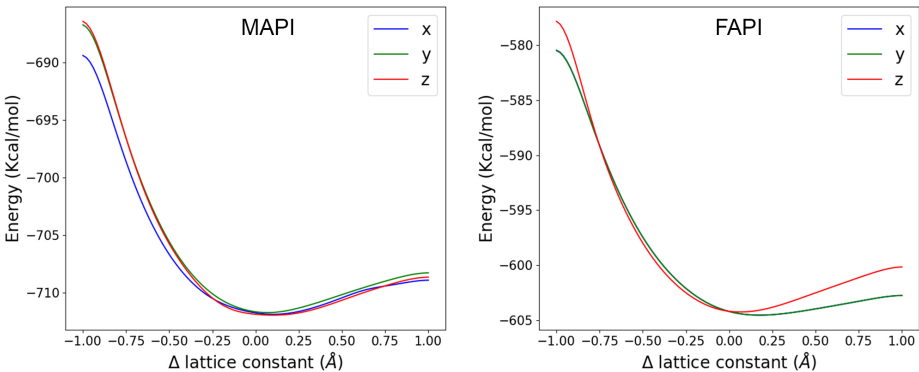


Figure A2.1 Model validation calculation, (left) energy with change of lattice constant for MAPI and (right) energy with change of lattice constant for FAPI.

Directional scatter plots

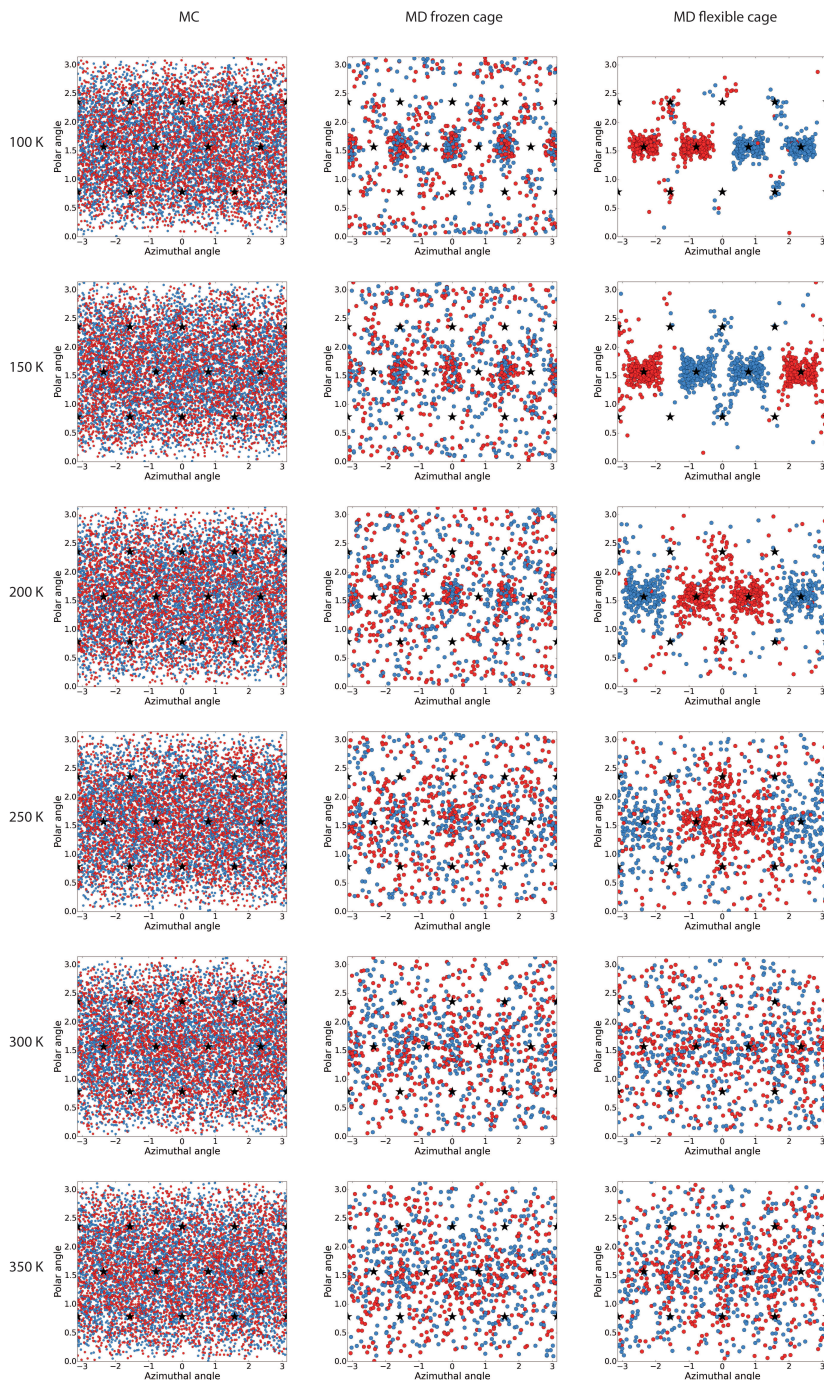


Figure A2.2 Directional scatter plots of Methylammonium dipoles simulated with MC, MD with frozen cage and MD with flexible cage. The temperature ranges from 50 K to 350 K with a 50 K interval.

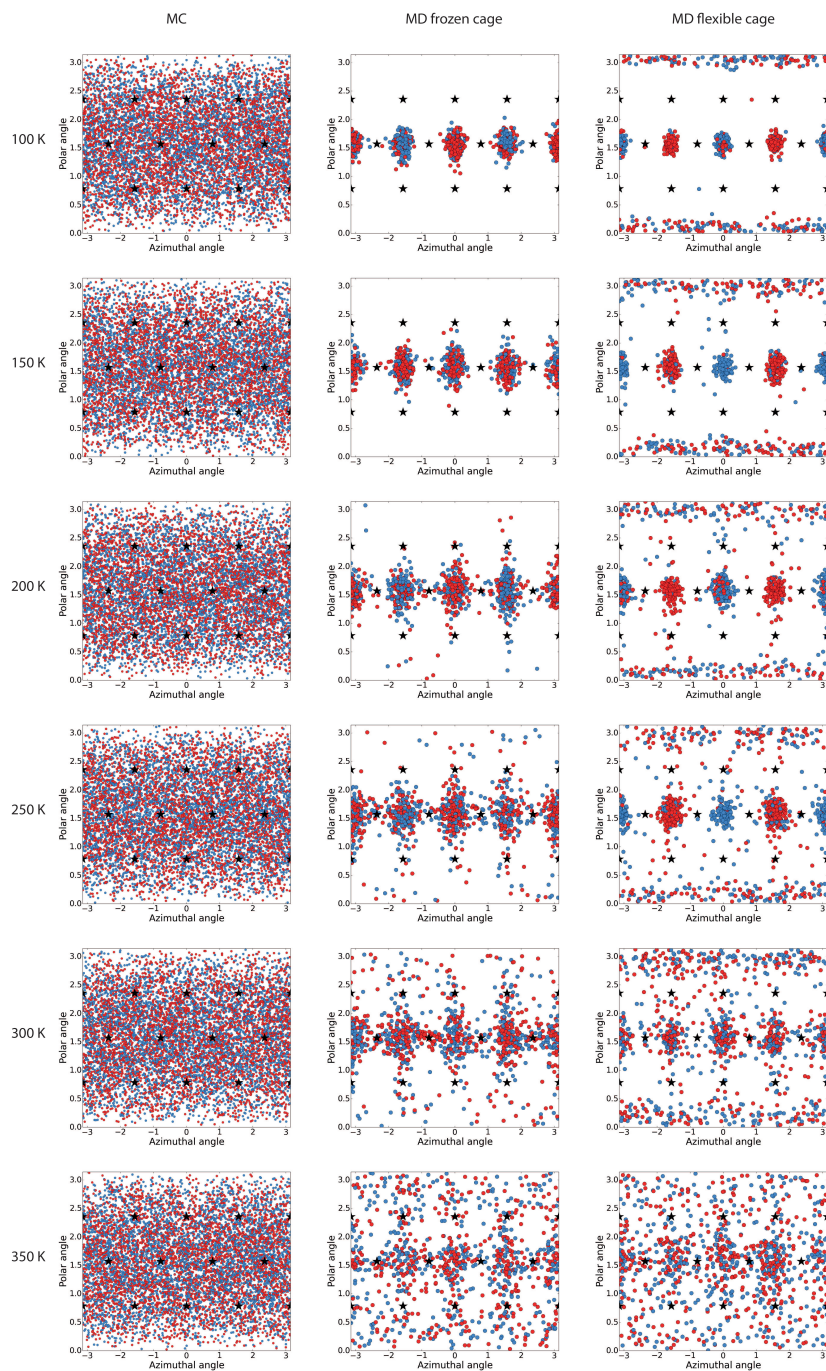


Figure A2.3 Directional scatter plots of Formamidinium dipoles simulated with MC, MD with frozen cage and MD with flexible cage. The temperature ranges from 50 K to 350 K with a 50 K interval.

3



Structural Dynamics of Two-Dimensional Ruddlesden-Popper Perovskites: A Computational Study

Recently two-dimensional (2D) hybrid organic-inorganic perovskites have attracted a lot of interest as more stable analogues of their three-dimensional counterparts for opto-electronic applications. However, a thorough understanding of the effect that this reduced dimensionality has on dynamical and structural behavior of individual parts of the perovskite is currently lacking. In this chapter we have used molecular dynamics simulations to investigate the structure and dynamics of 2D Ruddlesden-Popper perovskite with the general formula $\text{BA}_2\text{MA}_{n-1}\text{Pb}_n\text{I}_{3n+1}$, where BA is butylammonium, MA is methylammonium and n is the number of lead-iodide layers. We discuss the dynamic behavior of both the inorganic and the organic part and compare between the different 2D structures. We show that the rigidity of the inorganic layer markedly increases with the number of lead-iodide layers and that low temperature structural phase changes accompanied by tilting of the octahedra occurs in some but not all structures. Furthermore, the dynamic behavior of the MA ion is significantly affected by the number of inorganic layers, involving both changes in the reorientation times and in the occurrence of specific preferred orientations.

3.1 Introduction

Over the past few years hybrid halide perovskite materials have attracted a lot of interest due to their impressive properties as photovoltaic materials.¹⁻³ This has led to high-efficiency solar cells, reaching efficiencies over 25%,⁴ but applications in light-emitting diodes (LEDs),⁵⁻⁷ photodetectors,⁸⁻⁹ lasers^{6,10} and radiation detectors¹¹⁻¹³ are also rapidly emerging. Perovskites are characterized by a general ABX_3 structure where A is a monovalent cation, often organic (methylammonium, formamidinium, cesium), B is a divalent cation (lead, tin) and X is a monovalent halide anion (iodide, bromide). The most studied perovskite for photovoltaic applications is $(CH_3NH_3)PbI_3$ or methylammonium lead iodide (MAPbI). In this material the A cation is the organic cation methylammonium (MA).

One of the major drawbacks of perovskites is that they are very sensitive towards air and moisture, causing a rapid degradation of devices when they are not properly encapsulated.¹⁴⁻¹⁵ A possible approach to counter this is replacing (part of) the MA by a large organic cation, leading to a two-dimensional (2D) structure.¹⁶⁻²¹ The large organic cation breaks up the structure in 2D layers of inorganic Pb-I octahedra separated by the large organic cations. The hydrophobic nature of the organic component protects the material from air and moisture, resulting in a higher stability.^{17-18, 22-23} The most common 2D perovskites are Ruddlesden-Popper type materials that have a general $(R-NH_3)_2A_nB_nX_{3n+1}$ structural formula.^{16,21} In these structures, A, B and X are the same as in the case of the 3D perovskite, but $R-NH_3^+$ is a large monovalent ammonium cation that does not fit inside the 3D perovskite structure, and hence is responsible for breaking up the structure into layers. Since the large cation does not have to fit into the inorganic metal-halide cage structure, there is considerable freedom in size and nature. The most common choices at present are the commercially available phenylethylammonium (PEA)²⁴⁻²⁵ or aliphatics like n-butylammonium (BA),^{16, 18, 21} but there are also examples of the incorporation of large conjugated molecules.²⁶⁻³⁰ By modifying the ratio between the large $(R-NH_3)$ and the small (A) organic cation it is possible to systematically vary the number of inorganic perovskite layers (n) between each spacer layer of the large organic cations. This tuning of the layer thickness is accompanied by changes in the opto-electronic properties.²¹ When $n = 1$, there is no small A-cation present and a single layer of Pb-I octahedra is sandwiched between the large organic cations. For large values of n the number of inorganic perovskite layers in between the organic layers increases, but at the same time small organic cations are introduced in the materials. These changes have a large effect on the local environment of the individual molecules in the system. The optoelectronic properties (exciton diffusion, fluorescence quantum yield) are intricately linked to the (dynamic) structural properties of the 2D layers in the material.³¹ As shown recently, structural variations in the layer of large organic cations or altering the number of inorganic layer can result in significant changes in the exciton diffusion properties,³²⁻³³ which is believed to be a result of differences in the rigidity of the 2D structure. Therefore, it is of considerable interest to explore the structural dynamics of 2D perovskites and how it depends on the number of inorganic layers.

In this chapter we have performed model potential molecular dynamics (MD) simulations on 2D Ruddlesden-Popper perovskites with varying number of inorganic layers ($n = 1 - 4$), as well as on the corresponding 3D perovskite. In all cases lead and iodide form the

inorganic layer and where appropriate the large cation is BA and the small cation is MA. We have studied the effect of the number of layers on the individual parts of the structure; the inorganic layer, the small organic cation and the large organic cation. In this way we gain insight in the rigidity of the inorganic layer, the mutual angles of the octahedra and the rotational diffusion of the small and large organic cations. These simulations indicate that the interplay between the dynamics of the inorganic lattice and the organic cations is very subtle and that the behavior of the different parts of the materials are strongly interconnected. The presence of the organic cations has a pronounced effect on the structure of the inorganic lattice, but the motion of the organic cations is also strongly correlated with distortions of the inorganic lattice. The results show that it is possible to tune the distortions in the inorganic lattice by changing the organic cations but increasing the layer thickness of the inorganic part generally makes the lattice more rigid. Both the average structure and rigidity of the inorganic lattice and the rotational dynamics of the organic cations will affect the electronic structure of the materials.³⁴⁻³⁶

3.2 Methods

All molecular dynamics simulations were performed using the LAMMPS software.³⁷ We have adopted the force field from the work of Mattoni et. al.³⁸ on 3D methylammonium lead iodide. In this force field the interactions between Pb and I are described with a Buckingham potential, while the organic-organic, interaction are described by Lennard-Jones terms which are derived from the standard Amber force field.³⁹ The inorganic-organic interactions are described by either Lennard-Jones (when hydrogen is involved) or a Buckingham potential. In order to make the force field transferrable between the different materials that we consider, we deviate from the Mattoni force field in one respect: the partial charges for the Coulomb interactions. We assign the full formal charges +2 and -1 to the lead and iodide ions (versus +2.02 and -1.13 in the Mattoni force field). In addition, the organic cations have a full +1 charge that is distributed over all atoms as obtained from an electronic structure calculation. This leads to small deviations as can be seen if the results for 3D perovskite are compared to our previous work which did not use full formal charges.⁴⁰ This leads to a decrease of the temperature at which the phase transition is observed (Figure A3.1). We have explicitly chosen to adapt the way charges are assigned to the individual ions because this leads to a straightforward transferrable force field that can be adapted easily to structures for different *n* and other organic cations. We recognize that this may affect the detailed description, for instance of phase transitions, however, it does make it possible to make a direct qualitative comparison between different related structures. The latter would not be possible if the force field was optimized for each compound individually.

The partial charges on the individual atoms in MA and BA were obtained by fitting them to the electrostatic potential from a density functional theory calculation (B3LYP/cc-pVQZ) using the CHelpG approach⁴¹ in the Gaussian09 software.⁴²

The initial structures used for the 2D perovskites and the 3D perovskite were obtained from experimental crystal structures.^{21, 43} In the case of the 3D perovskite the simulations were performed on a super cell of 10×10×10 unit cells, while for the 2D perovskite a super cell of 10×10 unit cells was used. The direction perpendicular to the lead-iodide layer was

not replicated for the 2D systems, but it should be noted that the unit cell already contains two Pb-I layers. In all cases periodic boundary conditions were used in all directions and the volume is kept constant.

For all simulations an initial temperature of 400 K is used where the system is allowed to equilibrate for 1 ns with a time step of 1 fs. This time step was used throughout all simulations discussed. After the equilibration the temperature is lowered to the desired temperature with a fixed annealing rate of 125 K/ns. Once the desired temperature is reached, the system is again allowed to equilibrate for 1 ns before a 100 ps production run is performed. Throughout the production run the positions of all atoms is recorded.

3.3 Results and discussion

In order to gain insight in the structural and dynamical properties of 2D Ruddlesden-Popper perovskites we have performed a series of MD simulations as outlined above. Following these MD simulations, we now analyze the trajectories that were obtained in order to compare their structural features. More specifically we want to understand what the effect will be on the rigidity of the lead-iodide layers and the orientation and motion of the MA and BA ions. We start by focusing on the lead-iodide layer and its rigidity, after which we discuss the dynamics of the organic component.

3.3.1 Structure and dynamics of the Pb-I lattice

In order to compare the rigidity of the lead-iodide layer between different structures we compare the positions of the lead atoms throughout the simulations. For each simulation the coordinates of every lead atom at every time step is extracted and a histogram of the out of layer coordinate (the z-coordinate) is made. Depending on the initial structure, the histograms will differ in number and positions of peaks. However, each peak will in all cases represent a single layer of lead ions in the structure. Every peak is fitted with a simple Gaussian function and the standard deviation extracted. The latter is an indicator of the structural flexibility of the lead atoms in each layer. In a more rigid layer, the movement of the lead atoms in the direction perpendicular to the layer will be diminished and therefore give rise a narrower peak with a smaller standard deviation. This procedure is illustrated in Figures 3.1a-c with an example of a histogram and a fit, while in Figure 3.1d the average standard deviation of each structure is plotted as a function of temperature.

In Figure 3.1d it can be seen that lowering the temperature leads to the expected trend of a reduced movement of the lead atoms around their equilibrium position. Furthermore, at high temperatures the general trend is that the movement of lead atoms decreases on increasing the number of lead-iodide layers. This shows that increasing the number of stacked lead-iodide layers makes the structure more rigid. At 50 K, the lowest temperature simulated, all the structures except for the $n = 1$ material exhibit a more or less identical standard deviation of the position of the lead atoms.

While all the other structures have a similar change in standard deviation with temperature, for the $n = 1$ the dependence on temperature is much stronger. This results in a substantial difference between the $n = 1$ and the other structures at higher temperatures. Moreover, the gap between the standard deviations in the Pb positions between $n = 1$ and $n = 2$

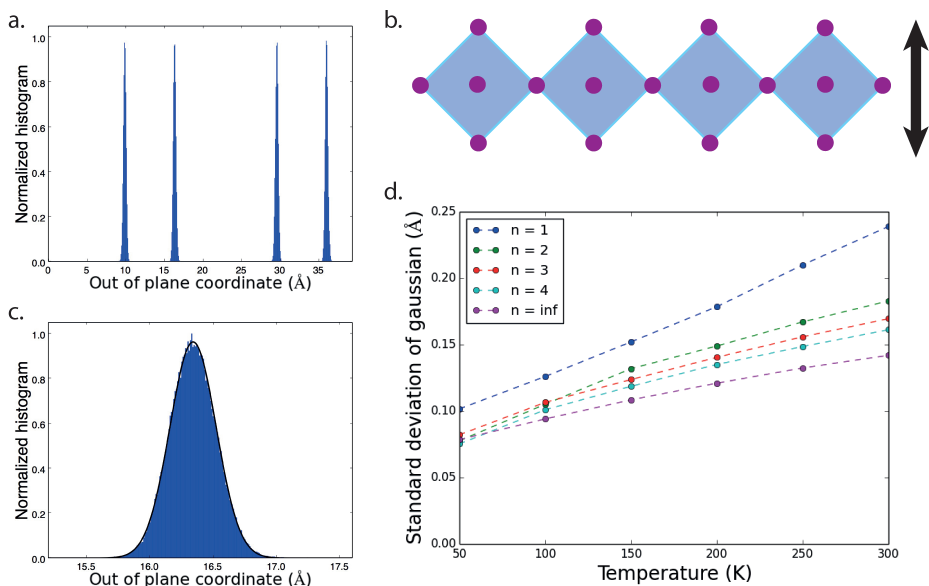


Figure 3.1 Motion of lead atoms. (a) Histogram of out of layer coordinates for an $n = 2$ simulation. (b) Lead-iodide octahedral layer with the out of layer direction highlighted. (c) Single peak from the histogram at close with a fitted gaussian. (d) The average standard deviation of the fitted gaussian for each structure versus temperature.

is much larger than between all other structures. This shows that the $n = 1$ structure is considerably less rigid than the $n > 1$ structures at all temperatures.

To obtain a more detailed understanding of the effects of temperature on the structure of the inorganic framework of the different RP compounds we have examined the average Pb-I-Pb angles as a function of the temperature (Figure 3.2). The Pb-I-Pb angle corresponds to the mutual angle between two neighboring octahedra and will therefore give an indication of the tilting of the octahedra in each structure. In a perfectly cubic structure the Pb-I-Pb angle will be 180° , but any tilting will result in a smaller angle, and the smaller the angle is the more tilted the octahedra are. Furthermore, due to thermal motion, a cubic structure will show a slightly lower average Pb-I-Pb angle than 180° . We make a distinction between the Pb-I-Pb angles that are present in the lead-iodide layers (Figure 3.2a) and the Pb-I-Pb angles that are perpendicular to the lead-iodide layers (Figure 3.2b) and we also show the standard deviations for both sets of angles in Figure 3.2c and Figure 3.2d. The Pb-I-Pb angles within the lead-iodide layer are two separate angles, but as can be seen in Figure A3.3 in the Appendix there is no difference between these two angles in the simulated structures.

The first clear trend observed from Figure 3.2a is that the average Pb-I-Pb angle in the layer approaches 180° as the number of lead-iodide layers increase. It is also clear that the tilting of the octahedra in the $n = 1$ structure is substantially more pronounced than in their counterparts with $n > 1$. This can be seen from the large gap in average Pb-I-Pb

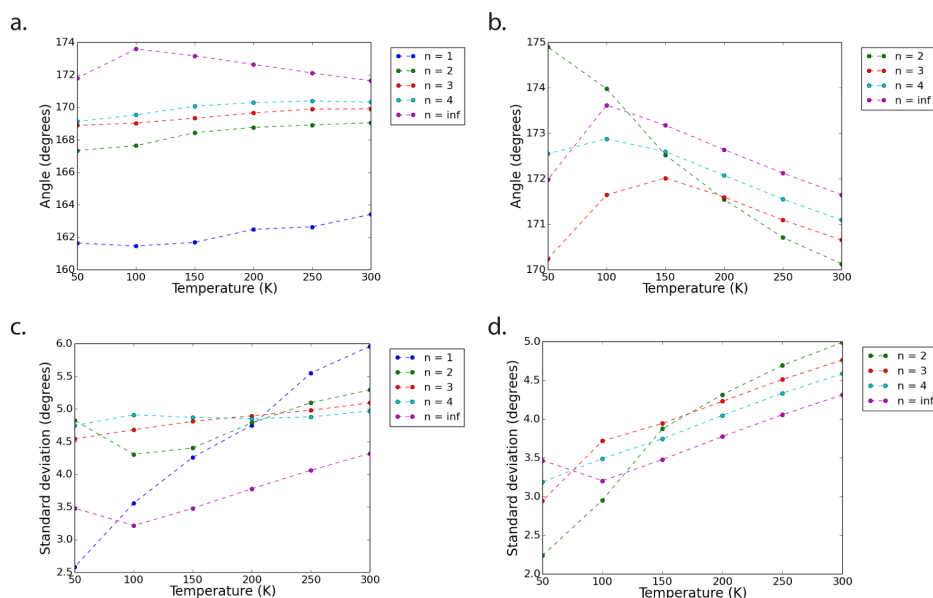


Figure 3.2 Pb-I-Pb angles in the different simulated structures. (a) Average Pb-I-Pb angles in the lead-iodide layer. (b) Average Pb-I-Pb angles perpendicular to the lead-iodide layer. (c) The standard deviation of the Pb-I-Pb angles in the lead-iodide layer. (d) The standard deviation of the Pb-I-Pb angles perpendicular to the lead-iodide layer.

angle for the $n = 1$ as compared to all other structures. As the temperature is lowered all the 2D structures show a similar gradual decrease in the average angle. The exception to this trend is the 3D perovskite where the average angle initially increases gradually before decreasing significantly between 100 K and 50 K. The gradual increase can be due to structural changes but can also be a result of statistical effects as noted above. The initially decreasing temperature leads to a reduction in the thermal motion of the resulting in an average angle closer to the optimal Pb-I-Pb angle of the structure, which is close to 180° . The sudden decrease in the average angle between 100 K and 50 K can however not be explained by such statistical effects and must therefore be due to distinct structural changes in the materials, a phase transition. This is well-known for 3D perovskites but happens at higher temperatures than observed in these simulations.⁴³

The Pb-I-Pb angle perpendicular to the lead-iodide layer for the 3D perovskite (Figure 3.2b) shows exactly the same behavior that in the lead-iodide layer. This is not surprising since the 3D perovskite is not a layered structure and all three principle directions are roughly equivalent. For the 2D structures, however, significant differences arise between the perpendicular and the in-layer angles. Firstly, all compounds show a larger Pb-I-Pb angle in the direction perpendicular to the lead-iodide layer than in the layer at all temperatures. Secondly, decreasing the temperature has a very different effect. The $n = 3$ and $n = 4$ now behave more like the 3D structure, where at first the angle increases and then at a specific temperature it decreases. For the $n = 4$ the decrease happens between 100 K and 50 K and is very small. Therefore, it is difficult to say whether this is due to a phase

transition in the material or a slight alteration in optimal angles. In the case of the $n = 3$ the decrease in the angle is more profound, starting with a slight decrease between 150 K and 100 K followed by a steeper decrease between 100 K and 50 K. This is very similar to the behavior of the 3D perovskite and suggests that the $n = 3$ goes through a phase transition at similar temperatures as the 3D perovskite. The $n = 2$ structure exhibits a very different behavior. In this case, the Pb-I-Pb angle increases steadily with decreasing temperature, indicating less tilting of the octahedra.

The $n = 1$ structure has no Pb-I-Pb angle perpendicular to the lead-iodide layer. In order to show some comparison of the out-of-layer tilting of that structure versus the other structures we define an angle between the lead iodide plane and the out-of-layer iodides, see Figure A3.2 in the Appendix. This analysis shows that the $n = 1$ has the largest tilting in the out-of-layer direction by some margin as it does in the in-layer direction (Figure 3.2a), i.e. the structure is more flexible overall.

From Figures 3.2c and 3.2d it can be seen that the standard deviation of the angles decreases in most cases with the temperature, as we would expect from the decreased motion of the atoms. There are however some notable exceptions. For instance, the standard deviation for the 3D perovskite becomes slightly larger when the material goes through its phase transition. This can be explained by the definition of the angle adopted here. Since the Pb-I-Pb angle is defined in the range from 0° - 180° the distribution of angles is one-sided when the optimal angle is close to 180° . If the optimal angle shifts to a slightly lower angle the distribution will become two-sided and therefore a bit broader.

3.3.2 Rotational dynamics of the methylammonium

The structure and dynamics of the inorganic Pb-I lattices are intricately linked to the presence and dynamics of the organic cations. Therefore, we now turn to the MA ions and their dynamics in the different structures. To compare the rotational dynamics of the MA ions we evaluate the rotational autocorrelation function (ACF) of the MA ions averaged over the number of MA ions (N_{ion}) and over all possible initial times t_0 during the simulation time (N_{t_0}).

$$A(t) = \langle \hat{n}(t) \cdot \hat{n}(0) \rangle = \frac{1}{N_{ion}} \sum_i \frac{1}{N_{t_0}} \sum_{t_1=t+t_0} \hat{n}_i(t_1) \cdot \hat{n}_i(t_0) \quad 3.1$$

The ACF gives an indication of whether the MA ions can rotate freely and on the time scale at which they reorient. If the MA ions are fully free to rotate and can obtain any orientation the ACF value will decay to zero, indicating a random distribution of directions, on average. The time scale on which this happens is the rotational diffusion time. However, if the rotational motion is restricted, for instance by directional interactions with the Pb-I lattice, the ACF will not fully decay to zero but saturate at a certain value. This saturation value indicates how much freedom the MA ion has to move around. In Figure 3.3 the ACF of the MA ions in the structure that include MA ions is shown at the following temperatures: (a) 300 K, (b) 150 K, (c) 100 K, and (d) 50 K. The reason we focus more on the lower temperatures is that at high temperature there is no significant change in behavior with temperature.

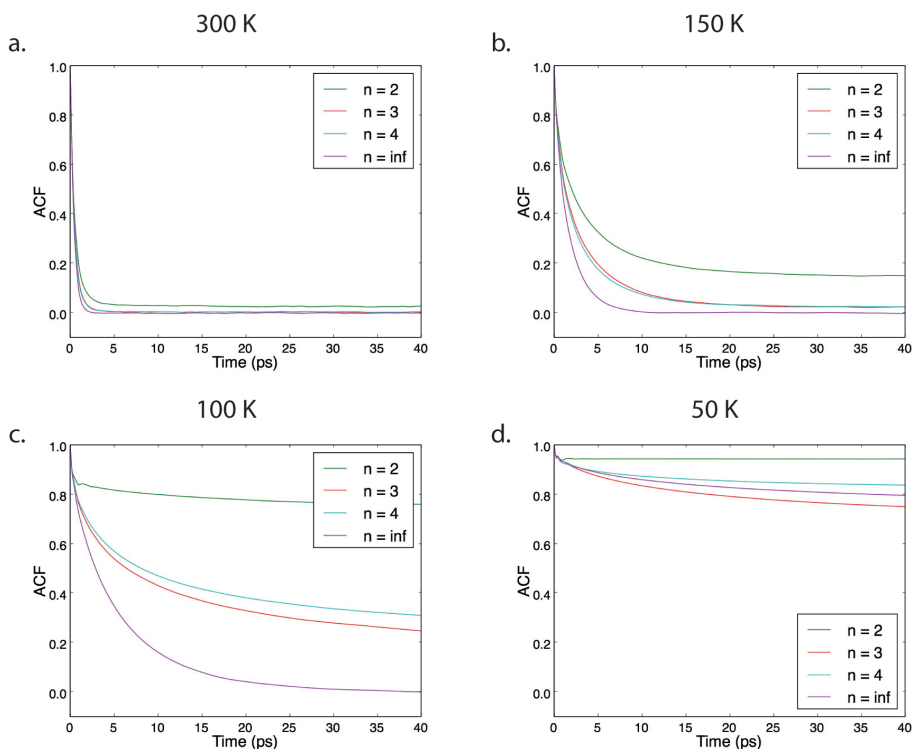


Figure 3.3 Rotational autocorrelation function for MA ions in the different structures. (a) 300 K, (b) 150 K, (c) 100 K and (d) 50 K.

As can be seen from Figure 3.3a, the ACF reaches a plateau within the first 5 ps for all structures at 300 K. The most interesting observation is that for the $n = 2$ structure the ACF does not fully decay to zero. This means that at this temperature the rotation of the MA ions in the $n = 2$ material is not completely free and some forbidden orientations exist. The data in Figure 3.3 also shows that for all temperatures the $n = 2$ structure always has the highest ACF value, by some margin. This indicates that the MA ions in this structure have the least freedom to rotate as compared to the other compounds. This is interesting since in the $n = 2$ structure the environment in which the MA ions rotate differs considerably from the other structures. In this material, each MA layer is flanked by two BA layers on each side, while the MA layers in the structures with $n > 2$ have at least one layer of MA as a neighbor, at least on one side. This indicates that the neighboring MA layers increase each other ability to move freely around.

At 150 K, shown in Figure 3.3b, we see that for the $n = \infty$ structure the ACF decays to zero within roughly 10 ps, while for $n = 3$ and $n = 4$ the decay is slower and saturates at a value above zero, indicating some preferential orientations. Interestingly, the plateau value of the ACF is almost identical at this temperature for $n = 3$ and $n = 4$. If the temperature is lowered even more, to 100 K, we see that $n = \infty$ still decays fastest and reaches zero in

roughly 40 ps. In addition, at this temperature the ACF of the $n = 3$ decays faster than the ACF for the $n = 4$ structure. This is the same temperature as we earlier saw changes in the octahedral tilting of the lead-iodide lattice for the $n = 3$ structure. This indicates that this structural change affects the motion of the MA ions in a positive way, giving them more freedom to rotate than they would otherwise have.

When considering the results at 50 K in Figure 3.3d, we see that the ACF of $n = 3$ still decays to a lower value than for $n = 4$ and is now also lower than the one for $n = \infty$. The $n = \infty$ structure has a significantly higher ACF plateau value at this temperature and the MA ions seem now much more static than before. This occurs at the same temperature where we previously saw the average Pb-I-Pb angle change and is consistent with a phase transition occurring in the material.^{38,40} The structural changes of both $n = 3$ and ∞ seem to affect the motion of their MA ions but in opposite fashion. In the case of the $n = 3$ the ACF value decays faster compared to the $n = 4$ structure meaning more movement of the MA ions while for $n = \infty$ the ACF gets higher and saturates at higher value than the $n = 3$ structure, indicating significantly less movement. This shows that the relation between structural changes and MA movement is not straightforward.

In order to analyze the dynamics and behavior of the MA ions in the different structures in more detail, we plot in Figure 3.4 normalized heat maps indicating the occurrence of different directions of the MA ions in terms of the polar and azimuthal angles, throughout a simulation at 300 K and 50 K. On the heat maps we have also plotted the relative positions of iodides and leads with respect to the MA ions based on the initial structure of the system. The normalization is done to compensate for the fact that we are plotting spherical surface on rectangular grid, and results in all values larger than one to represent higher density of MA ions than random distribution would predict and values lower than one representing less density than if the ions were distributed randomly.

If we first focus on the 300 K simulation for $n = \infty$ we see six high-density areas indicating preferential orientations of the MA ions. These areas correspond to structures where the CN axis of MA points to centers of the facets of the tetragonal lead-iodide surroundings. The reason that these orientations are preferred over others is the possibility of forming hydrogen bonding between the hydrogens on the MA nitrogen atoms and the iodides in the Pb-I layers. At high temperatures these hydrogen bonds are short lived and after they break up, the MA ion can jump to the next iodide forming a new hydrogen bond. These jumps happen rapidly and seem to happen primarily within a lead-iodide facet, resulting in a high-density of MA ions pointing toward each facet.

For $n = \infty$ the six tetragonal facets are roughly equivalent as the organic cation on the other side of the facet is always another MA ion. This is not the case for the 2D structures where the top and bottom facet have, either in all or most cases, at least one BA ion as a neighbor. These structures also show different behavior than the $n = \infty$ material at high temperatures, where top and bottom facets are less occupied than the others. This becomes increasingly visible when the number of layers is decreased. The $n = 2$ structure has even less MA ions pointing to the top and bottom facets than random orientation predicts. This is caused by the repulsion with the BA ions that are in a fixed global orientation

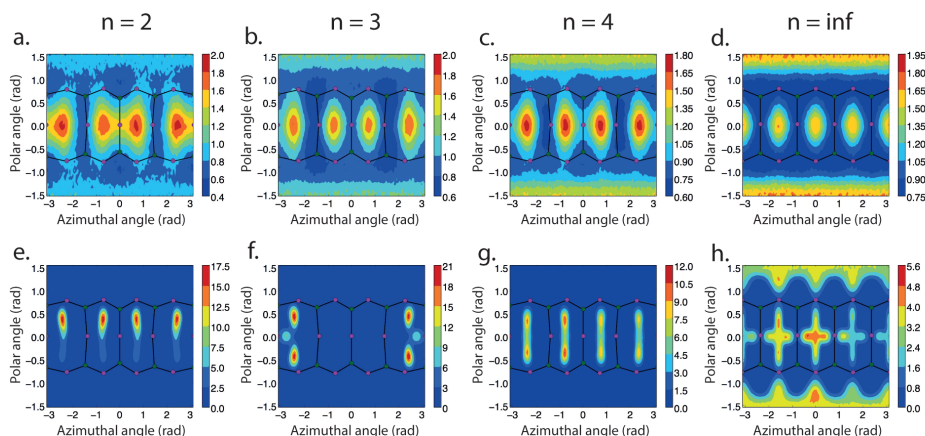


Figure 3.4 Normalized heat maps of MA ion directions in the structures examined at 300 K (top row) and 50 K (bottom row). (a) $n = 2$ at 300 K, (b) $n = 3$ at 300 K, (c) $n = 4$ at 300 K, (d) $n = \infty$ at 300 K, (e) $n = 2$ at 50 K, (f) $n = 3$ at 50 K, (g) $n = 4$ at 50 K, (h) $n = \infty$ at 50 K.

with respect to the Pb-I layers. As a result, the MA ions are prevented from taking certain orientation and explains why the ACF for $n = 2$ does not reach a plateau at zero.

If we now focus on the 50 K heat maps, we see that the $n = \infty$ structure has a similar MA ion distribution as at 300 K in the sense that still all the orientations are available for the MA ions. What is different in this case is that we clearly see higher density of MA ions next to the iodides where the hydrogen bonds are formed. This happens since at low temperature, the thermal motion of the MA ions is reduced and the hydrogen bonds live longer. Therefore, the MA will spend more time at the most preferred position, next to the iodide.

For all the other structures the difference between the high and low temperature is clearer. In all the cases the top and bottom facets are more or less unoccupied at 50 K, meaning that almost no MA ions point in this direction at low temperatures. The high-density areas next to the iodides are also clearer than for the $n = \infty$ and for the occupied facets not all positions next to iodide have high density. For the $n = 2$ only the position next to the top iodide is highly occupied with some minor occupation next to the lower iodides, meaning that the MA ions are really fixed in a certain orientation and rarely move to another orientation. This is consistent with the decay of the ACF for $n = 2$ structure at 50 K, which showed very little decay, see above. For the $n = 4$ structure the preferred orientations are very similar to the $n = 2$ material. The main difference is that the alignment next to the bottom iodide is now roughly equally probable as the alignment next to the top iodide. We also see that between these preferable areas there is a path with some occupancy, this implies that over the course of the simulation all or some of the MA ions manage to jump between these positions. This explains why the ACF of the $n = 4$ compound reaches a plateau at a significantly lower value than for $n = 2$.

Once again, the $n = 3$ structure shows a somewhat different behavior compared to the others. For some reason the $n = 3$ structure only has MA occupancy in two tetragonal facets. We attribute this to the observed structural changes in the Pb-I lattice, accompanied by octahedral tilting at low temperatures, as seen in the change in the average Pb-I-Pb angles in Figure 3.2b. As the octahedra tilt, certain orientations of the MA ion become preferable because of steric effects. As was the case for $n = 4$ the areas next to the top and bottom iodide are the preferred areas and there is a path with some occupancy between the two. The difference is that now there is an area on the path next to one of the middle iodides, which also has an appreciable occupancy. This means that when the MA ion is jumping between favorable positions next to the top and bottom iodide it can occupy an intermediate orientation in the case of $n = 3$. This decreases the energy barrier needed to make the jump and therefore allowing the MA ion to move more rapidly between the preferred areas. This explains why the $n = 3$ structure has the lowest ACF plateau at 50 K.

3.3.3 Rotational dynamics of the butylammonium

Finally, we consider whether there is any difference in the behavior of the BA ions for the different structures. To do this we compare the ACF of the N-C bond in BA for the different structures at some of the simulated temperatures in Figure 3.5. It is important to keep in mind that these ACF plots will differ from the ones for the MA ions. The MA ion is

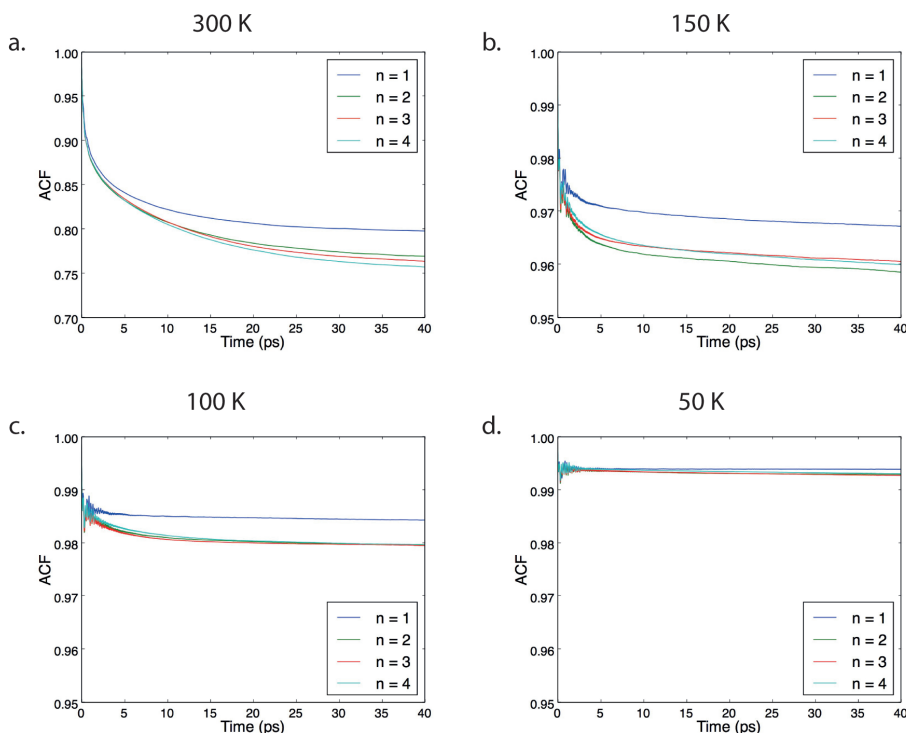


Figure 3.5 Rotational autocorrelation function for N-C bond in BA ions in the different structures. (a) 300 K, (b) 150 K, (c) 100 K and (d) 50 K.

small ion that can rotate relatively freely as long as nothing hampers it. The BA ion on the other hand is bulkier and is only surrounded by Pb-I on one side. Therefore, it cannot reorient completely and ACF will not reach zero at any temperature.

When comparing the ACF for BA in the different structures the main observation is that the $n = 1$ structure plateaus at significantly higher ACF value than the other structures, and thus reorients less. This surprising observation is related to the lack of MA ions in the structure. The BA ion interacts strongly with the Pb-I lattice for the $n = 1$ structure. When the inorganic layer becomes thicker and MA ions are introduced, this leads to a screening effect with a net repulsive interaction between the MA and BA ions. The overall result of this is an increased rotational freedom for structures with $n > 1$.

3.4 Conclusions

In this chapter we have analyzed the structural dynamics of Ruddlesden-Popper perovskites using model potential molecular dynamics simulations. Calculations were performed for different thicknesses of the inorganic layer. The results show that the dimensionality (layer thickness) of 2D Ruddlesden-Popper perovskites has a clear, but not always a straightforward, effect on the structure and dynamics of both the inorganic and organic part of the perovskite. In case of the inorganic part, we see that the rigidity increases as the number of inorganic layers is increased and that the $n = 1$ structure is substantially less rigid than the structures with $n > 1$. In addition, we clearly observe phase transition where the tilting of the average Pb-I-Pb angles changes for the $n = 3$ and $n = \infty$ structures, but in the other structures this is not as clearly visible.

In the organic part certain orientations of MA ions are not as favorable in the case of the 2D perovskite when compared to its 3D counterpart. This clearly shows the effect of the edges of the perovskite structure where relatively static BA cations are present. This non-uniform surrounding leads to restricted rotational freedom of the MA cations in the 2D structures, as compared to the 3D material. The motion of the organic cations is also directly linked to deformations in the inorganic lattice and clear differences are observed for different thicknesses of the inorganic layer. The results presented highlight the interplay between the inorganic and organic part in these materials, which is complex and not necessarily uniform for all the different structures. An improved understanding of the structural dynamics is essential for systematically engineering the electronic properties of Ruddlesden-Popper perovskites as the electronic structure is directly linked to the structure of the inorganic lattice and the rotational dynamics of the dipolar organic cations.

References

1. Kojima, A.; Teshima, K.; Shirai, Y.; Miyasaka, T., Organometal Halide Perovskites as Visible-Light Sensitizers for Photovoltaic Cells. *J. Am. Chem. Soc.* 2009, 131 (17), 6050-6051.
2. Lee, M. M.; Teuscher, J.; Miyasaka, T.; Murakami, T. N.; Snaith, H. J., Efficient Hybrid Solar Cells Based on Meso-Superstructured Organometal Halide Perovskites. *Science* 2012, 338 (6107), 643-647.
3. Snaith, H. J., Present Status and Future Prospects of Perovskite Photovoltaics. *Nat. Mater.* 2018, 17 (5), 372-376.
4. National Renewable Energy Laboratory (NREL) Best Research- Cell Efficiencies Chart. <https://www.nrel.gov/pv/cell-efficiency.html> (accessed 2020-06).
5. Tan, Z.-K.; Moghaddam, R. S.; Lai, M. L.; Docampo, P.; Higler, R.; Deschler, F.; Price, M.; Sadhanala, A.; Pazos, L. M.; Credgington, D., et al., Bright Light-Emitting Diodes based on Organometal Halide Perovskite. *Nat. Nanotechnol.* 2014, 9 (9), 687-692.
6. Veldhuis, S. A.; Boix, P. P.; Yantara, N.; Li, M.; Sum, T. C.; Mathews, N.; Mhaisalkar, S. G., Perovskite Materials for Light-Emitting Diodes and Lasers. *Adv. Mater.* 2016, 28 (32), 6804-34.
7. Xu, W.; Hu, Q.; Bai, S.; Bao, C.; Miao, Y.; Yuan, Z.; Borzda, T.; Barker, A. J.; Tyukalova, E.; Hu, Z., et al., Rational Molecular Passivation for High-Performance Perovskite Light-Emitting Diodes. *Nat. Photonics.* 2019, 13 (6), 418-424.
8. Dou, L.; Yang, Y.; You, J.; Hong, Z.; Chang, W.-H.; Li, G.; Yang, Y., Solution-Processed Hybrid Perovskite Photodetectors with High Detectivity. *Nat. Commun.* 2014, 5 (1), 5404.
9. Leung, S. F.; Ho, K. T.; Kung, P. K.; Hsiao, V. K. S.; Alshareef, H. N.; Wang, Z. L.; He, J. H., A Self-Powered and Flexible Organometallic Halide Perovskite Photodetector with Very High Detectivity. *Adv. Mater.* 2018, 30 (8).
10. Chen, S.; Roh, K.; Lee, J.; Chong, W. K.; Lu, Y.; Mathews, N.; Sum, T. C.; Nurmikko, A., A Photonic Crystal Laser from Solution Based Organo-Lead Iodide Perovskite Thin Films. *ACS Nano* 2016, 10 (4), 3959-67.
11. Stoumpos, C. C.; Malliakas, C. D.; Peters, J. A.; Liu, Z.; Sebastian, M.; Im, J.; Chasapis, T. C.; Wibowo, A. C.; Chung, D. Y.; Freeman, A. J., et al., Crystal Growth of the Perovskite Semiconductor CsPbBr₃: A New Material for High-Energy Radiation Detection. *Cryst. Growth Des.* 2013, 13 (7), 2722-2727.
12. Wei, H.; Fang, Y.; Mulligan, P.; Chuirazzi, W.; Fang, H.-H.; Wang, C.; Ecker, B. R.; Gao, Y.; Loi, M. A.; Cao, L., et al., Sensitive X-Ray Detectors made of Methylammonium Lead Tribromide Perovskite Single Crystals. *Nat. Photonics.* 2016, 10 (5), 333-339.
13. Wei, H.; Huang, J., Halide Lead Perovskites for Ionizing Radiation Detection. *Nat. Commun.* 2019, 10 (1), 1066.
14. Berhe, T. A.; Su, W.-N.; Chen, C.-H.; Pan, C.-J.; Cheng, J.-H.; Chen, H.-M.; Tsai, M.-C.; Chen, L.-Y.; Dubale, A. A.; Hwang, B.-J., Organometal Halide Perovskite Solar Cells: Degradation and Stability. *Energy Environ. Sci.* 2016, 9 (2), 323-356.
15. Niu, G.; Guo, X.; Wang, L., Review of Recent Progress in Chemical Stability of Perovskite Solar Cells. *J. Mater. Chem. A* 2015, 3 (17), 8970-8980.
16. Mitzi, D. B., Synthesis, Crystal Structure, and Optical and Thermal Properties of

- (C₄H₉NH₃)₂MI₄ (M = Ge, Sn, Pb). *Chem. Mater.* 1996, 8 (3), 791-800.
17. Smith, I. C.; Hoke, E. T.; Solis-Ibarra, D.; McGehee, M. D.; Karunadasa, H. I., A Layered Hybrid Perovskite Solar-Cell Absorber with Enhanced Moisture Stability. *Angew. Chem. Int. Ed.* 2014, 53 (42), 11232-5.
 18. Cao, D. H.; Stoumpos, C. C.; Farha, O. K.; Hupp, J. T.; Kanatzidis, M. G., 2D Homologous Perovskites as Light-Absorbing Materials for Solar Cell Applications. *J. Am. Chem. Soc.* 2015, 137 (24), 7843-50.
 19. Dou, L.; Wong, A. B.; Yu, Y.; Lai, M.; Kornienko, N.; Eaton, S. W.; Fu, A.; Bischak, C. G.; Ma, J.; Ding, T., et al., Atomically Thin Two-Dimensional Organic-Inorganic Hybrid Perovskites. *Science* 2015, 349 (6255), 1518-21.
 20. Liu, J.; Xue, Y.; Wang, Z.; Xu, Z.-Q.; Zheng, C.; Weber, B.; Song, J.; Wang, Y.; Lu, Y.; Zhang, Y., et al., Two-Dimensional CH₃NH₃PbI₃ Perovskite: Synthesis and Optoelectronic Application. *ACS Nano* 2016, 10 (3), 3536-3542.
 21. Stoumpos, C. C.; Cao, D. H.; Clark, D. J.; Young, J.; Rondinelli, J. M.; Jang, J. I.; Hupp, J. T.; Kanatzidis, M. G., Ruddlesden-Popper Hybrid Lead Iodide Perovskite 2D Homologous Semiconductors. *Chem. Mater.* 2016, 28 (8), 2852-2867.
 22. Liao, Y.; Liu, H.; Zhou, W.; Yang, D.; Shang, Y.; Shi, Z.; Li, B.; Jiang, X.; Zhang, L.; Quan, L. N., et al., Highly Oriented Low-Dimensional Tin Halide Perovskites with Enhanced Stability and Photovoltaic Performance. *J. Am. Chem. Soc.* 2017, 139 (19), 6693-6699.
 23. Spanopoulos, I.; Hadar, I.; Ke, W.; Tu, Q.; Chen, M.; Tsai, H.; He, Y.; Shekhawat, G.; Dravid, V. P.; Wasielewski, M. R., et al., Uniaxial Expansion of the 2D Ruddlesden-Popper Perovskite Family for Improved Environmental Stability. *J. Am. Chem. Soc.* 2019, 141 (13), 5518-5534.
 24. Quan, L. N.; Yuan, M.; Comin, R.; Voznyy, O.; Beauregard, E. M.; Hoogland, S.; Buin, A.; Kirmani, A. R.; Zhao, K.; Amassian, A., et al., Ligand-Stabilized Reduced-Dimensionality Perovskites. *J. Am. Chem. Soc.* 2016, 138 (8), 2649-55.
 25. Yuan, M.; Quan, L. N.; Comin, R.; Walters, G.; Sabatini, R.; Voznyy, O.; Hoogland, S.; Zhao, Y.; Beauregard, E. M.; Kanjanaboos, P., et al., Perovskite Energy Funnels for Efficient Light-Emitting Diodes. *Nat. Nanotechnol.* 2016, 11 (10), 872-877.
 26. Gao, Y.; Shi, E.; Deng, S.; Shiring, S. B.; Snider, J. M.; Liang, C.; Yuan, B.; Song, R.; Janke, S. M.; Liebman-Peláez, A., et al., Molecular Engineering of Organic-Inorganic Hybrid Perovskites Quantum Wells. *Nat. Chem.* 2019, 11 (12), 1151-1157.
 27. Passarelli, J. V.; Fairfield, D. J.; Sather, N. A.; Hendricks, M. P.; Sai, H.; Stern, C. L.; Stupp, S. I., Enhanced Out-of-Plane Conductivity and Photovoltaic Performance in n = 1 Layered Perovskites through Organic Cation Design. *J. Am. Chem. Soc.* 2018, 140 (23), 7313-7323.
 28. Du, K.-z.; Tu, Q.; Zhang, X.; Han, Q.; Liu, J.; Zauscher, S.; Mitzi, D. B., Two-Dimensional Lead(II) Halide-Based Hybrid Perovskites Templated by Acene Alkylamines: Crystal Structures, Optical Properties, and Piezoelectricity. *Inorg. Chem.* 2017, 56 (15), 9291-9302.
 29. Gélvez-Rueda, M. C.; Fridriksson, M. B.; Dubey, R. K.; Jager, W. F.; van der Stam, W.; Grozema, F. C., Overcoming the Exciton Binding Energy in Two-Dimensional Perovskite Nanoplatelets by Attachment of Conjugated Organic Chromophores. *Nat. Commun.* 2020, 11 (1), 1901.

30. Maheshwari, S.; Savenije, T. J.; Renaud, N.; Grozema, F. C., Computational Design of Two-Dimensional Perovskites with Functional Organic Cations. *J. Phys. Chem. C* 2018, 122 (30), 17118-17122.
31. Zibouche, N.; Islam, M. S., Structure-Electronic Property Relationships of 2D Ruddlesden-Popper Tin- and Lead-based Iodide Perovskites. *ACS Appl. Mater. Interfaces* 2020, 12 (13), 15328-15337.
32. Seitz, M.; Magdaleno, A. J.; Alcazar-Cano, N.; Melendez, M.; Lubbers, T. J.; Walraven, S. W.; Pakdel, S.; Prada, E.; Delgado-Buscalioni, R.; Prins, F., Exciton Diffusion in Two-Dimensional Metal-Halide Perovskites. *Nat. Commun.* 2020, 11 (1), 2035.
33. Deng, S.; Shi, E.; Yuan, L.; Jin, L.; Dou, L.; Huang, L., Long-Range Exciton Transport and Slow Annihilation in Two-Dimensional Hybrid Perovskites. *Nat. Commun.* 2020, 11 (1), 664.
34. Maheshwari, S.; Patwardhan, S.; Schatz, G. C.; Renaud, N.; Grozema, F. C., The Effect of the Magnitude and Direction of the Dipoles of Organic Cations on the Electronic Structure of Hybrid Halide Perovskites. *Phys. Chem. Chem. Phys.* 2019, 21 (30), 16564-16572.
35. Gallop, N. P.; Selig, O.; Giubertoni, G.; Bakker, H. J.; Rezus, Y. L. A.; Frost, J. M.; Jansen, T. L. C.; Lovrincic, R.; Bakulin, A. A., Rotational Cation Dynamics in Metal Halide Perovskites: Effect on Phonons and Material Properties. *J. Phys. Chem. Lett.* 2018, 9 (20), 5987-5997.
36. Mao, L.; Stoumpos, C. C.; Kanatzidis, M. G., Two-Dimensional Hybrid Halide Perovskites: Principles and Promises. *J. Am. Chem. Soc.* 2019, 141 (3), 1171-1190.
37. Plimpton, S., Fast Parallel Algorithms for Short-Range Molecular Dynamics. *J. Comput. Phys.* 1995, 117 (1), 1-19.
38. Mattoni, A.; Filippetti, A.; Saba, M. I.; Delugas, P., Methylammonium Rotational Dynamics in Lead Halide Perovskite by Classical Molecular Dynamics: The Role of Temperature. *J. Phys. Chem. C* 2015, 119 (30), 17421-17428.
39. Ponder, J. W.; Case, D. A., Force Fields for Protein Simulations. *Adv. Protein Chem.* 2003, 66, 27-85.
40. Maheshwari, S.; Fridriksson, M. B.; Seal, S.; Meyer, J.; Grozema, F. C., The Relation between Rotational Dynamics of the Organic Cation and Phase Transitions in Hybrid Halide Perovskites. *J. Phys. Chem. C* 2019, 123 (23), 14652-14661.
41. Breneman, C. M.; Wiberg, K. B., Determining Atom-Centered Monopoles from Molecular Electrostatic Potentials. The Need for High Sampling Density in Formamide Conformational Analysis. *J. Comput. Chem.* 1990, 11 (3), 361-373.
42. Frisch, M. J.; Trucks, G. W.; Schlegel, H. B.; Scuseria, G. E.; Robb, M. A.; Cheeseman, J. R.; Scalmani, G.; Barone, V.; Petersson, G. A.; Nakatsuji, H., et al. *Gaussian 09 Rev. A.02*, Wallingford, CT, 2016.
43. Stoumpos, C. C.; Malliakas, C. D.; Kanatzidis, M. G., Semiconducting Tin and Lead Iodide Perovskites with Organic Cations: Phase Transitions, High Mobilities, and Near-Infrared Photoluminescent Properties. *Inorg. Chem.* 2013, 52 (15), 9019-9038.

Appendix

Molecular dynamics parameters

The force field employed is based on the work of Mattoni et al.³⁸ and uses both Buckingham potential and Lennard-Jones potential to describe the interatomic interactions. The Buckingham potential (Equation A3.1) is used for inorganic-inorganic interactions as well as interaction between the inorganics and either a carbon or a nitrogen. All other interatomic interactions are described by the Lennard-Jones potential (Equation A3.2). The Buckingham potential parameters are obtained from Mattoni et al.³⁸ and can be seen in table A3.1. The Lennard-Jones parameters are obtained either from Mattoni et al.³⁸ or from the standard Amber force field³⁹ and can be seen in table A3.2.

The intramolecular terms are obtained from the standard Amber force field.³⁹ The bonds and angles are described by the harmonic approximation (Equations A3.3 and A3.4) and the parameters can be found in tables A3.3 and A3.4 respectively. For the dihedrals the fourier approximation (Equation A3.5) is used and the parameters can be found in table A3.5.

In this work we use full formal charges to the individual molecules. The partial charges on the individual atoms in MA and BA were obtained by fitting them to the electrostatic potential from a density functional theory calculation (B3LYP/cc-pVQZ) using the CHelpG approach⁴¹ in the Gaussian09 software.⁴² The individual charges on each atom in the simulation can be seen in table A3.6. The organic atoms are distinguished between methylammonium and butylammonium with brackets containing either MA or BA. The different carbons in the butylammonium are distinguished with numbers ranging from 1 to 4, where C₁ is the carbon next to the nitrogen and C₄ is the carbon on the other end of the molecule.

$$E = Ae^{-r/\rho} - \frac{C}{r^6} \quad \text{A3.1}$$

Table A3.1 Buckingham potential coefficients for each atom pair.

Pairs	A (Kcal/mole)	ρ (Å)	C (Å·Kcal/mole)
Pb – Pb	70359906.62970	0.131258	0.00
Pb – I	103496.13301	0.321737	0.00
I – I	22793.33858	0.482217	696.94954
Pb – N	32690390.93800	0.150947	0.00
Pb – C	32690390.93800	0.150947	0.00
I – N	112936.71421	0.342426	0.00
I – C	112936.71421	0.342426	0.00

$$E = 4\epsilon \left[\left(\frac{\sigma}{r} \right)^{12} - \left(\frac{\sigma}{r} \right)^6 \right] \quad \text{A3.2}$$

Table A3.2 Lennard-Jones potential coefficients for each atom pair.

Pairs	ϵ (Kcal/mole)	σ (Å)	Pairs	ϵ (Kcal/mole)	σ (Å)
Pb – H _s	0.01400	2.26454	N – H _c	0.0517	2.60500
Pb – H _c	0.01400	2.70999	C – C	0.10940	3.39970
I – H _s	0.0574	2.75000	C – H _s	0.04140	2.23440
I – H _c	0.0574	3.10000	C – H _c	0.04140	2.67980
N – N	0.17000	3.25000	H _s – H _s	0.01570	1.06910
N – C	0.13640	3.32480	H _s – H _c	0.01570	1.51450
N – H _s	0.0517	2.15950	H _c – H _c	0.01570	1.96000

$$E = K(r - r_0)^2 \quad \text{A3.3}$$

Table A3.3 Bond coefficients.

Bond	K (Kcal/mole/ Å ²)	r ₀ (Å)
N – C	276.638	1.480
N – H _s	443.528	1.028
C – C	306.432	1.508
C – H _c	342.991	1.093

$$E = K(\theta - \theta_0)^2 \quad \text{A3.4}$$

Table A3.4 Angle coefficients.

Angles	K (Kcal/mole/rad ²)	θ_0 (°)
H _s – N – H _s	41.596	107.787
H _s – N – C	41.452	111.206
N – C – C	84.848	106.493
N – C – H _c	62.754	106.224
H _c – C – H _c	37.134	108.836
C – C – H _c	54.770	110.549
C – C – C	61.243	109.608

$$E = \sum_i K_i [1.0 + \cos(n_i \phi - d_i)]$$

A3.5

Table A3.5 Dihedral coefficients.

Dihedrals	i	K (Kcal/mole)	n	d (°)
H _s – N – C – H _c	1	0.13	3	0
H _s – N – C – C	1	0.093	3	0
N – C – C – H _c	1	0.346	1	0
	2	-0.265	2	180
	3	0.139	3	0
N – C – C – C	1	-0.324	1	0
	2	0.275	2	180
	3	0.295	3	0
H _c – C – C – H _c	1	0.142	1	0
	2	-0.693	2	180
	3	0.157	3	0
H _c – C – C – C	1	0.32	1	0
	2	-0.315	2	180
	3	0.132	3	0
C – C – C – C	1	0.051	1	0
	2	0.341	2	180
	3	0.166	3	0

Table A3.6 Charges of atoms.

Atom	Charge	Atom	Charge
Pb	2.0000	C1 (BA)	0.0955
I	-1.0000	H _{ca} (BA)	0.0794
N (MA)	-0.3301	C2 (BA)	-0.1045
H _s (MA)	0.3328	H _{ca} (BA)	0.0534
C (MA)	-0.0523	C3 (BA)	0.1411
H _c (MA)	0.1280	H _{ca} (BA)	-0.0037
N (BA)	-0.4157	C4 (BA)	-0.1659
H _s (BA)	0.3366	H _{ca} (BA)	0.0605

The effect of using full formal charges

Using full formal charges is a different approach than Mattoni et al.³⁸ used. We do this in order to have a transferrable force field where the parameters can be assigned independent of the layer thickness of the inorganic layer and the nature of the large organic cation. This however does affect absolute results of individual structures. Figure A3.1 show the rotational autocorrelation of 3D perovskite with full atomic charges and if the charges are kept constant with the work of Mattoni et al.³⁸ that figure is obtained from our previous work on 3D perovskite.⁴⁰ As can be seen there is a substantial effect as the phase transition occurs at roughly 50 K instead of occurring around 200 K. However, crucially the phase transition is still visible.

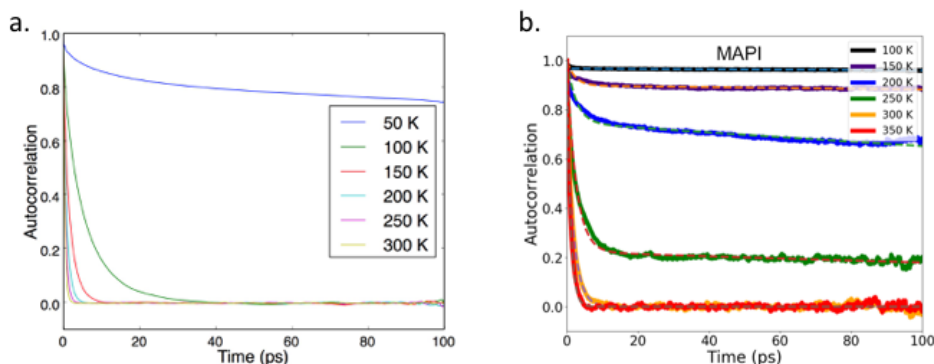


Figure A3.1 Rotational autocorrelation function of 3D methylammonium lead iodide using (a) full formal charges and (b) using the charges from the original force field.⁴⁰

Out-of-layer iodide angle

Since the $n = 1$ structure has no Pb-I-Pb angle in the direction perpendicular to the lead-iodide layer we cannot compare the tilting of the octahedra in that structure to the other materials using that angle. Because of that we define here the out-of-layer iodide angle. The out-of-layer iodide angle is the angle between the lead-iodide plane and the vector between the two iodides in the octahedra that are out of the lead-iodide plane, as indicated in Figure A3.2a. As this is an angle between a vector and a plane it will maximum be 90° if the vector between the iodides is perpendicular to the plane, as would be the case for a perfectly cubic structure. However, due to motion of the atoms, even a cubic structure will have a slightly lower average out-of-layer iodide angle than 90° . If no structural changes occur in the material when the temperature is lowered, one would expect the standard deviation of the angles to decrease and the average angle to approach 90° , due to fewer outliers. Figure A3.2b shows the standard deviation of the out-of-layer iodide angles versus temperature, and Figure A3.2c shows the average out-of-layer iodide angles for the different structures versus temperature.

The first observation is that there is a clear trend where, as the number of lead-iodide layers is increased, the average angle approaches 90° and the standard deviation decreases. Similar to what we saw for the Pb-I-Pb angles (Figure 3.2). This indicates that the $n = 1$ structure has the largest tilting of the octahedra in this direction as well as in the in-layer directions. The behavior of the 3D perovskite and the $n = 3$ structure is very similar to what we saw in Figure 3.2b where at lower temperature the angle gets smaller indicating more tilted octahedra. The $n = 2$ structure has a different behavior for the out-of-layer iodide angle than would have been expected from its Pb-I-Pb angle. The Pb-I-Pb angle increased steadily as the temperature was decreased, which is not the case for the out-of-layer iodide angle. This indicates that even though the Pb-I-Pb angle between the octahedra gets more rigid at lower temperature there is still some freedom in the iodides that are not flanked between the octahedra.

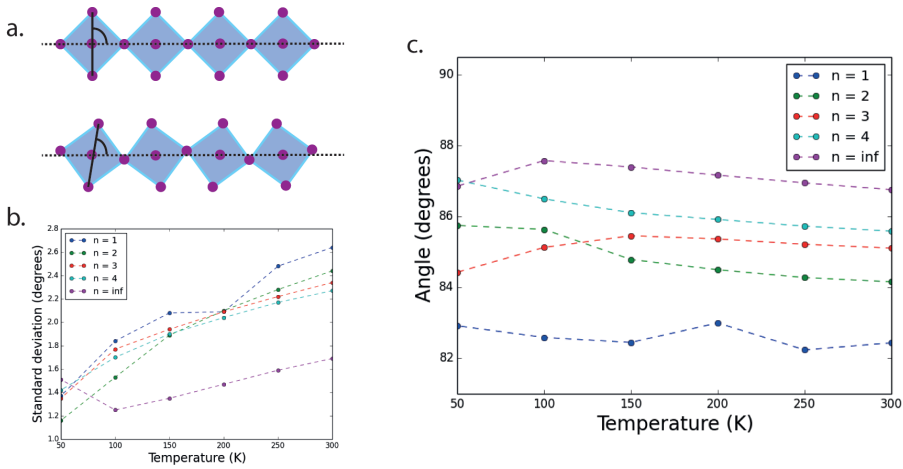


Figure A3.2 Out-of-layer iodide angles. (a) A schematic showing what we define here as the out-of-layer iodide angle. (b) The standard deviation of the out-of-layer iodide angles versus temperature for all the structures. (c) The average out-of-layer iodide angle versus temperature for all the structures.

Comparison of the two Pb-I-Pb angles within the lead-iodide layer

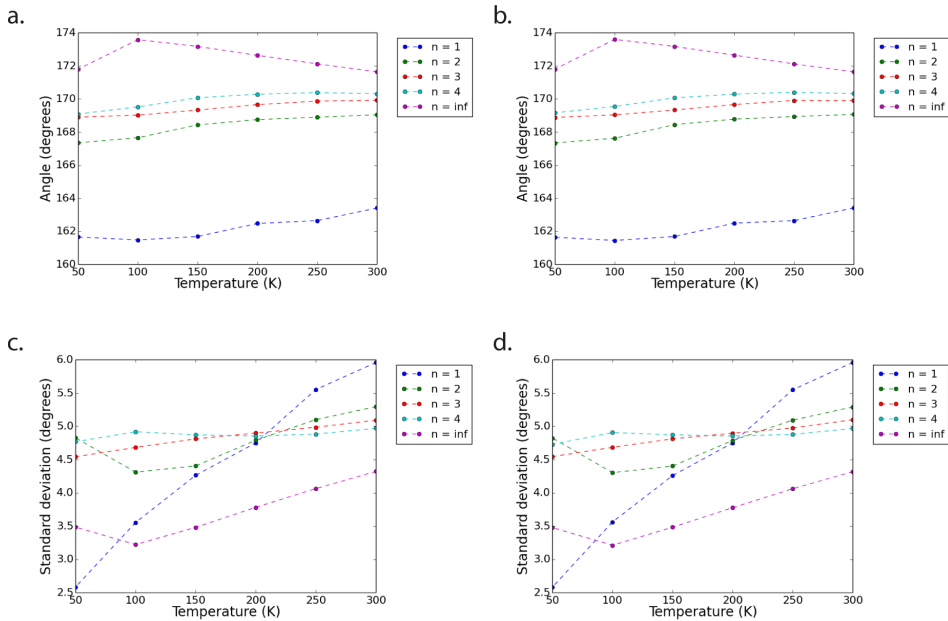


Figure A3.3 Comparison of the two different Pb-I-Pb angles in the lead-iodide layers. (a) Average Pb-I-Pb angles in x-direction in the lead-iodide layer. (b) Average Pb-I-Pb angles in y-direction in the lead-iodide layer. (c) Standard deviation of the Pb-I-Pb angles in the x-direction in the lead-iodide layer. (d) Standard deviation of the Pb-I-Pb angles in the y-direction in the lead-iodide layer.

4



Tuning the Structural Rigidity of 2D Ruddlesden-Popper Perovskites Through the Organic Cation

Two-dimensional (2D) hybrid organic-inorganic perovskites are an interesting class of semi-conducting materials. One of their main advantages is the large freedom in the nature of the organic spacer molecules that separates the individual inorganic layers. The nature of the organic layer can significantly affect the structure and dynamics of the 2D material, however, there is currently no clear understanding of the effect of the organic component on the structural parameters. In this chapter we have used molecular dynamics simulations to investigate the structure and dynamics of 2D Ruddlesden-Popper perovskite with a single inorganic layer ($n = 1$) and varying organic cations. We discuss the dynamic behavior of both the inorganic and the organic part of the materials as well as the interplay between the two, and compare the different materials. We show that both aromaticity as well as the length of the flexible linker between the aromatic unit and the amide has a clear effect on the dynamics of both the organic and the inorganic part of the structures, highlighting the importance of the organic cation in the design of 2D perovskites.

4.1 Introduction

In recent years two-dimensional (2D) Ruddlesden-Popper hybrid halide perovskite materials have attracted interest as opto-electronic materials,¹⁻³ in particular as a more stable alternative for their three-dimensional (3D) counterparts.⁴⁻⁵ The use of 2D perovskites has already been demonstrated in light emitting diodes (LED)⁶⁻⁷, lasers⁸⁻⁹ and solar cell devices¹⁰⁻¹² with good results. The general structure of 2D Ruddlesden-Popper perovskites is $(\text{R-NH}_3)_2\text{A}_{n-1}\text{B}_n\text{X}_{3n+1}$,¹³⁻¹⁴ where B and X are a metal cation and a halide, respectively; A is a small (organic) cation incorporated in the cavities of the metal halide lattice and R is a larger organic amide which is responsible for breaking the perovskite structure into 2D layers.

4

One of the main advantages of the 2D Ruddlesden-Popper perovskites compared to 3D perovskites is the added design freedom introduced by the large organic cation. As is the case with 3D perovskites, it is possible to vary the A, B and X ions, which affects the electronic properties of the material.^{3, 15-16} However, for 2D perovskites there is an added freedom in choosing the large organic cation (R-NH_3) where specific functional organic moieties can be introduced. In addition, the number of inorganic layers (n) in the structure can be varied by changing the ratio between the small (A) and large organic cations. Altering these variables affects several properties of the material. For instance, the number of inorganic layers has been shown to affect the bandgap,¹⁷ as well as both the exciton binding energy¹⁸ and the exciton diffusion length.¹⁹ Additionally, changes in the structure of the large organic cation have been shown to affect the dielectric environment,²⁰⁻²¹ electron-phonon coupling,²² the stability of the perovskite towards air and moisture,²³ and the exciton diffusion length.²⁴

Currently, the most common large organic cations for 2D Ruddlesden-Popper perovskites are n-butylammonium (BA)^{13, 17, 25} and phenylethylammonium (PEA).^{6, 26-27} They differ in the sense that PEA contains an aromatic phenyl group that can aid the packing of the organic molecules through π - π interactions. 2D perovskites with a variety of larger organic cations have also been made, including longer aliphatic chains such as hexyl- and octylammonium²⁸⁻³⁰ and large conjugated molecules.^{23, 31-33} These larger conjugated molecules exhibit even stronger π - π interactions than PEA and have been shown to result in exceptional moisture-stability.²³

The effects of changes in the organic component are known to be very subtle, and depending on the nature of the organic component and the processing conditions, often lower-dimensional structures are formed.³⁴⁻³⁵ In addition, the interaction between the organic moieties in the side chains can have a distinct effect on the structure and dynamics of the inorganic layers in the material, and in this way can indirectly affect the opto-electronic properties of the material. A detailed understanding of the interplay between the interactions in the layer of large organic cations and the inorganic layer is essential in the design of new 2D perovskite materials. However, at present, the understanding of these interactions is currently very limited, especially since theoretical studies of the structural dynamics are largely limited to BA, PEA and some small organic cations. It is especially interesting to consider the effect of the aromaticity and the length of an aliphatic chain on the structure and dynamics of the inorganic layer. A large aromatic

core will have stronger π - π interactions resulting in the molecules packing closer together and moving less which could influence the motion of the inorganic layer and make it more rigid. However, the length of the aliphatic chain could also play a role as a longer chain can result in more movement independent of the aromaticity.

In this chapter we have performed classical molecular dynamics (MD) simulations on $n = 1$ Ruddlesden-Popper perovskites with lead-iodide inorganic layer and three different organic cations varying in the presence and size of the aromatic component and in the length of the aliphatic chain connected to the amide. The organic cations considered are BA, PEA and pyrene-*o*-butylammonium (POB). We then compare the dynamics of the organic molecules, the dynamics and structure of the inorganic lead-iodide layer and discuss the interplay between these two parts. We show that both the aromaticity as well as the length of the aliphatic chain has a substantial effect on the structure and dynamics of both the organic and the inorganic part of the system, highlighting the impact the organic cations can have on the properties of 2D perovskites.

4.2 Methods

The MD simulations are performed using the LAMMPS software.³⁶ A time step of 1 fs is used for all the simulations and all the simulations start at 300 K, where the system is equilibrated for 1 ns. Thereafter the temperature is decreased to the desired temperature with a fixed annealing rate of 125 K/ns. When the desired temperature is reached the system is again allowed to equilibrate for 1 ns before a 100 ps production run is performed. Throughout the production run the positions of all the atoms is recorded.

The force field used in the MD simulations is based on the MYP force field³⁷ and on our previous work on 3D perovskites³⁸ and 2D Ruddlesden-Popper perovskites with varying number of inorganic layers with BA as the large organic cation and. The intermolecular potential for the lead and the iodide is taken from the MYP force field³⁷ and consists of a Buckingham potential except for the interaction between either lead or iodide with hydrogen where a Lennard-Jones potential is used. Both the inter- and intramolecular parameters for BA are the same as in the previous chapter, while the additional parameters for PEA and POB are obtained from the standard Amber force field,³⁹ consistent with the MYP force field. All intermolecular interactions between two organic molecules are described by a Lennard-Jones potential. In order to make the force field transferable between the different materials that we consider, we deviate from the MYP force field in one respect: the partial charges for the Coulomb interactions. We assign the full formal charges +2 and -1 to the lead and iodide ions (versus +2.02 and -1.13 in the MYP force field). In addition, the organic cations have a full +1 charge that is distributed over all atoms as obtained from an electronic structure calculation. The partial charges on the individual atoms in the organic molecules were obtained by fitting them to the electrostatic potential from a density functional theory calculation (B3LYP/cc-pVTZ) using the CHelpG approach⁴⁰ in the Gaussian09 software.⁴¹

The initial structures were obtained from the experimental crystal structures of the materials.^{14, 31, 42} The simulations are performed on a supercell of 10×10 unit cells where the direction perpendicular to the inorganic lead-iodide layer is not replicated. Due to the

size of the unit cells each simulation includes two lead-iodide layers. Periodic boundary conditions are used in all directions and NPT ensemble is used.

4.3 Results and discussion

In order to analyze how the intermolecular interactions in the organic part of the material affect the dynamics in 2D Ruddlesden-Popper perovskites we analyze the MD trajectories of the materials at different temperatures. The analysis is separated into three parts. We first discuss the dynamics of the organic part, after which we consider the structure and dynamics of the inorganic layer. Finally, we examine the interaction between the organic molecules and the inorganic layer.

4.3.1 Dynamics of the organic molecules

In Figure 4.1 the three large organic cations considered in this work are shown. As can be seen, the molecular structures vary considerably, leading to differences in the interaction. The structural differences make it also challenging to compare their dynamics. A common structural element in all compounds is the amide group that coordinates with the inorganic layer. An obvious way to monitor the motion of this linking amide group is to compare the rotational dynamics of the C-N bond in the amide group in the different molecules. This is achieved by comparing the rotational autocorrelation function (ACF) of the C-N bond for the different materials. The rotational autocorrelation function is calculated according to the following equation (4.1) where N_{ion} is the number of organic cations, N_{t_0} is the number of initial times (t_0) considered and \hat{n} is the unit vector in the direction of the bond.

$$A(t) = \langle \hat{n}(t) \cdot \hat{n}(0) \rangle = \frac{1}{N_{ion}} \sum_i \frac{1}{N_{t_0}} \sum_{t_1=t+t_0} \hat{n}_i(t_1) \cdot \hat{n}_i(t_0) \quad 4.1$$

The ACF gives an indication of the extent of the rotational motion of the bond and of

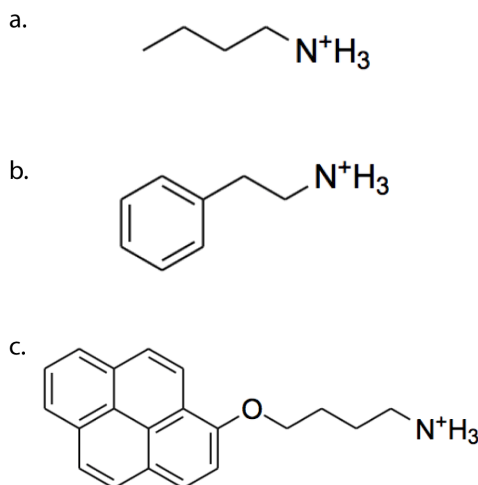


Figure 4.1 The large organic cations present in the examined structures. (a) n-butylammonium (BA). (b) phenylethylammonium (PEA). (c) pyrene-o-butylammonium (POB).

the time scale on which this motion occurs. Initially, the ACF is always equal to 1, but as a function of time it will decay as the average direction of the bond will start to deviate from the initial direction. For a freely rotating bond the ACF will decay to zero eventually, indicating a random orientation on average. If the rotational motion is restricted, the ACF does not decay all the way to zero but a plateau may be reached after some time. Such restricted motion is found in the rotational dynamics in the present case since the coordination of the amide group to the inorganic layer prevents full reorientation of the C-N bond. Therefore, a plateau value is reached after some time. Higher plateau values indicate a more restricted rotational motion of the bond compared to lower ones. The time required to reach the plateau indicates the time scale on which the rotational motion takes place and can be defined as a rotational diffusion time. In Figure 4.2 the ACF of the C-N bond is shown for the three compounds at all simulated temperatures.

From Figure 4.2a we see that at high temperatures (300 K) the ACF reaches a plateau with a significantly higher value for PEA than for the other two molecules, indicating a more restricted rotational freedom for the C-N bond. This indicates a more rigid structure that is likely to be related to the combination of π - π interactions and the short relatively rigid ethyl linker. The BA and POB seem to reach a similar value after 100 ps, although for POB no plateau is reached within the 100 ps simulation time. It is obvious that the rotational diffusion of the C-N bond in BA is considerably faster than in BOP as its ACF decays rapidly within the first 10 ps, after which it stays constant. This difference in the time scale of the rotation can be attributed to the large bulky aromatic part of the POB that slows down the rotational movement of the C-N bond in POB.

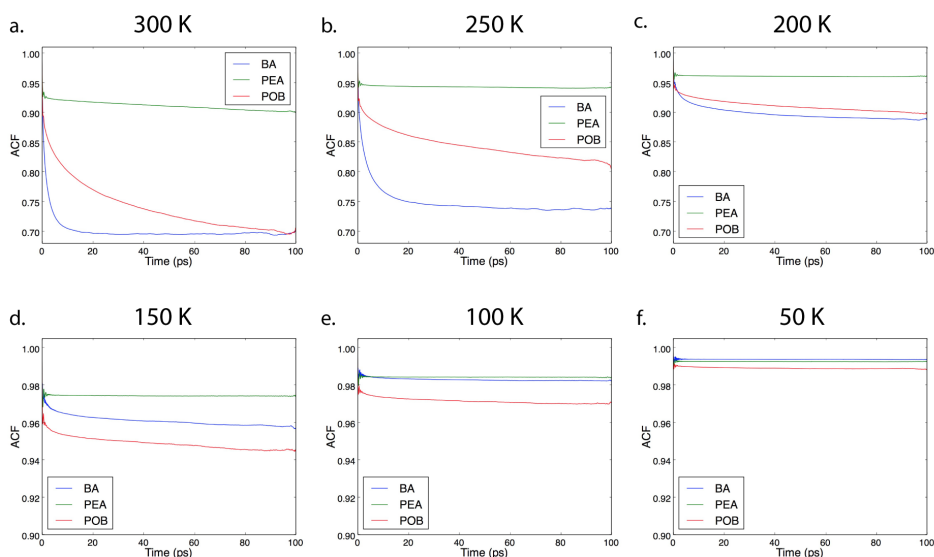


Figure 4.2 Rotational autocorrelation function of the C-N bond in the three organic molecules at different temperatures. (a) 300 K. (b) 250 K. (c) 200 K. (d) 150 K. (e) 100 K. (f) 50 K.

As the temperature is lowered the overall decay in the ACF is less for all compounds, indicating a more rigid structure. For all temperatures the motion of C-N bond in the PEA remains the most restricted. Apart from the simulations at 50 K (Figure 4.2f) where BA has a slightly higher ACF plateau. However, at this temperature the ACF values remain close to 1.0 for both molecules indicating that the bond is more or less fixed in both cases. In the case of the POB, the bond rotation gradually becomes less as the temperature is lowered, as reflected in the higher ACF values. The time scale of the rotation remains slow as can be seen from the lack of plateau formation for POB at all temperatures within the 100 ps simulation time.

For BA the decay of the ACF at 250 K (Figure 4.2b) is similar to the behavior at 300 K apart from a slightly higher plateau value. When the temperature is lowered further to 200 K (Figure 4.2c) a large change in the decay of the ACF is observed, including a slower decay and a considerably higher plateau value. This indicates reduced rotational motion of the C-N bond in the BA which is consistent with the occurrence of a phase transition in the material. This agrees well with the experimentally known phase transition that occurs in this material in the same temperature interval.²⁸ As the temperature is lowered further the ACF plateau value of the BA becomes substantially higher than that for POB and reaches a value similar to PEA.

In order to gain insight in the motion in the other parts of the organic layer we also consider the rotation of bonds further away from the amide group. In Figure 4.3 the rotational ACFs of the aromatic units in PEA and POB (defined by a vector through a phenyl group along the axis of the aromatic part) are compared with the rotation of the terminal C-C bond in BA. Not surprisingly, the terminal C-C bond in BA has substantial rotational freedom at all temperatures, although the motion is strongly restricted at low temperature. In contrast, the π - π interactions in PEA and POB lead to a rigidly packed structure at all temperatures with ACF values very close to 1. Comparison of the ACF for PEA and POB shows that the rotation of the aromatic part of POB is even more restricted than for PEA as a result of the large aromatic unit. Overall, this shows that more rigid tightly packed organic layers are formed when large aromatic units are attached to the amide. The formation of such a tightly packed layer isolates that inorganic part from moisture, explaining the exceptional moisture stability of the POB compounds reported experimentally.³¹ The extent to which

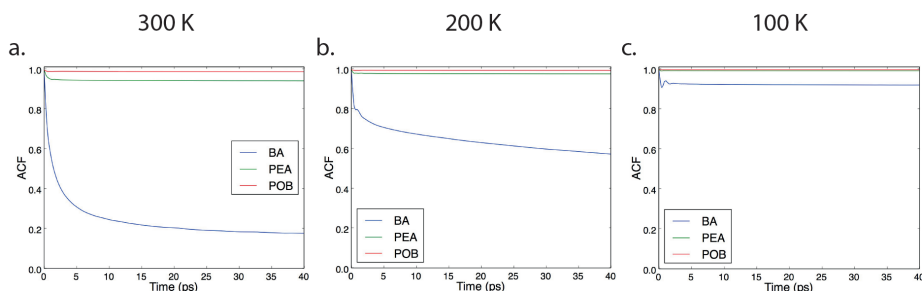


Figure 4.3 Rotational autocorrelation function of the end C-C bond in BA and the vector across a phenyl group in PEA and POB. (a) 300 K. (b) 250 K. (c) 200 K.

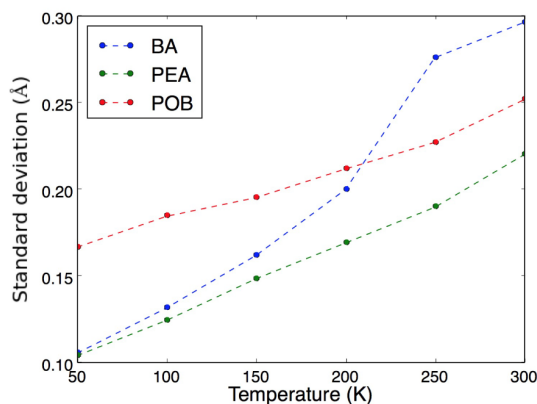


Figure 4.4 Standard deviation of lead atom deviation from the lead plane.

4

the rigidity of the organic layer is transmitted to the amide group that connects with inorganic layer depends strongly on the linker. For the short relatively rigid ethyl linker in PEA this results in severely restricted rotational motion of the C-N bond, while the longer flexible linker in POB allows a rotational freedom comparable to BA.

4.3.2 Structure and dynamics of the inorganic lead-iodide layer

In order to investigate the rigidity of the lead-iodide layer in the different structures we analyze how much the lead atoms deviate from the lead-iodide layer plane throughout the simulation. A detailed description of the procedure followed can be found in the Appendix. The standard deviation of the lead atoms with respect to the lead-iodide layer plane is shown as a function of temperature in Figure 4.4.

From Figure 4.4 it is clear that at all temperatures the lead atoms in the PEA structure deviate the least from the lead-iodide plane. At high temperatures the BA structure exhibits the largest deviation but between 250 K and 200 K it drops drastically. This is the same temperature range as where a sudden jump in the ACF decays for BA was observed, consistent with the claim that this is related to a phase transition in the material. The deviation of the lead atoms in the POB structure decreases gradually as the temperature is lowered similar to PEA. However, the deviation is substantially larger in the case of POB indicating that the lead atoms are less restricted in the lead-iodide plane.

For a more detailed picture of the dynamics of the inorganic lead-iodide layer we have calculated the average absolute distance of a lead atom from its position at a certain reference time (t_0) as a function of time in all directions. This movement is shown in Figure 4.5a and b for 300 K and 50 K, respectively. In Figure 4.5c the mean absolute distance averaged over the time range 10-100ps is plotted as a function of temperature. These curves give an indication of the fluctuations in the position of the Pb atoms, independent on the direction of the movement.

Figure 4.5c shows that the lead atoms in the BA structure have the largest freedom to

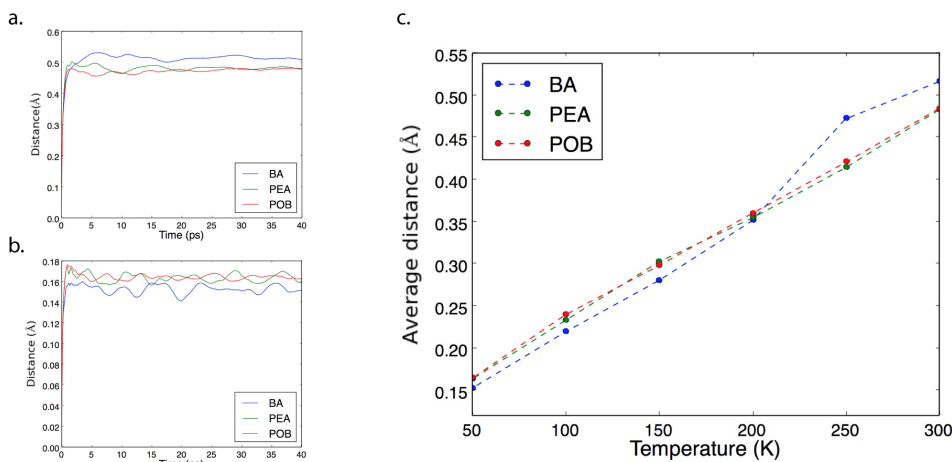


Figure 4.5 (a-b) Average distance of lead atom from its position at $t = 0$ versus time at (a) 300 K and (b) 50 K. (c) Average distance in the range 10-100 ps versus temperature.

move around at high temperatures (250 K and 300 K). But lowering the temperature from 250 K to 200 K results in a sharp decrease in movement. At all temperatures below 200 K the lead atoms in the BA structure have the least freedom to move. This is consistent with the occurrence of a phase transition in the BA material between 250 K and 200 K, resulting in a more rigid structure.

Interestingly the PEA structure and the POB structure show more or less identical mean average movement for the ions at all temperatures. This is in contrast to the observations above for the movement of the Pb ions out of the inorganic plane. A substantially higher out-of-plane movement was found for the POB structure than for the PEA structure. This indicates that the overall movement is similar in both structures, but that in the PEA structure the out-of-plane motion is significantly reduced, as compared to the POB material.

To obtain a more detailed insight in the structural fluctuations in the different 2D perovskite materials we have examined the tilting of the inorganic octahedra in two different directions. Firstly, we examine the Pb-I-Pb angles within each lead-iodide layer. The Pb-I-Pb angle corresponds to the mutual angle between two neighboring octahedra and will therefore give an indication of the tilting of the octahedra in each structure. It is defined in the range $0^\circ - 180^\circ$, where 180° corresponds to a perfectly cubic structure. Increased tilting of the octahedra results in a lower Pb-I-Pb angle. We distinguish between the two different directions of the Pb-I-Pb angles within the layer since these are not necessarily the same. The materials considered in this work all consist of a single inorganic layer flanked between organics ($n = 1$), hence there is no Pb-I-Pb angle in the direction perpendicular to the inorganic layer. To gain insight in the tilting of the octahedra with respect to the inorganic plane we also examine the out-of-layer iodide angle. The out-of-layer iodide angle is the angle between the lead-iodide layer plane and a vector between the two iodides in the octahedral that are above and below the plane. The out-of-layer

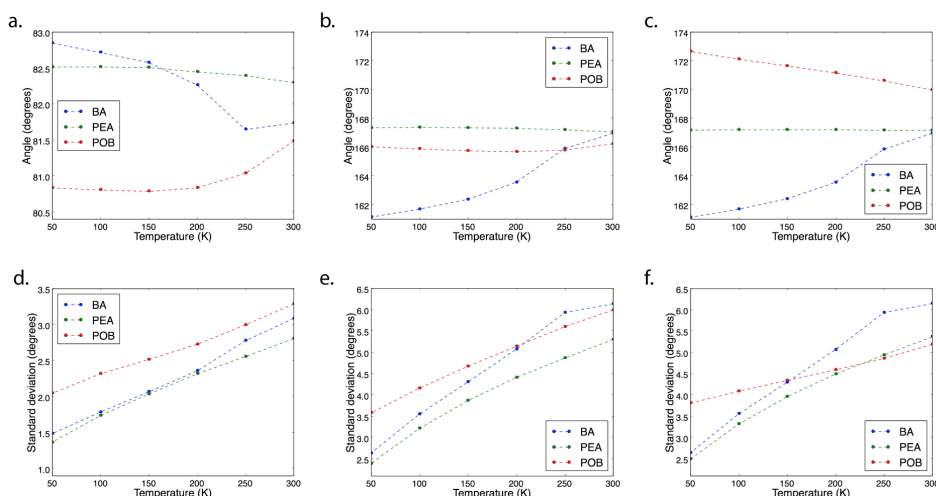


Figure 4.6 The out-of-layer iodide and Pb-I-Pb angles for all structures versus temperature. (a) Average out-of-layer iodide angles. (b) Average Pb-I-Pb angles in x-direction. (c) Average Pb-I-Pb angles in y-direction. (d) Standard deviation of the out-of-layer iodide angles. (e) Standard deviation of the Pb-I-Pb angles in x-direction. (f) Standard deviation of the Pb-I-Pb angles in y-direction.

iodide angle is defined in the range $0^\circ - 90^\circ$. If the structure is perfectly cubic the out-of-layer iodide angle will be 90° but any tilting of the octahedra will result in a smaller angle. In Figure 4.6 the averages and standard deviations of both the out-of-layer iodide angles and the Pb-I-Pb angles are shown.

From Figures 4.6a-c it is clear that the octahedral tilting in the PEA material is virtually unaffected by temperature in all directions, indicating that no significant structural changes take place as the temperature is lowered. In the case of the BA structure structural changes are observed in all three angles as the temperature decreases from 250 K and 200 K. The out-of-layer iodide angle increases indicating less tilting of the octahedra in that direction, while the Pb-I-Pb angles decrease in both x- and y-direction in a similar way, indicating increased tilting of the octahedra in the layer. This change in the octahedral tilting is consistent with our previous notions that we observe a phase transition in the material between these temperatures. The POB structure also exhibits some structural changes but they differ from what was observed for the BA structure. In this case, the out-of-layer iodide angle decreases as the temperature is lowered from 300 K down to 200 K and remains fairly constant below that. It should also be noted that the POB structure has the smallest out-of-layer iodide angle at all temperatures, and therefore the largest octahedral tilt in that particular direction. The Pb-I-Pb angle in x-direction for the POB structure hardly changes with temperature, while the same angle in y-direction increases gradually as the temperature is decreased. The standard deviation of the out-of-layer iodide angles and the Pb-I-Pb angles decreases steadily as the temperature is lowered for all the different structures, as expected.

If we compare the three different structural parameters related to the inorganic lead-iodide

layer considered here, there are some interesting observations. Even though the lead atoms have similar freedom to move in the structures containing PEA and POB, the POB exhibits more movement in the direction perpendicular to the lead-iodide layer. The POB compounds also shows substantially more tilting of the octahedra than the PEA structure in that particular direction. This indicates that is a relation between the tilting of the octahedra in the direction perpendicular to the lead-iodide layer and the rigidity of the same layer. Structures with less tilted octahedra (closer to a cubic structure) result in reduced motion of the lead atoms perpendicular to the inorganic layer.

4.3.3 Interactions between the organic and the inorganic part of the system

4

In preceding two sections we have separately considered the structural dynamics in the organic and the inorganic parts. However, these two parts of the materials are intimately connected. Therefore, we now turn to the interaction between the organic and the inorganic parts. The connection of the two components is formed by the ionic bonding between the amide unit and the Pb-I framework. Some structural insights of this interaction can be derived from the radial distribution function for both lead & nitrogen and iodide & nitrogen, shown in Figures A4.2 and A4.3 at 300 K and 50 K. The lead-nitrogen RDF gives information about the proximity of the amide unit of organic molecules and the lead atoms in the inorganic layers. The amide unit ‘fills’ the cavity formed by the inorganic octahedra and can therefore be interpreted as a penetration depth of the organic molecule into the inorganic layer. The iodide-nitrogen RDF is related to the distance between the amide and the iodide and can be seen as an indication of whether hydrogen bonds are formed between the iodide and the amide hydrogens.

To ease the comparison of the RDFs at different temperatures for the different materials we show in Figure 4.7 the position of the first RDF peak versus temperature for the three materials. This gives an indication of the nearest neighbor distances between lead & nitrogen and iodide & nitrogen. From Figure 4.7a we see that the Pb-N distance is highest for the BA material at all temperatures and we can again see the effect of phase transition occurring in the BA structure as the temperature is lowered from 250 K to 200 K. During this phase transition the lead-nitrogen distance decreases substantially indicating a tighter incorporation of the amide in the cavities in the inorganic structure (or a larger penetration). For the PEA and POB materials no sudden drop in Pb-N distance is observed but they do show a gradual decrease in distance with temperature. It is noteworthy that the PEA structure exhibits a significantly smaller Pb-N distance at all temperatures, but particularly at 300 K. This shows that the average penetration of the amide in PEA is largest.

The iodide-nitrogen distance shown in Figure 4.7b in the PEA structure is more or less stable over all the simulated temperatures, while for the structures including BA and POB there is a steady decrease as the temperature is lowered. This difference can be explained by the difference in aliphatic chain length of the organics. BA and POB both have four carbons in their chain while the PEA only has two. The longer the aliphatic chain, the more freedom the nitrogen has to approach the the iodide in order to form hydrogen bonds, resulting in the shorter distance at low temperatures.

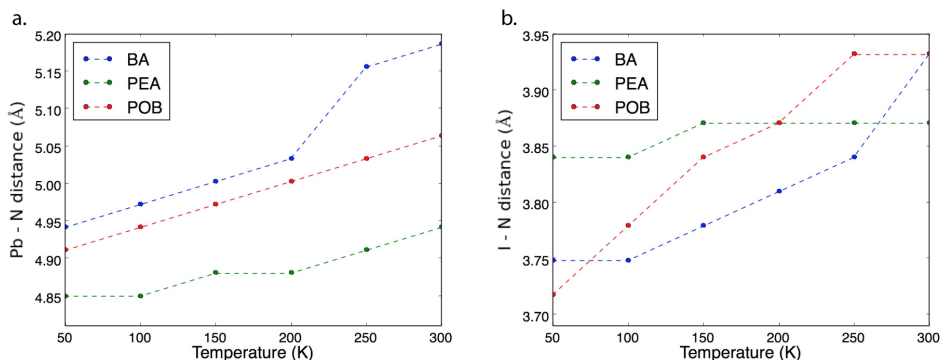


Figure 4.7 Positions of the first RDF peak. (a) lead & nitrogen and (b) iodide & nitrogen.

4

4.3.4 General discussion

The analysis above shows that the structural dynamics in 2D Ruddlesden-Popper perovskites are considerably affected by the nature of the organic component. The influence of the nature of the organic group connected to the amide is not restricted to the organic layer alone but also significantly affects the inorganic layer. For the BA compound this is clear in the phase transitions that take place in the materials. This phase transition leads to structural rearrangements in the inorganic layer, which is accompanied by a reduced rotational motion of the BA cation and a larger penetration of the amide into the inorganic layer. Introduction of an aromatic unit in the organic layer leads to substantially reduced structural fluctuations there. This reduction in fluctuations is transmitted to the inorganic layer when the aromatic unit is coupled to the amide with a short rigid linker such as an ethyl in the PEA-based material. This is consistent with experimental observations of the differences in structural rigidity between PEA and BA.^{24, 43} When the length of the linker is increased such as in the POB compound, the flexibility of the amide is increased, but the rigidity of the aromatic part of the material is maintained. The latter leads to a strongly enhanced resistance to moisture, while leaving the structural rigidity of the inorganic part unaffected. These observations have some interesting implications for the design of 2D halide perovskites. The results show that the structural softness of alkyl-based perovskites can be overcome by introducing aromatic side chains, however, the linker between the aromatic unit and the amide plays an important role in this. A short linker can transmit this increased rigidity to the inorganic framework while a longer flexible linker will allow for substantial fluctuations in the inorganic part.

4.4 Conclusions

In this chapter we show that the nature of the organic component has a marked effect on the structural rigidity of 2D Ruddlesden-Popper perovskites. Both the aromaticity of the organic component and the length of the aliphatic linker connecting it to the amine have a large influence on the structure and dynamics of the materials. Introduction of aromatic units such as a phenyl or a pyrene in the organic component result in a more rigid organic layer. The length of the aliphatic linker significantly affects the motion of the amide group, with a longer chain allowing more movement. These effects are not limited

to the behavior of the organic molecule itself but also directly affect the inorganic layer. More rigidity in the organic part due to aromatic interactions combined with a short rigid linker leads to less dynamic inorganic layers such as in the PEA structure considered. The results presented indicate that there is a subtle interplay between interactions in the organic and the inorganic parts of the material and that different aspects of the organic component that is used should be considered when designing new 2D hybrid perovskites.

4

References

1. Chen, Y.; Sun, Y.; Peng, J.; Tang, J.; Zheng, K.; Liang, Z., 2D Ruddlesden–Popper Perovskites for Optoelectronics. *Adv. Mater.* 2018, 30 (2), 1703487.
2. Yan, J.; Qiu, W.; Wu, G.; Heremans, P.; Chen, H., Recent Progress in 2D/Quasi-2D Layered Metal Halide Perovskites for Solar Cells. *J. Mater. Chem. A* 2018, 6 (24), 11063-11077.
3. Quan, L. N.; Rand, B. P.; Friend, R. H.; Mhaisalkar, S. G.; Lee, T.-W.; Sargent, E. H., Perovskites for Next-Generation Optical Sources. *Chem. Rev.* 2019, 119 (12), 7444-7477.
4. Kim, J.; Ho-Baillie, A.; Huang, S., Review of Novel Passivation Techniques for Efficient and Stable Perovskite Solar Cells. *Sol. RRL* 2019, 3 (4), 1800302.
5. Krishna, A.; Gottis, S.; Nazeeruddin, M. K.; Sauvage, F., Mixed Dimensional 2D/3D Hybrid Perovskite Absorbers: The Future of Perovskite Solar Cells? *Adv. Funct. Mater.* 2019, 29 (8), 1806482.
6. Yuan, M.; Quan, L. N.; Comin, R.; Walters, G.; Sabatini, R.; Voznyy, O.; Hoogland, S.; Zhao, Y.; Beauregard, E. M.; Kanjanaboos, P., et al., Perovskite Energy Funnels for Efficient Light-Emitting Diodes. *Nat. Nanotechnol.* 2016, 11 (10), 872-877.
7. Tsai, H.; Nie, W.; Blancon, J.-C.; Stoumpos, C. C.; Soe, C. M. M.; Yoo, J.; Crochet, J.; Tretiak, S.; Even, J.; Sadhanala, A., et al., Stable Light-Emitting Diodes Using Phase-Pure Ruddlesden–Popper Layered Perovskites. *Adv. Mater.* 2018, 30 (6), 1704217.
8. Li, M.; Wei, Q.; Muduli, S. K.; Yantara, N.; Xu, Q.; Mathews, N.; Mhaisalkar, S. G.; Xing, G.; Sum, T. C., Enhanced Exciton and Photon Confinement in Ruddlesden–Popper Perovskite Microplatelets for Highly Stable Low-Threshold Polarized Lasing. *Adv. Mater.* 2018, 30 (23), 1707235.
9. Zhang, H.; Liao, Q.; Wu, Y.; Zhang, Z.; Gao, Q.; Liu, P.; Li, M.; Yao, J.; Fu, H., 2D Ruddlesden–Popper Perovskites Microring Laser Array. *Adv. Mater.* 2018, 30 (15), 1706186.
10. Tsai, H.; Nie, W.; Blancon, J. C.; Stoumpos, C. C.; Asadpour, R.; Harutyunyan, B.; Neukirch, A. J.; Verduzco, R.; Crochet, J. J.; Tretiak, S., et al., High-Efficiency Two-Dimensional Ruddlesden–Popper Perovskite Solar Cells. *Nature* 2016, 536 (7616), 312-6.
11. Cao, D. H.; Stoumpos, C. C.; Yokoyama, T.; Logsdon, J. L.; Song, T.-B.; Farha, O. K.; Wasielewski, M. R.; Hupp, J. T.; Kanatzidis, M. G., Thin Films and

- Solar Cells Based on Semiconducting Two-Dimensional Ruddlesden-Popper $(\text{CH}_3(\text{CH}_2)_3\text{NH}_3)_2(\text{CH}_3\text{NH}_3)_n-1\text{SnI}_{3n+1}$ Perovskites. *ACS Energy Lett.* 2017, 2 (5), 982-990.
12. Ren, H.; Yu, S.; Chao, L.; Xia, Y.; Sun, Y.; Zuo, S.; Li, F.; Niu, T.; Yang, Y.; Ju, H., et al., Efficient and Stable Ruddlesden-Popper Perovskite Solar Cell with Tailored Interlayer Molecular Interaction. *Nat. Photonics.* 2020, 14 (3), 154-163.
 13. Mitzi, D. B., Synthesis, Crystal Structure, and Optical and Thermal Properties of $(\text{C}_4\text{H}_9\text{NH}_3)_2\text{MI}_4$ ($\text{M} = \text{Ge}, \text{Sn}, \text{Pb}$). *Chem. Mater.* 1996, 8 (3), 791-800.
 14. Stoumpos, C. C.; Cao, D. H.; Clark, D. J.; Young, J.; Rondinelli, J. M.; Jang, J. I.; Hupp, J. T.; Kanatzidis, M. G., Ruddlesden-Popper Hybrid Lead Iodide Perovskite 2D Homologous Semiconductors. *Chem. Mater.* 2016, 28 (8), 2852-2867.
 15. Saparov, B.; Mitzi, D. B., Organic-Inorganic Perovskites: Structural Versatility for Functional Materials Design. *Chem. Rev.* 2016, 116 (7), 4558-4596.
 16. Zibouche, N.; Islam, M. S., Structure-Electronic Property Relationships of 2D Ruddlesden-Popper Tin- and Lead-based Iodide Perovskites. *ACS Appl. Mater. Interfaces* 2020, 12 (13), 15328-15337.
 17. Cao, D. H.; Stoumpos, C. C.; Farha, O. K.; Hupp, J. T.; Kanatzidis, M. G., 2D Homologous Perovskites as Light-Absorbing Materials for Solar Cell Applications. *J. Am. Chem. Soc.* 2015, 137 (24), 7843-50.
 18. Blancon, J. C.; Stier, A. V.; Tsai, H.; Nie, W.; Stoumpos, C. C.; Traoré, B.; Pedesseau, L.; Kepenekian, M.; Katsutani, F.; Noe, G. T., et al., Scaling Law for Excitons in 2D Perovskite Quantum Wells. *Nat. Commun.* 2018, 9 (1), 2254.
 19. Deng, S.; Shi, E.; Yuan, L.; Jin, L.; Dou, L.; Huang, L., Long-Range Exciton Transport and Slow Annihilation in Two-Dimensional Hybrid Perovskites. *Nat. Commun.* 2020, 11 (1), 664.
 20. Hong, X.; Ishihara, T.; Nurmikko, A. V., Dielectric Confinement Effect on Excitons in PbI_4 -Based Layered Semiconductors. *Phys. Rev. B* 1992, 45 (12), 6961-6964.
 21. Straus, D. B.; Kagan, C. R., Electrons, Excitons, and Phonons in Two-Dimensional Hybrid Perovskites: Connecting Structural, Optical, and Electronic Properties. *J. Phys. Chem. Lett.* 2018, 9 (6), 1434-1447.
 22. Gong, X.; Voznyy, O.; Jain, A.; Liu, W.; Sabatini, R.; Piontkowski, Z.; Walters, G.; Bappi, G.; Nokhrin, S.; Bushuyev, O., et al., Electron-Phonon Interaction in Efficient Perovskite Blue Emitters. *Nat. Mater.* 2018, 17 (6), 550-556.
 23. Gao, Y.; Shi, E.; Deng, S.; Shiring, S. B.; Snider, J. M.; Liang, C.; Yuan, B.; Song, R.; Janke, S. M.; Liebman-Peláez, A., et al., Molecular Engineering of Organic-Inorganic Hybrid Perovskites Quantum Wells. *Nat. Chem.* 2019, 11 (12), 1151-1157.
 24. Seitz, M.; Magdaleno, A. J.; Alcazar-Cano, N.; Melendez, M.; Lubbers, T. J.; Walraven, S. W.; Pakdel, S.; Prada, E.; Delgado-Buscalioni, R.; Prins, F., Exciton Diffusion in Two-Dimensional Metal-Halide Perovskites. *Nat. Commun.* 2020, 11 (1), 2035.
 25. Liu, J.; Xue, Y.; Wang, Z.; Xu, Z.-Q.; Zheng, C.; Weber, B.; Song, J.; Wang, Y.; Lu, Y.; Zhang, Y., et al., Two-Dimensional $\text{CH}_3\text{NH}_3\text{PbI}_3$ Perovskite: Synthesis and Optoelectronic Application. *ACS Nano* 2016, 10 (3), 3536-3542.
 26. Du, K. Z.; Tu, Q.; Zhang, X.; Han, Q.; Liu, J.; Zauscher, S.; Mitzi, D. B., Two-Dimensional Lead(II) Halide-Based Hybrid Perovskites Templated by

- Acene Alkylamines: Crystal Structures, Optical Properties, and Piezoelectricity. *Inorg. Chem.* 2017, 56 (15), 9291-9302.
27. Quan, L. N.; Yuan, M.; Comin, R.; Voznyy, O.; Beauregard, E. M.; Hoogland, S.; Buin, A.; Kirmani, A. R.; Zhao, K.; Amassian, A., et al., Ligand-Stabilized Reduced-Dimensionality Perovskites. *J. Am. Chem. Soc.* 2016, 138 (8), 2649-55.
 28. Billing, D. G.; Lemmerer, A., Synthesis, Characterization and Phase Transitions in the Inorganic-Organic Layered Perovskite-Type Hybrids $[(\text{C}_n\text{H}_{2n+1}\text{NH}_3)_2\text{PbI}_4]$, $n = 4, 5$ and 6. *Acta Crystallogr. B* 2007, 63 (Pt 5), 735-47.
 29. Koh, T. M.; Shanmugam, V.; Guo, X.; Lim, S. S.; Filonik, O.; Herzig, E. M.; Müller-Buschbaum, P.; Swamy, V.; Chien, S. T.; Mhaisalkar, S. G., et al., Enhancing Moisture Tolerance in Efficient Hybrid 3D/2D Perovskite Photovoltaics. *J. Mater. Chem. A* 2018, 6 (5), 2122-2128.
 30. Lemmerer, A.; Billing, D. G., Synthesis, Characterization and Phase Transitions of the Inorganic-Organic Layered Perovskite-Type Hybrids $[(\text{C}(n)\text{H}(2n+1)\text{NH}_3)_2\text{PbI}_4]$, $n = 7, 8, 9$ and 10. *Dalton Trans.* 2012, 41 (4), 1146-57.
 31. Passarelli, J. V.; Fairfield, D. J.; Sather, N. A.; Hendricks, M. P.; Sai, H.; Stern, C. L.; Stupp, S. I., Enhanced Out-of-Plane Conductivity and Photovoltaic Performance in $n = 1$ Layered Perovskites through Organic Cation Design. *J. Am. Chem. Soc.* 2018, 140 (23), 7313-7323.
 32. Maheshwari, S.; Savenije, T. J.; Renaud, N.; Grozema, F. C., Computational Design of Two-Dimensional Perovskites with Functional Organic Cations. *J. Phys. Chem. C* 2018, 122 (30), 17118-17122.
 33. Gelvez-Rueda, M. C.; Fridriksson, M. B.; Dubey, R. K.; Jager, W. F.; van der Stam, W.; Grozema, F. C., Overcoming the Exciton Binding Energy in Two-Dimensional Perovskite Nanoplatelets by Attachment of Conjugated Organic Chromophores. *Nat. Commun.* 2020, 11 (1), 1901.
 34. Kamminga, M. E.; Fang, H.-H.; Filip, M. R.; Giustino, F.; Baas, J.; Blake, G. R.; Loi, M. A.; Palstra, T. T. M., Confinement Effects in Low-Dimensional Lead Iodide Perovskite Hybrids. *Chem. Mater.* 2016, 28 (13), 4554-4562.
 35. Marchal, N.; Van Gompel, W.; Gélvez-Rueda, M. C.; Vandewal, K.; Van Hecke, K.; Boyen, H.-G.; Conings, B.; Herckens, R.; Maheshwari, S.; Lutsen, L., et al., Lead-Halide Perovskites Meet Donor-Acceptor Charge-Transfer Complexes. *Chem. Mater.* 2019, 31 (17), 6880-6888.
 36. Plimpton, S., Fast Parallel Algorithms for Short-Range Molecular Dynamics. *J. Comput. Phys.* 1995, 117 (1), 1-19.
 37. Mattoni, A.; Filippetti, A.; Saba, M. I.; Delugas, P., Methylammonium Rotational Dynamics in Lead Halide Perovskite by Classical Molecular Dynamics: The Role of Temperature. *J. Phys. Chem. C* 2015, 119 (30), 17421-17428.
 38. Maheshwari, S.; Fridriksson, M. B.; Seal, S.; Meyer, J.; Grozema, F. C., The Relation between Rotational Dynamics of the Organic Cation and Phase Transitions in Hybrid Halide Perovskites. *J. Phys. Chem. C* 2019, 123 (23), 14652-14661.
 39. Ponder, J. W.; Case, D. A., Force Fields for Protein Simulations. *Adv. Protein Chem.* 2003, 66, 27-85.
 40. Breneman, C. M.; Wiberg, K. B., Determining Atom-Centered Monopoles from Molecular Electrostatic Potentials. The Need for High Sampling Density in Formamide Conformational Analysis. *J. Comput. Chem.* 1990, 11 (3), 361-373.

41. Frisch, M. J.; Trucks, G. W.; Schlegel, H. B.; Scuseria, G. E.; Robb, M. A.; Cheeseman, J. R.; Scalmani, G.; Barone, V.; Petersson, G. A.; Nakatsuji, H., et al. Gaussian 09 Rev. A.02, Wallingford, CT, 2016.
42. Du, K.-z.; Tu, Q.; Zhang, X.; Han, Q.; Liu, J.; Zauscher, S.; Mitzi, D. B., Two-Dimensional Lead(II) Halide-Based Hybrid Perovskites Templated by Acene Alkylamines: Crystal Structures, Optical Properties, and Piezoelectricity. *Inorg. Chem.* 2017, 56 (15), 9291-9302.
43. Gélvez-Rueda, M. C.; Peeters, S.; Wang, P.-C.; Felter, K. M.; Grozema, F. C., Effect of Structural Defects and Impurities on the Excited State Dynamics of 2D BA2PbI4 Perovskite. *Helv. Chim. Acta* 2020, 103 (7).

Appendix

Molecular dynamics parameters

The force field employed is based on the work of Mattoni et al.³⁷ and uses both Buckingham potential and Lennard-Jones potential to describe the interatomic interactions. The Buckingham potential (Equation A4.1) is used for inorganic-inorganic interactions as well as interaction between the inorganics and either a carbon or a nitrogen. All other interatomic interactions are described by the Lennard-Jones potential (Equation A4.2). The Buckingham potential parameters are obtained from Mattoni et al.³⁷ and can be seen in table A4.1. The Lennard-Jones parameters are obtained either from Mattoni et al.³⁷ or from the standard Amber force field³⁹ and can be seen in tables A4.2 – A4.4.

4

The intramolecular terms are obtained from the standard Amber force field.³⁹ The bonds and angles are described by the harmonic approximation (Equations A4.3 and A4.4) and the parameters can be found in tables A4.5 – A4.7 and A4.8 – A4.10 respectively. For the dihedrals the fourier approximation (Equation A4.5) is used and the parameters can be found in tables A4.11 – A4.13.

In this work we use full formal charges to the individual molecules. The partial charges on the individual atoms in BA, PEA and POB were obtained by fitting them to the electrostatic potential from a density functional theory calculation (B3LYP/cc-pVQZ) using the CHelpG approach⁴⁰ in the Gaussian09 software.⁴¹ The individual charges on each atom in the simulation can be seen in tables A4.14 – A4.16. In all the tables hydrogens connected to a carbon or a nitrogen are distinguished with a subscript with either a C or an N. Aliphatic and aromatic carbons are distinguished with brackets containing either al or ar. In the tables containing the atomic charges the carbons all have a number to separate them. In Figure A4.1 the molecules are shown with the carbon numbers.

$$E = Ae^{-r/\rho} - \frac{C}{r^6} \quad \text{A4.1}$$

Table A4.1 Buckingham potential coefficients for each atom pair, equivalent for all materials.

Pairs	A (Kcal/mole)	ρ (Å)	C (Å ⁶ ·Kcal/mole)
Pb-Pb	70359906.62970	0.131258	0.00
Pb-I	103496.13301	0.321737	0.00
I-I	22793.33858	0.482217	696.94954
Pb-N	32690390.93800	0.150947	0.00
Pb-C	32690390.93800	0.150947	0.00
Pb-O	32690390.93800	0.150947	0.00
I-N	112936.71421	0.342426	0.00
I-C	112936.71421	0.342426	0.00
I-O	112936.71421	0.342426	0.00

$$E = 4\epsilon \left[\left(\frac{\sigma}{r} \right)^{12} - \left(\frac{\sigma}{r} \right)^6 \right]$$

A4.2

Table A4.2 Lennard-Jones potential coefficients for each atom pair, BA.

Pairs	ϵ (Kcal/mole)	σ (Å)	Pairs	ϵ (Kcal/mole)	σ (Å)
Pb-H _s	0.01400	2.26454	N-H _c	0.0517	2.60500
Pb-H _c	0.01400	2.70999	C-C	0.10940	3.39970
I-H _s	0.0574	2.75000	C-H _s	0.04140	2.23440
I-H _c	0.0574	3.10000	C-H _c	0.04140	2.67980
N-N	0.17000	3.25000	H _s -H _s	0.01570	1.06910
N-C	0.13640	3.32480	H _s -H _c	0.01570	1.51450
N-H _s	0.0517	2.15950	H _c -H _c	0.01570	1.96000

Table A4.3 Lennard-Jones potential coefficients for each atom pair, PEA.

Pairs	ϵ (Kcal/mole)	σ (Å)	Pairs	ϵ (Kcal/mole)	σ (Å)
Pb-H _s	0.01400	2.26454	C(al)-H _c (al)	0.04144	3.39500
Pb-H _c	0.01400	2.70999	C(al)-H _c (ar)	0.04144	3.39500
I-H _s	0.0574	2.75000	C(ar)-C(ar)	0.08600	3.81600
I-H _c	0.0574	3.10000	C(ar)-H _s	0.03675	2.50800
N-N	0.17000	3.68400	C(ar)-H _c (al)	0.03675	3.39500
N-C(al)	0.13637	3.73200	C(ar)-H _c (al)	0.03675	3.39500
N-C(ar)	0.12091	3.73200	H _s -H _s	0.01570	1.20000
N-H _s	0.05166	2.42400	H _s -H _c (al)	0.01570	2.08700
N-H _c (al)	0.05166	3.31100	H _s -H _c (ar)	0.01570	2.08700
N-H _c (ar)	0.05166	3.31100	H _c (al)-H _c (al)	0.01570	2.97400
C(al)-C(al)	0.10940	3.81600	H _c (al)-H _c (ar)	0.01570	2.97400
C(al)-C(ar)	0.09700	3.81600	H _c (ar)-H _c (ar)	0.01570	2.97400
C(al)-H _s	0.04144	2.50800			

Table A4.4 Lennard-Jones potential coefficients for each atom pair, POB.

Pairs	ϵ (Kcal/mole)	σ (Å)	Pairs	ϵ (Kcal/mole)	σ (Å)
Pb-H _s	0.01400	2.26454	O-H _c (ar)	0.05166	3.17070
Pb-H _c	0.01400	2.70999	C(al)-C(al)	0.10940	3.81600
I-H _s	0.0574	2.75000	C(al)-C(ar)	0.09700	3.81600
I-H _c	0.0574	3.10000	C(al)-H _s	0.04144	2.50800
N-N	0.17000	3.68400	C(al)-H _c (al)	0.04144	3.39500
N-O	0.17000	3.50770	C(al)-H _c (ar)	0.04144	3.39500
N-C(al)	0.13637	3.73200	C(ar)-C(ar)	0.08600	3.81600
N-C(ar)	0.12091	3.73200	C(ar)-H _s	0.03675	2.50800
N-H _s	0.05166	2.42400	C(ar)-H _c (al)	0.03675	3.39500
N-H _c (al)	0.05166	3.31100	C(ar)-H _c (al)	0.03675	3.39500
N-H _c (ar)	0.05166	3.31100	H _s -H _s	0.01570	1.20000
O-O	0.17000	3.36740	H _s -H _c (al)	0.01570	2.08700
O-C(al)	0.13637	3.59170	H _s -H _c (ar)	0.01570	2.08700
O-C(ar)	0.12091	3.59170	H _c (al)-H _c (al)	0.01570	2.97400
O-H _s	0.05166	2.28370	H _c (al)-H _c (ar)	0.01570	2.97400
O-H _c (al)	0.05166	3.17070	H _c (ar)-H _c (ar)	0.01570	2.97400

$$E = K(r - r_0)^2$$

A4.3

Table A4.5 Bond coefficients, BA.

Bond	K (Kcal/mole/Å ²)	r, (Å)	Bond	K (Kcal/mole/Å ²)	r, (Å)
N-C(al)	276.638	1.48	C(al)-C(al)	306.432	1.508
N-H _s	443.528	1.028	C(al)-H _c (al)	342.991	1.093

Table A4.6 Bond coefficients, PEA.

Bond	K (Kcal/mole/Å ²)	r, (Å)	Bond	K (Kcal/mole/Å ²)	r, (Å)
N-C(al)	365.42326	1.48942	C(al)-C(ar)	315.86042	1.48789
N-H _s	421.96460	1.03880	C(ar)-C(ar)	436.40302	1.38337
C(al)-C(al)	290.71051	1.51445	C(ar)-H _c (ar)	368.92606	1.08345
C(al)-H _c (al)	340.00000	1.09000			

Table A4.7 Bond coefficients, POB.

Bond	K (Kcal/mole/Å ²)	r, (Å)	Bond	K (Kcal/mole/Å ²)	r, (Å)
N-C(al)	365.42326	1.48942	C(al)-O	320.00000	1.41000
N-H _s	421.96460	1.03880	O-C(ar)	450.00000	1.32300
C(al)-C(al)	290.71051	1.51445	C(ar)-C(ar)	436.40302	1.38337
C(al)-H _c (al)	340.00000	1.09000	C(ar)-H _c (ar)	368.92606	1.08345

$$E = K(\theta - \theta_0)^2$$

A4.4

Table A4.8 Angle coefficients, BA.

Angles	K (Kcal/mole/rad ²)	θ ₀ (°)	Angles	K (Kcal/mole/rad ²)	θ ₀ (°)
H _s -N-H _s	41.596	107.787	H _c -C-H _c	37.134	108.836
H _s -N-C	41.452	111.206	C-C-H _c	54.770	110.549
N-C-C	84.848	106.493	C-C-C	61.243	109.608
N-C-H _c	62.754	106.224			

Table A4.9 Angle coefficients, PEA.

Angles	K (Kcal/mole/rad ²)	θ ₀ (°)	Angles	K (Kcal/mole/rad ²)	θ ₀ (°)
H _s -N-H _s	36.37932	110.38305	C(ar)-C(al)-H _c (al)	49.63642	110.27836
H _s -N-C(al)	50.36054	108.47442	C(al)-C(al)-C(ar)	62.84255	112.57229
N-C(al)-C(al)	79.97299	111.33933	C(al)-C(ar)-C(ar)	69.82042	120.38660
N-C(al)-H _c (al)	50.00000	109.50000	C(ar)-C(ar)-C(ar)	62.88385	120.05976
H _c (al)-C(al)-H _c (al)	35.00000	109.50000	C(ar)-C(ar)-H _c (ar)	46.31522	119.62283
C(al)-C(al)-H _c (al)	50.00000	109.50000			

Table A4.10 Angle coefficients, POB.

Angles	K (Kcal/mole/rad ²)	θ_0 (°)	Angles	K (Kcal/mole/rad ²)	θ_0 (°)
H _s -N-H _s	36.37932	110.38305	O-C(al)-C(al)	50.00000	109.50000
H _s -N-C(al)	50.36054	108.47442	O-C(al)-H _c (al)	50.00000	109.50000
N-C(al)-C(al)	79.97299	111.33933	C(al)-O-C(ar)	60.00000	117.00000
N-C(al)-H _c (al)	50.00000	109.50000	O-C(ar)-C(ar)	80.00000	125.00000
H _c (al)-C(al)-H _c (al)	35.00000	109.50000	C(ar)-C(ar)-C(ar)	62.88385	120.05976
C(al)-C(al)-H _c (al)	50.00000	109.50000	C(ar)-C(ar)-H _c (ar)	46.31522	119.62283
C(al)-C(al)-C(al)	42.05979	109.66082			

$$E = \sum_i K_i [1.0 + \cos(n_i \phi - d_i)]$$

A4.5

Table A4.11 Dihedral coefficients, BA.

Dihedrals	i	K (Kcal/mole)	n	d (°)
H _s -N-C-H _c	1	0.13	3	0
H _s -N-C-C	1	0.093	3	0
N-C-C-H _c	1	0.346	1	0
	2	-0.265	2	180
	3	0.139	3	0
N-C-C-C	1	-0.324	1	0
	2	0.275	2	180
	3	0.295	3	0
H _c -C-C-H _c	1	0.142	1	0
	2	-0.693	2	180
	3	0.157	3	0
H _c -C-C-C	1	0.32	1	0
	2	-0.315	2	180
	3	0.132	3	0
C-C-C-C	1	0.051	1	0
	2	0.341	2	180
	3	0.166	3	0

Table A4.12 Dihedral coefficients, PEA.

Dihedrals	i	K (Kcal/mole)	n	d (°)
H _s -N-C(al)-H _c (al)	1	0.15600	3	0
H _s -N-C(al)-C(al)	1	0.15600	3	0
N-C(al)-C(al)-H _c (al)	1	0.15600	3	0
N-C(al)-C(al)-C(ar)	1	0.15600	3	0
H _c (al)-C(al)-C(al)-H _c (al)	1	0.15600	3	0
H _c (al)-C(al)-C(al)-C(ar)	1	0.15600	3	0
C(al)-C(al)-C(ar)-C(ar)	1	0.30000	3	0
H _c (al)-C(al)-C(ar)-C(ar)	1	0.30000	3	0
C(al)-C(ar)-C(ar)-C(ar)	1	3.18247	2	180
C(al)-C(ar)-C(ar)-H _c (ar)	1	3.18247	2	180
C(ar)-C(ar)-C(ar)-C(ar)	1	3.18247	2	180
C(ar)-C(ar)-C(ar)-H _c (ar)	1	3.18247	2	180
H _c (ar)-C(ar)-C(ar)-H _c (ar)	1	3.18247	2	180

Table A4.13 Dihedral coefficients, POB.

Dihedrals	i	K (Kcal/mole)	n	d (°)
H _s -N-C(al)-H _c (al)	1	0.15600	3	0
H _s -N-C(al)-C(al)	1	0.15600	3	0
N-C(al)-C(al)-H _c (al)	1	0.15600	3	0
N-C(al)-C(al)-C(al)	1	0.15600	3	0
H _c (al)-C(al)-C(al)-H _c (al)	1	0.15600	3	0
H _c (al)-C(al)-C(al)-C(al)	1	0.15600	3	0
C(al)-C(al)-C(al)-C(al)	1	0.15600	3	0
C(al)-C(al)-C(al)-O	1	0.15600	3	0
H _c (al)-C(al)-C(al)-O	1	0.15600	3	0
C(al)-C(al)-O-C(ar)	1	0.38300	3	0
H _c (al)-C(al)-O-C(ar)	1	0.38300	3	0
C(al)-O-C(ar)-C(ar)	1	1.05000	2	180
O-C(ar)-C(ar)-C(ar)	1	3.18247	2	180
O-C(ar)-C(ar)-H _c (ar)	1	3.18247	2	180
C(ar)-C(ar)-C(ar)-C(ar)	1	3.18247	2	180
C(ar)-C(ar)-C(ar)-H _c (ar)	1	3.18247	2	180
H _c (ar)-C(ar)-C(ar)-H _c (ar)	1	3.18247	2	180

Table A4.14 Charges of atoms, BA.

Atom	Charge	Atom	Charge	Atom	Charge
Pb	2.0000	C1	0.0955	C3	0.1411
I	-1.0000	H _{c1}	0.0794	H _{c3}	-0.0037
N	-0.4157	C2	-0.1045	C4	-0.1659
H _s	0.3366	H _{c2}	0.0534	H _{c4}	0.0605

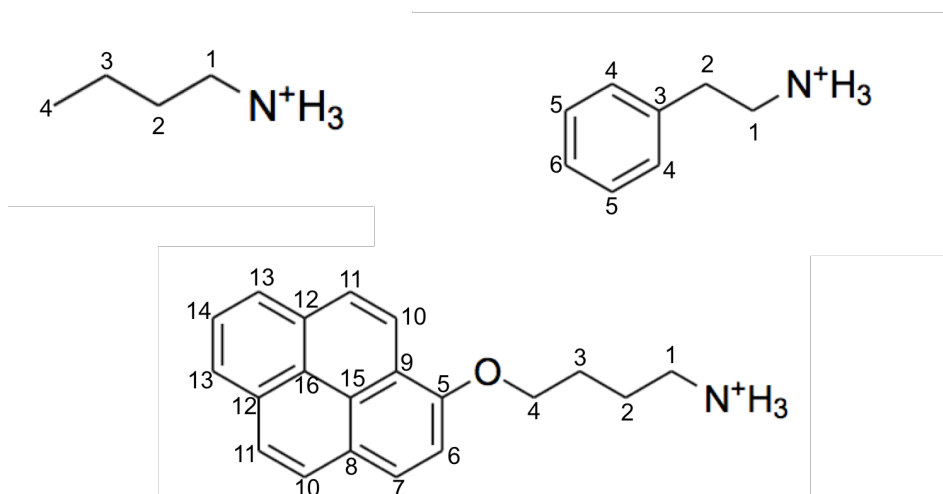


Figure A4.1 The molecules used with their carbons numbered in the same fashion as in the charge tables.

Table A4.15 Charges of atoms, PEA.

Atom	Charge	Atom	Charge	Atom	Charge
Pb	2.0000	H _{C1}	0.0277	H _{C4}	0.1177
I	-1.0000	C2	-0.2240	C5	-0.0565
N	-0.2645	H _{C2}	0.0857	H _{C3}	0.1066
H _N	0.2925	C3	0.1671	C6	-0.0601
C1	0.2061	C4	-0.1846	H _{C6}	0.1047

Table A4.16 Charges of atoms, POB.

Atom	Charge	Atom	Charge	Atom	Charge
Pb	2.0000	H _{C4}	-0.0457	C11	-0.2073
I	-1.0000	O	-0.3899	H _{C11}	0.1233
N	-0.3974	C5	0.1468	C12	0.2037
H _N	0.3253	C6	-0.1822	C13	-0.2312
C1	0.1477	H _{C5}	0.1281	H _{C13}	0.1214
H _{C1}	0.0590	C7	-0.1819	C14	-0.0090
C2	0.0068	H _{C7}	0.1187	H _{C14}	0.0923
H _{C2}	0.0200	C8	0.1413	C15	-0.0263
C3	-0.0869	C9	0.0735	C16	-0.0484
H _{C3}	0.0342	C10	-0.1372		
C4	0.4057	H _{C10}	0.1024		

Lead atom deviation from lead-iodide plane process

This is a method we use to examine the magnitude which the lead atoms are able to deviate from the lead-iodide plane in the different structures at different temperatures. This gives information about the rigidity of the lead iodide layer. For each simulation the coordinates of every lead atom at every time step are extracted and a histogram of the out of layer coordinate (the z-coordinate) is made. Since all the structures have two separate lead-iodide layers in their unit cell each histogram will have two separate peaks that each represent a single layer of lead ions. Every peak is fitted with a simple Gaussian function and the standard deviation extracted. The standard deviation is an indicator of the structural flexibility of the lead atoms in each layer. In a more rigid layer, the movement of the lead atoms in the direction perpendicular to the layer will be diminished and therefore give rise a narrower peak with a smaller standard deviation.

Radial distribution functions

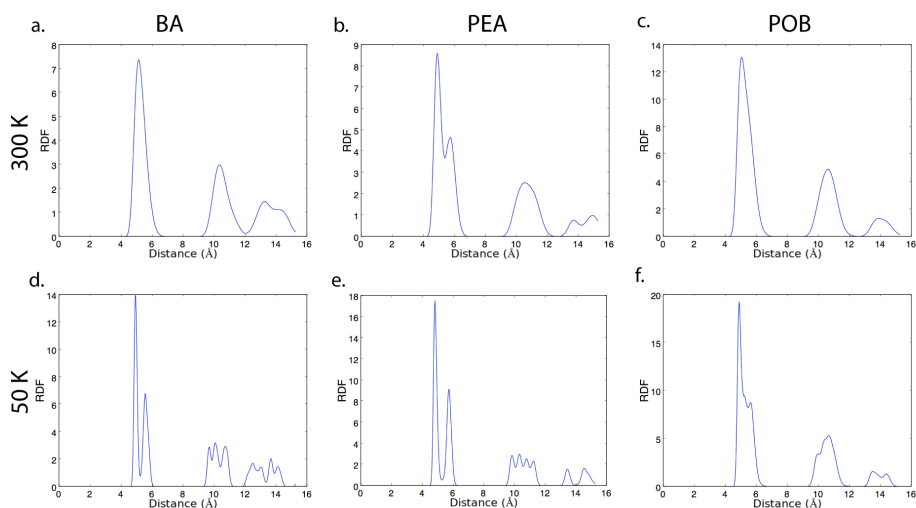


Figure A4.2 Radial distribution functions for lead & nitrogen for the different simulated structures at 300 K and 50 K. (a) BA at 300 K. (b) PEA at 300 K. (c) POB at 300 K. (d) BA at 50 K. (e) PEA at 50 K. (f) POB at 50 K.

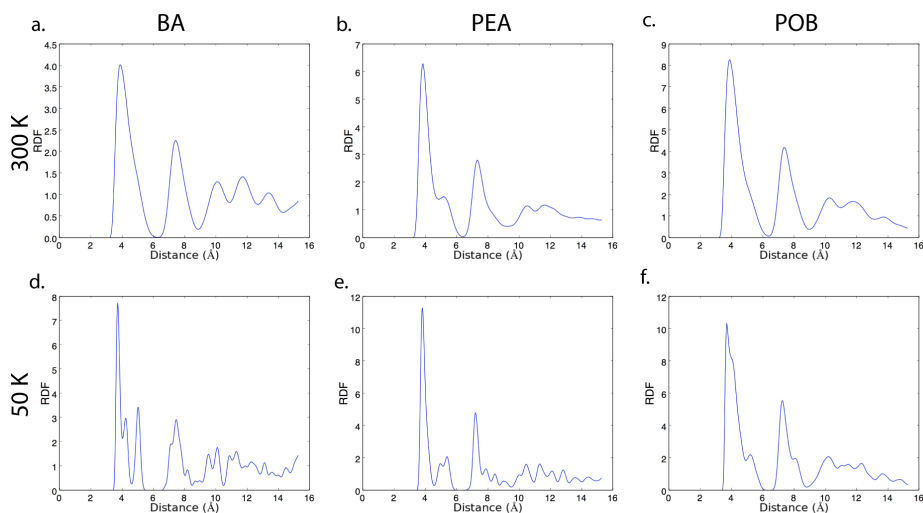


Figure A4.3 Radial distribution functions for iodide & nitrogen for the different simulated structures at 300 K and 50 K. (a) BA at 300 K. (b) PEA at 300 K. (c) POB at 300 K. (d) BA at 50 K. (e) PEA at 50 K. (f) POB at 50 K.

5



Trapping and De-Trapping in Colloidal Perovskite Nanoplatelets: Elucidation and Prevention of Non-Radiative Processes Through Chemical Treatment

Metal-halide perovskite nanocrystals show promise as the future active material in photovoltaics, lighting, and other optoelectronic applications. The appeal of these materials is largely due to the robustness of the optoelectronic properties to structural defects. The photoluminescence quantum yield (PLQY) of most types of perovskite nanocrystals is nevertheless below unity, evidencing the existence of non-radiative charge-carrier decay channels. In this work, we experimentally elucidate the non-radiative pathways in CsPbBr_3 nanoplatelets, before and after a chemical treatment with PbBr_2 that improves the PLQY. A combination of picosecond streak camera and nanosecond time-correlated single-photon counting measurements is used to probe the excited-state dynamics over six orders of magnitude in time. We find that up to 40% of the nanoplatelets from a synthesis batch are entirely nonfluorescent and cannot be turned fluorescent through chemical treatment. The other nanoplatelets show fluorescence, but charge-carrier trapping leads to losses that are prevented by chemical treatment. Interestingly, even without chemical treatment, some losses due to trapping are mitigated because trapped carriers spontaneously de-trap on nanosecond-to-microsecond timescales. Our analysis shows that multiple non-radiative pathways are active in perovskite nanoplatelets, which are affected differently by chemical treatment with PbBr_2 . More generally, our work highlights that in-depth studies using a combination of techniques are necessary to understand non-radiative pathways in fluorescent nanocrystals. Such understanding is essential to optimize synthesis and treatment procedures.

This chapter is based on: Vonk, S. J. W.^{||}; Fridriksson, M. B.^{||}; Hinterding, S. O. M.; Mangnus, M. J. J.; Van Swieten, T. P.; Grozema, F. C.; Rabouw, F. T.; van der Stam, W., J. Phys. Chem. C 2020, 124 (14), 8047-8054

^{||} These authors contributed equally to the work

5.1 Introduction

Research and development of lead–halide perovskite nanocrystals (NCs) has almost reached the same maturity as more conventional II–VI and III–V semiconductor nanomaterials, offering exciting properties such as narrow emission linewidths, fast excited-state decay, and high material gain.^{1–2} Furthermore, synthesis protocols for high-quality perovskite NCs of various compositions and shapes have been developed over the past five years.^{3–12} While the fluorescence of the conventional II–VI and III–V semiconductor NCs is strongly quenched unless their surface is covered with a wide-bandgap shell material, this is different for perovskite NCs.^{4, 13–16} The optical properties of perovskite NCs are less sensitive to (surface) defects than their II–VI and III–V counterparts, because the localized electronic states due to defects often lie outside the bandgap.^{17–18} Even simple synthesis procedures for single-component perovskite NCs, without shell, yield fluorescence with a photoluminescence quantum yield (PLQY) as high as a few tens of percent.^{4–5} Nevertheless, better synthesis methods,¹¹ ligand-exchange procedures,¹⁷ and other post-synthesis chemical treatments¹⁸ continue to be discovered that lead to even higher PLQY values. Clearly, structural imperfections in the interior of perovskite NCs or on their surface deteriorate the PLQY by opening non-radiative decay channels, but they can be removed or prevented if the right chemical methods are used. Unity PLQYs have been achieved for some compositions and shapes of perovskite NCs, but not yet for many others.^{19–21} The success of synthesis and treatment procedures in preventing non-radiative losses is usually evaluated in terms of the PLQY and excited-state decay dynamics of the resulting NCs. These parameters serve as feedback to optimize the chemical methods. However, batches of NCs are typically heterogeneous with strong interparticle-property variations. This complicates the ability of the community to identify the non-radiative loss pathways in an ensemble of NCs and, consequently, to evaluate and optimize the chemical procedures used.

In this chapter, we unravel the non-radiative processes in CsPbBr₃ nanoplatelets (NPLs), before and after chemical treatment with PbBr₂ that improves the PLQY. We analyze the excited-state dynamics over six orders of magnitude in time using a combination of integrating-sphere PLQY measurements, streak camera experiments, and time-correlated single-photon counting (TCSPC). We find that trapping of charge carriers occurs over a wide range of timescales, from sub-picosecond to nanoseconds.¹⁸ While some trapped charge carriers recombine non-radiatively, another part is de-trapped on longer timescales and contributes to delayed emission of photons up to several hundred nanoseconds after photoexcitation. Chemical treatment of the CsPbBr₃ nanoplatelets with PbBr₂ removes the picosecond-to-nanosecond trapping pathways, resulting in an increase of the PLQY. However, our combination of spectroscopic techniques reveals the presence of a “dark fraction” of entirely nonfluorescent NPLs that cannot be healed by chemical treatment with PbBr₂. Our results show that multiple non-radiative processes are operative in an ensemble of CsPbBr₃ NPLs, each with a distinct signature in the excited-state dynamics and with a distinct response to chemical surface treatment with PbBr₂. More broadly, our analysis method provides a framework to identify the effect of a chemical treatment on the non-radiative pathways in fluorescent nanomaterials.

5.2 Methods

5.2.1 Materials

Lead bromide (PbBr_2 , 99.999%), cesium carbonate (Cs_2CO_3 , 99%), oleic acid (OA, >99%), oleylamine (technical grade, 70%), anhydrous hexane, acetone and toluene were purchased from Sigma- Aldrich and used as received.

5.2.2 Precursor solution preparation

A Cs-oleate precursor solution was prepared by dissolving Cs_2CO_3 (0.1 mmol) in oleic acid (10 mL) at 100°C.²² A PbBr_2 treatment precursor solution was prepared by dissolving PbBr_2 (0.1 mmol) in a mixture of oleic acid (0.1 mL), oleylamine (0.1 mL) and hexane (10 mL) at 100°C. A PbBr_2 synthesis precursor was prepared by dissolving PbBr_2 (0.1 mmol) in a mixture of oleic acid (0.1 mL), oleylamine (0.1 mL) and toluene (10 mL) at 100°C. All mixtures were vigorously stirred and heated in order to dissolve the salts, after which transparent, colorless precursor solutions were obtained.

5.2.3 Synthesis and treatment of CsPbBr_3 nanoplatelets

The CsPbBr_3 nanoplatelets (NPLs) were all synthesized following the protocol of Bohn et al.¹⁸ In brief, for the synthesis of 4 monolayer (ML) CsPbBr_3 NPLs, 150 μL Cs-oleate precursor was injected into 1.2 mL PbBr_2 synthesis precursor, while continuously stirring the reaction solution. After ~5 s, 2 mL acetone was swiftly added in order to initiate the crystallization of the NPLs. After 1 min, the stirring was terminated and the solution was centrifuged (3500 rpm, 5 min) in order to separate the NPLs from unreacted precursor. For the synthesis of 6 ML NPLs, all synthesis steps are the same as described above, except for the amounts of (precursor) solution (250 μL Cs-oleate precursor, 1 mL PbBr_2 synthesis precursor with 0.3 mL acetone added, and 2.5 mL acetone). All syntheses were conducted under ambient conditions. To treat the NPLs, 0.1 mL of the PbBr_2 treatment precursor solution was added to diluted (10^{-8} M) NPL dispersions under vigorous stirring.

5.2.4 Steady-state optical spectroscopy

The absorbance of CsPbBr_3 NPL solutions was measured on a Perkin Elmer Lambda 900 UV/VIS/NIR Spectrometer. The steady-state photoluminescence (PL) was measured on an Edinburgh Instruments FLS980 Fluorescence Spectrometer, using a 450 W Xenon lamp as the excitation source (excitation wavelength 405 nm). PLQY measurements were carried out in the same device, using an integrating sphere. Solutions were measured in closed quartz cuvettes (pathlength 10 mm). Diluted solutions were prepared by adding 50–100 μL of the crude NPLs in hexane solution (concentration 10^{-8} M) to 3 mL hexane in quartz cuvettes, in order to reach an optical density at the excitation wavelength of 405 nm around 0.1.²³⁻²⁴

5.2.5 Transmission electron microscopy and x-ray diffraction

Transmission electron microscopy samples were prepared by drop-casting a dilute solution of NPLs in hexane on a carbon-coated copper TEM grid (400-mesh). TEM images and electron diffraction patterns were measured on a JEOL JEM-1400 TEM, operating at 120 kV. X-ray diffraction samples were prepared by drying a concentrated solution of NPLs, the dry powder was put on a silicon wafer. X-ray diffraction patterns were measured using a Bruker D2 Phaser using a Co X-ray source ($\lambda = 1.79 \text{ \AA}$).

5.2.6 Streak camera measurements

The time-resolved photoluminescence streak camera measurements were performed using a Hamamatsu C5680 streak camera setup. The samples were excited with a Chameleon Ultra II (Ti:Sapph) oscillator combined with a harmonic generator producing 140 fs pulses with a repetition rate of 80 MHz at a fluence of $\sim 1 \mu\text{J cm}^{-2}$ corresponding to an average number of excitons per pulse of $\langle N \rangle \approx 0.03\text{--}0.04$. This range is obtained by assuming an intrinsic absorption coefficient of CsPbBr_3 at 400 nm in hexane of $7.7 \times 10^4 \text{ cm}^{-1}$, lateral dimensions of $8 \text{ nm} \times 8 \text{ nm}$ and a NPL thickness of 2.4 nm (4ML) and 3.4 nm (6ML) giving absorption cross sections of $1.2 \times 10^{-14} \text{ cm}^2$ (4ML) and $1.7 \times 10^{-14} \text{ cm}^2$ (6ML).²⁴ The NPL dispersion was stirred during the measurement to minimize sedimentation and beam damage by the laser. An excitation wavelength of 405 nm was used in order to match the settings of the TCSPC pulsed laser. The time ranges of the streak camera measurements were 0.13 ns for the high-resolution measurement and 1.22 ns for the low-resolution measurement. The time resolution of the setup is 3 ps.

5

5.2.7 TCSPC measurements

Nanosecond time-correlated single-photon counting (TCSPC) measurements were performed on an Edinburgh Instrument FLS920 fluorescence spectrometer, using a PicoQuant pulsed diode laser (wavelength 405 nm) with a repetition rate of 0.5 MHz at a fluence of $\sim 0.1 \text{ nJ cm}^{-2}$. The NPL dispersion was stirred during the measurement to minimize sedimentation and beam damage by the laser. Emission events were time-correlated with the excitation pulses using an Edinburgh TCC900 computer card.

5.3 Results and discussion

5.3.1 CsPbBr_3 nanoplatelet synthesis and characterization before and after PbBr_2 treatment

Colloidal CsPbBr_3 NPLs of two thicknesses (4 and 6 monolayers, ML) were prepared following the procedure of Bohn et al.¹⁸ Sharp features are observed in the photoluminescence (PL) spectra, indicating controlled NPL thicknesses (Figure 5.1a). Surface treatment with a PbBr_2 precursor solution was performed on the NPLs,^{18, 22} which resulted in an enhancement of the PLQY (Figure 5.1b). Transmission Electron Microscopy (TEM) confirms the platelet shape of our NCs (Figure 5.1c,d). The variations in side length, which were also observed by Bohn et al.,¹⁸ have limited effect on the emission wavelength because this is determined by the thickness of the NPLs. X-ray diffraction confirms the CsPbBr_3 perovskite crystal structure of our NPLs (Appendix, Figure A5.1). In total, four NPL samples were prepared and studied in this work: 4ML, 4ML-treated, 6ML, and 6ML-treated CsPbBr_3 NPLs. The main text will focus mainly on the data obtained for the 4ML and 4ML-treated NPLs. All measurements in the manuscript were conducted one day after synthesis, so that the picosecond-to-nanosecond excited-state dynamics and the PLQY could be directly combined and compared without complications due to slow degradation over the timescale of days to weeks.

5.3.2 Photoluminescence decay measurements on picosecond, nanosecond and microsecond timescales

We studied the excite-state dynamics of the NPLs using picosecond streak camera (Figure 5.2a) and nanosecond TCSPC measurements (Figure 5.2b). By measuring the excited-

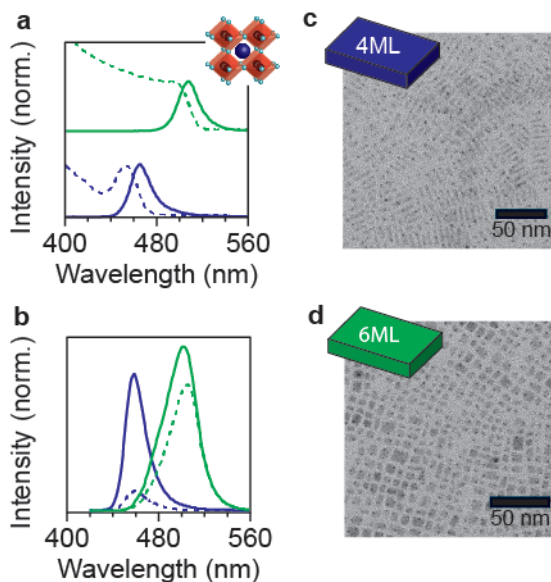


Figure 5.1 Optical and structural characterization of CsPbBr₃ nanoplatelets. (a) Steady-state absorption (dashed lines) and photoluminescence (solid lines) spectra of CsPbBr₃ nanoplatelets with a thickness of 4ML (dark blue) and 6ML (green). The inset shows the perovskite crystal structure (blue sphere; Cs⁺, black sphere; Pb²⁺, light blue sphere; Br⁻). (b) Photoluminescence spectra normalized to PLQY before (dashed lines, 4ML 10.2%, 6ML 50.8%) and after PbBr₂ treatment (solid lines, 4ML 44.2%; 6ML 68.8%). Transmission electron microscopy (TEM) images of (c) 4ML thick and (d) 6ML thick CsPbBr₃ NPLs.

state decay with TCSPC as a function of the photon energy using a monochromator, we obtain a 2D map of the excited-state dynamics vs. energy, i.e. time-resolved emission spectra (TRES). Using both techniques—streak camera and TRES—we are able to resolve the spectral position, linewidth and intensity over a wide range of delay times (Figure 5.2a,b). We keep the laser excitation fluence low (estimated to yield on average 0.03 excitons per NPL per pulse for the streak camera measurement; see Appendix) to minimize the creation of multiexcitons and the influence of Auger recombination on the decay dynamics.

The peak emission energy and linewidth remain nearly constant over the entire experimental time range (Figure 5.2c,d). This indicates that radiative recombination of the photogenerated charge carriers occurs always from the same exciton state irrespective of the timescale. Because of the sub-picosecond cooling time of hot charge carriers,²⁵ this must be the lowest-energy exciton state, whose energy is dependent on the thickness of the NPLs through quantum confinement effects (Figure 5.1). We ascribe the small (~3 nm) shift of the emission peak over the first 20 ns to slight inhomogeneous broadening and a wavelength-dependent density of optical states.²⁶

Although the narrow linewidth in the TRES measurements (Figure 5.2b) indicates

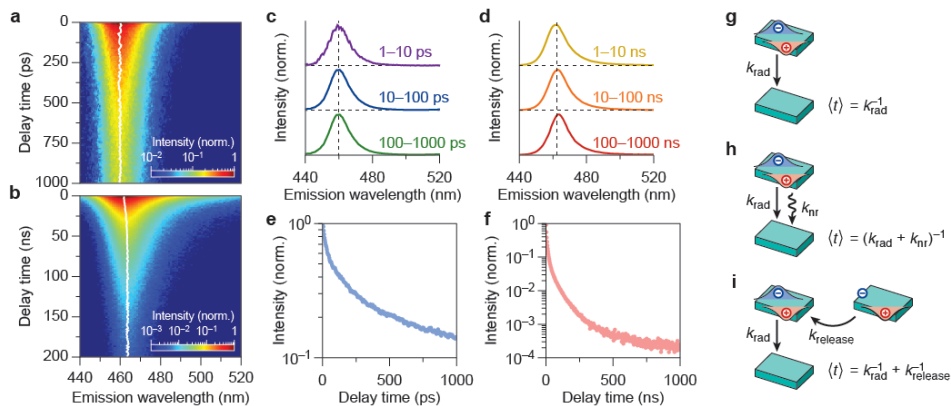


Figure 5.2 Picosecond streak camera measurements and time-correlated single-photon counting on 4-monolayer CsPbBr₃ nanoplatelets. (a) Streak camera image measured over the first 1000 ps and (b) time-resolved emission spectrum measured over the first 200 ns after photoexcitation for untreated 4ML CsPbBr₃ NPLs. Spectral slices measured with (c) the streak camera and (d) TCSPC show that the spectral position (white line in panels (a) and (b)) and width remain nearly constant over the entire time range. The constant 2 nm shift of the peak position between the two different measurements is due to calibration differences between the TCSPC and streak camera setup. PL decay traces obtained by (e) streak camera (from 0 to 1000 ps) and (f) TCSPC (from 0 to 1000 ns) measurements, showing multi-exponential decay. Schematic representation of the radiative and non-radiative processes that typically occur in nanomaterials: (g) radiative recombination, where an excitation is directly followed by photon emission, (h) non-radiative recombination, which results in energy losses and shortens the timescale of photon emission, and (i) temporary storage of charge carriers and subsequent release leads to delayed emission of photons.

radiative recombination from identical 4ML nanoplatelets, the PL decay curves (Figures 5.2e,f) show multi-exponential excited-state dynamics. This suggests a variation in non-radiative processes within subpopulations of NPLs in the sample. As reported previously,^{18, 22, 27-28} and as we investigate in more detail below, the radiative decay rate k_{rad} of the lowest-energy exciton state in perovskite NCs is on the order of $k_{\text{rad}} = 0.1\text{--}1\text{ ns}^{-1}$.¹⁸ Based on this rate, we expect an average delay time of $\langle t \rangle = k_{\text{rad}}^{-1} = 1\text{--}10\text{ ns}$ (Figure 5.2g) if no other recombination pathways are active. However, the PL decay curve measured here clearly contains significantly faster (Figure 5.2e) as well as slower (Figure 5.2f) decay components. The decay components faster than the radiative rate can be ascribed to non-radiative trapping processes from imperfect NPLs in the sample, which are in competition with radiative recombination. Non-radiative trapping at rate k_{nr} shortens the timescale of emission (Figure 5.2h) to $\langle t \rangle = (k_{\text{rad}} + k_{\text{nr}})^{-1}$. If the charge carriers recombine non-radiatively after trapping, this lowers the PLQY. The decay components slower than the radiative rate can also be due to non-radiative processes. Trapping of a charge carrier, followed by de-trapping at rate k_{release} and radiative recombination at rate k_{rad} will increase the timescale of emission to $\langle t \rangle = k_{\text{rad}}^{-1} + k_{\text{release}}^{-1}$ (Figure 5.2i, Appendix for derivation). However, since this sequence of processes yields a photon eventually, it does not affect the PLQY. This photon emission following trapping and de-trapping is often referred to as delayed emission and has been shown to influence the PL dynamics in perovskite NCs²⁸⁻³⁰ as well as other materials.³¹⁻³³ Below, we will study both non-radiative processes (trapping/

non-radiative recombination and trapping/de-trapping) and characterize the influence of the PbBr_2 surface treatment on these non-radiative processes.

5.3.3 Stitching the PL decay curves together and modeling of the non-radiative processes

In Figure 5.3a we combine the streak camera and TCSPC measurements over six orders of magnitude in time by stitching them together. This procedure is detailed in the Appendix. In addition to the PL decay trace, the PLQY measured with an integrating sphere also contains information about non-radiative processes. We combine the information from all measurements by defining the “quantum yield density” $\phi(t)$, which is obtained by normalizing the stitched PL decay data such that the total area, i.e. the time-integrated quantum yield density, equals the PLQY:

$$\int_0^{\infty} \phi(t) dt = \text{PLQY}. \quad 5.1$$

The quantum yield density has units of inverse time and represents the photon emission probability per unit delay time per absorption event from the ensemble of NPLs. The quantum yield density plot contains information about the fast trapping—even those processes that are faster than the instrument response of our streak camera—as well as the slow de-trapping processes.

Figures 5.3b–e illustrate how we quantify different non-radiative processes by analyzing the quantum yield density plot $\phi(t)$, under the assumption that all NPLs have the same intrinsic radiative decay rate k_{rad} . In the simplest scenario (Figure 5.3b, blue), radiative recombination of the exciton is the only decay pathway and no competing non-radiative processes in any of the NPLs in the ensemble are present. In this case, the PLQY would be unity and the quantum yield density would follow single-exponential decay, i.e. $\phi(t) = k_{\text{rad}} \exp(-k_{\text{rad}} t)$.

In practice, batches of NCs typically contain a “dark fraction”,³⁴ i.e. some NCs do not emit any photons upon photoexcitation and are therefore not directly observable in spectroscopic measurements.^{34–36} This dark fraction of entirely nonfluorescent NPLs that we identify below is qualitatively different from the “dark NPLs” with weak and fast fluorescence that Bohn et al. discuss.¹⁸ The presence of a truly dark fraction has a large influence on the quantitative analysis of the decay processes.³⁷ Photogenerated excitons in these dark NPLs are quenched by ultrafast non-radiative charge carrier recombination, which may even outcompete the thermalization rate to the band edge. This subpopulation is invisible in the PL decay traces but does show up in the PLQY measurements. Figure A5.3 in the Appendix discusses the concept of a dark fraction in more detail and provides an analysis strategy to identify if a dark fraction is present in a NC sample. Figure 5.3c (green) shows the quantum yield density for the scenario that a fraction $1-f$ of NPLs is dark, while the other NPLs (bright fraction f) exhibit exclusively radiative decay, which follows $\phi(t) = f k_{\text{rad}} \exp(-k_{\text{rad}} t)$. From the amplitude $\phi(0) = f k_{\text{rad}}$ of the quantum yield density plot we can thus estimate the bright fraction within the NPL ensemble:

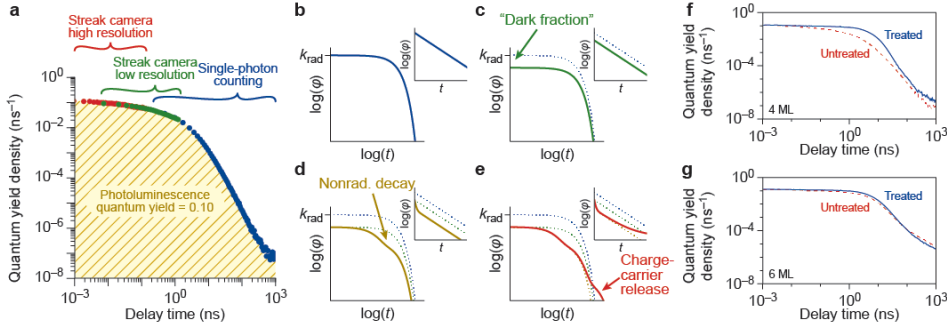


Figure 5.3 Stitching of streak camera and TCSPC measurements. (a) Example of the combination of high- and low-resolution streak camera measurements with time-correlated single-photon counting (TCSPC) measurements for a sample of untreated 4ML nanoplatelets (NPLs) in order to obtain a photoluminescence (PL) decay trace over 6 orders of magnitude in time. The area under the PL decay curve is normalized to the PLQY of 10.2%, yielding what we define as the quantum yield density $\varphi(t)$. (b) Model of the PL decay trace on a double logarithmic scale (and semi logarithmic inset) in case all generated charge carriers recombine radiatively (PLQY = 100%). (c) Model of the PL decay trace, in case a fraction of the NPLs is dark, resulting in a decrease of the amplitude, since the extremely fast dynamics of the dark fraction is masked by the instrument response function. (d) Model of the PL decay trace, but in addition to the model in (c), part of the bright fraction NPLs exhibit non-radiative recombination that is in competition with radiative recombination. (e) Model of the PL decay trace, but in addition to the model in (d), delayed photons are taken into account, i.e. radiative recombination of charge carriers after temporary storage in a non-emissive state. (f) Experimental PL decay traces for untreated (dashed line) and PbBr_2 treated (full line) 4ML CsPbBr_3 NPLs. (g) Same, but for 6ML CsPbBr_3 NPLs.

$$f = \frac{\varphi(0)}{k_{\text{rad}}}.$$

5.2

Figures 5.3d,e illustrate the additional features that may appear in the quantum yield density plots if a fraction of NPLs in the sample exhibit trapping of charge carriers which can lead to non-radiative recombination (Figure 5.3d, yellow), or de-trapping and subsequent delayed emission of photons on longer timescales (Figure 5.3e, red). These processes introduce additional components in the quantum yield density plots that are faster (non-radiative recombination) or slower (delayed emission) than the radiative recombination, respectively (see Figures 5.2g-i).

Figure 5.3f shows the experimental quantum yield density plot $\varphi(t)$ of the untreated and treated 4ML NPL samples, and Figure 5.3g for the untreated and treated 6ML NPL samples. We see that the untreated and treated samples have very similar amplitudes $\varphi(0)$, indicating that the treatment with PbBr_2 does not affect the dark fraction of NPLs (see model in Figure 5.3c). In addition, we observe that the treatment process makes the decay dynamics on the picosecond-to-nanosecond timescales (< 10 ns) slower. This is consistent with a suppression of non-radiative trapping pathways in imperfect NPLs by the PbBr_2 treatment. Finally, we observe additional slow (> 50 ns) multi-exponential components in the quantum yield density $\varphi(t)$ for all samples, associated with delayed emission of

photons following trapping and de-trapping (Figure 5.2i). Interestingly, the contribution of the delayed emission events to the total amount of emitted photons changes with treatment. From these measurements, we conclude that the PbBr_2 treatment procedure affects the non-radiative processes contributing to non-radiative recombination in the bright fraction of NPLs, as well as those contributing to delayed emission, whereas the dark fraction is unaffected by the treatment.

5.3.4 Identifying radiative and non-radiative processes in CsPbBr_3 NPLs ensembles

For a more quantitative analysis of the non-radiative processes in our NPL samples, we have to determine the radiative decay rates k_{rad} . For example, the value of k_{rad} is necessary for a quantitative identification of the dark fraction (Equation 5.2) and the distinction between charge-carrier trapping followed by non-radiative recombination (Figure 5.3d) or delayed emission (Figure 5.3e).

We measured the excited-state decay of three independently synthesized samples of 4ML NPL with slightly different PLQY (see Figure 5.4a). The fitted lifetime of the excited state is constant (blue line) indicating that the synthesis procedure gives synthesis-to-synthesis variations in the dark fraction. An alternative explanation—where the PLQY changes due to a variation in non-radiative rates—would result in a positive slope of the lifetime of the excited state vs. the PLQY (red dashed line, see Appendix for details) which does not follow the data. From this, we conclude that the slowest decay dynamics of the treated NPLs on the 1–10 ns timescale are predominantly due to k_{rad} . From the measurements on the treated samples, we extract $k_{\text{rad}} = 1/(5.6 \text{ ns})$ for the 4ML NPLs and $k_{\text{rad}} = 1/(5.7 \text{ ns})$ for

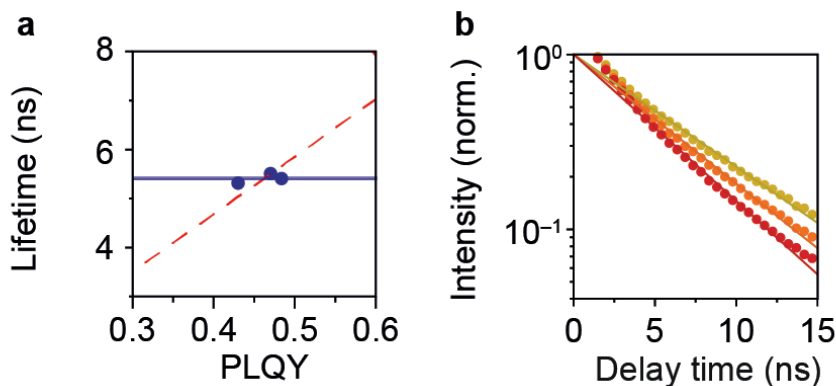


Figure 5.4 Determination of the radiative decay rate. (a) Lifetime vs. PLQY for three independently synthesized treated 4ML NPL samples. The lifetime of the excited state is approximately constant $k_{\text{rad}} = 1/(5.6 \text{ ns})$, independent of the PLQY, indicating variations in the dark fraction from sample to sample (blue line). The red dashed line shows the expected trend if the non-unity PLQY were due to non-radiative decay in each NPL (rather than a dark and bright fraction), with sample-to-sample variations in PLQY due to sample-to-sample variations in k_{nr} . (b) Decay curve for treated 6ML NPL of one synthesis batch dispersed in hexane ($n = 1.375$, dark yellow), toluene ($n = 1.5$, orange) and CS_2 ($n = 1.63$, red). The lifetime of the excited state decreases for increasing refractive index n showing that the total decay rate is dominated by radiative processes.

the 6ML NPLs. This is approximately a factor 2 faster than the radiative rate estimated by Bohn et al.,¹⁸ since we take into account that the dark fraction of NPLs is the cause for most of the losses in the ensemble, while most fluorescent NPLs show purely radiative decay.³⁷ The absolute values for k_{rad} for the two samples are determined by the electronic structure of the NPLs, including the thermal occupation of various exciton fine structure states,³⁸ and photonic effects, including a shape-dependent local field factor.¹ To further confirm that the ns-component in the PL decay dynamics is due to radiative decay, we measured the excited-state decay using TCSPC on 6ML NPLs in different photonic environments by changing the solvent (see Figure 5.4b). We observe that the lifetime of the excited state becomes faster for increasing the refractive index from $n = 1.374$ [hexane, dark yellow, $k_{\text{rad}}=1/(6.8 \text{ ns})$] to $n = 1.63$ [CS_2 , red, $k_{\text{rad}}=1/(5.2 \text{ ns})$]. This is consistent with a change in the radiative rate of the NPLs due to an increase of the local density of optical states.

5

Using these values for k_{rad} and the concepts explained in Figure 5.3b–e, we identify and quantify the different non-radiative processes at play in the sample of untreated 4ML NPLs in Figure 5.5a. The red line is the experimental quantum yield density plot $\phi(t)$ obtained after stitching of the PL streak camera and TCSPC measurements. The yellow line is a multi-exponential fit (to account for variations of non-radiative trapping rates between subpopulations of NPLs) to the first 20 ns of which the slowest fit component is fixed to k_{rad} . This captures the excited-state dynamics due to picosecond-to-nanosecond charge-carrier trapping from the band-edge exciton state (see Figure 5.3d) but excludes delayed emission on timescales longer than $1/k_{\text{rad}}$ (see Figure 5.3e). The blue line (Figure 5.3b) is the hypothetical quantum yield density assuming a unity PLQY sample, i.e. no dark fraction, decaying with the radiative rate k_{rad} . The green line (Figure 5.3c) shows the calculated quantum yield density we would measure if the bright fraction f suffered no band-edge losses, in which case the excited-state dynamics would follow single-exponential decay with the radiative rate k_{rad} .

By integrating the appropriate areas between the curves in Figure 5.5a, we estimate the probabilities of different decay pathways in our NPL ensemble and thus the influence of the various non-radiative processes. Because the quantum yield density is normalized to the PLQY (Equation 5.1), integration immediately yields the probabilities of decay pathways per photon absorption event. Specifically, in this way we obtain the probability of prompt photon emission (yellow-shaded area), the band-edge losses due to charge carrier trapping (green-shaded area), and the losses due to the dark fraction of NPLs (blue-shaded area). In addition, the red-shaded area represents the delayed emission on timescales exceeding prompt emission. Figures 5.5b–d show the same plots and analysis for the treated 4ML NPLs (Figure 5.5b), the untreated 6ML NPLs (Figure 5.5c), and the treated 6ML NPLs (Figure 5.5d).

From these plots, it becomes clear that in a fraction of NPLs charge carriers are ‘lost’ by trapping on the sub-picosecond timescale (blue-shaded area) and/or picosecond-to-nanosecond (green-shaded area) timescale. Delayed emission (red-shaded areas in Figures 5.5a–d) is due to de-trapping of charge carriers and subsequent photon emission on long timescales compared to prompt emission. To determine the timescales of trapping and release and how the treatment affects it, we plot the contribution of delayed emission

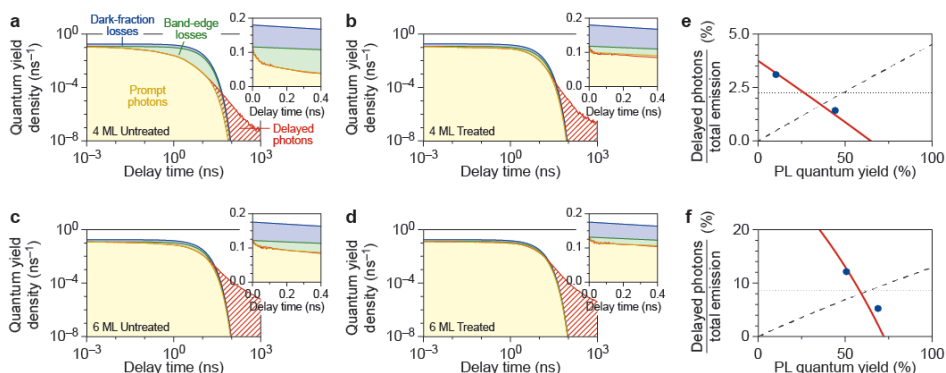


Figure 5.5 Identifying the radiative and non-radiative processes from the PL decay traces. (a–d) Stitched experimental PL decay traces (solid red line) and the comparison to the model distinguishing the contribution of prompt photons (yellow-shaded area), band-edge losses (green-shaded area), the dark fraction (blue-shaded area) and delayed PL (red-shaded area) for (a) untreated and (b) PbBr_2 -treated 4ML CsPbBr_3 NPLs, and (c) untreated and (d) PbBr_2 -treated 6ML CsPbBr_3 NPLs. The insets show a zoom of the first 400 ps. (e,f) Plots of the percentage of delayed photons with respect to the total number of emitted photons versus the PLQY, before and after treatment for (e) 4ML NPLs and (f) 6ML NPLs, and the comparison to the different possible models for temporary trapping and how it is affected by chemical treatment (Appendix for details): hot-exciton trapping with a constant rate (dotted lines), band-edge exciton trapping with a constant rate (dashed line) and band-edge exciton trapping with a rate that changes to the same extent as the non-radiative recombination rate (red solid line).

to the total emission, against the ensemble PLQY in Figure 5.5e (4ML NPLs) and Figure 5.5f (6ML NPLs).

As can be seen in Figure 5.5e,f, the delayed-emission fraction (contribution of delayed emission to the integrated quantum yield density) decreases as the PLQY increases by PbBr_2 treatment. From this analysis, we have to conclude that surface treatment not only suppresses non-radiative recombination pathways for the bright NPLs, but also has a profound influence on temporary charge carrier trapping and de-trapping. There are three possible scenarios that we consider for the effect of treatment on the rates of non-radiative processes in our NPLs (detailed explanation in Appendix). If only the non-radiative recombination rate k_{nr} is suppressed by the chemical treatment, we can calculate the delayed-emission fraction as a function of the PLQY assuming trapping from (1) a hot exciton state (Figure 5.5e,f dotted line) or (2) from a band-edge exciton state (Figure 5.5e,f dashed line). Neither scenario reproduces the measurements of the delayed-emission fraction before and after treatment. However, if we assume that the treatment suppresses (3) non-radiative recombination k_{nr} as well as temporary trapping k_{trap} from the band-edge exciton to the same extent, i.e. both rates are reduced by the same factor, we reproduce the delayed-emission fraction dependence on PLQY before and after treatment for both NPL samples (Figure 5.5e,f red lines).

We conclude from this analysis that trapping from the band-edge exciton state is

the dominant mechanism contributing to delayed emission in perovskite NPLs. Additionally, we identified that the process leading to non-radiative recombination (i.e., trapping followed by recombination) and temporary trapping (i.e., trapping followed by de-trapping) is affected to the same extent by a chemical treatment with PbBr_2 . This might indicate that the defects that are responsible for these two processes have the same chemical nature. As charge-carrier trapping on these defects can be reversible (giving rise to delayed emission), the defect probably acts as a “shallow trap state”, i.e. close in energy to the conduction- or valence-band edge. Indeed, undercoordinated Pb may lead to such shallow trap states, whose density is expected to decrease by chemical treatment of the NPLs with excess PbBr_2 .¹³

5.3.5 Quantifying the contribution of non-radiative and radiative processes

Figure 5.6a schematically summarizes the various excited-state decay pathways of an ensemble of perovskite NPLs that we studied with our combined PL decay and PLQY measurements. After excitation from the ground state (0) to a hot-carrier state (1), some NPLs in the ensemble decay non-radiatively on sub-picosecond timescales leading to dark-fraction losses (blue). In the other subpopulation of NPLs, charge carriers quickly thermalize to form a band-edge exciton (2). From this lowest-energy exciton state, there is a probability to recombine radiatively, yielding prompt photons (yellow). Alternatively, in imperfect subpopulations of NPLs, radiative recombination can be in competition with non-radiative trapping from the lowest-energy exciton state followed by non-radiative recombination, leading to band-edge losses (green). Some of these trapping events from the lowest-energy exciton state do not result in non-radiative recombination, but instead the trapped charge (3) is de-trapped after some time. After de-trapping and restoration of the lowest-energy exciton, radiative recombination can occur contributing to delayed emission of photons (red).

We plot the contributions of the different decay pathways by subpopulations of NPLs for the different batches (4ML and 6ML) in Figure 5.6b. The contributions of dark-fraction losses (blue), band-edge losses (green), and prompt photon emission (yellow) add up to 100%, but the numbers are rounded to the nearest 1%. The emission of delayed photons (red) compensates for part of the band-edge losses. Clearly, the main effect of PbBr_2 treatment is enhancement of the prompt emission (yellow) and suppression of band-edge trapping (green), while the dark-fraction remains similar. Therefore, to approach unity PLQY values for CsPbBr_3 perovskite NPLs, an alternative post-synthetic chemical treatment appears necessary that can heal the dark fraction.

The effect of PbBr_2 treatment on the absolute delayed-emission intensity is nontrivial: the delayed-emission intensity increases for the 4ML NPLs, but decreases for the 6ML NPLs. This can be understood by considering that delayed emission follows a multi-step pathway: (i) a charge carrier is first trapped from the band-edge exciton state, (ii) released, and then (iii) recombines radiatively. On the one hand, treatment suppresses non-radiative recombination of the band-edge exciton, so that steps (i) and (iii) become more efficient and delayed emission thus more likely. On the other hand, treatment also suppresses trapping of carriers into temporary traps, as we have elucidated in Figures

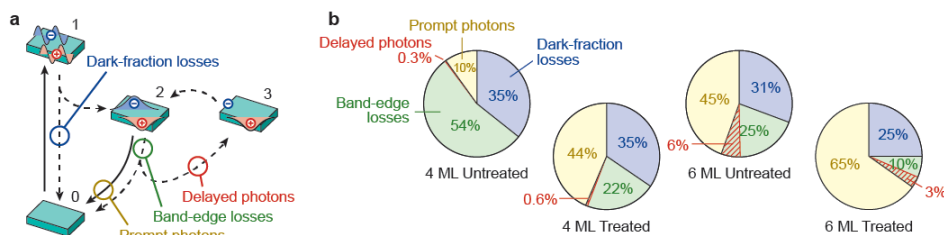


Figure 5.6 Models for radiative and non-radiative processes in CsPbBr₃ nanoplatelets. (a) Schematic summary of the radiative and non-radiative processes at play in subpopulations of an ensemble of CsPbBr₃ NPLs. After photoexcitation from the ground state (0) to the excited state (1), hot charge carriers are initially generated. In some NPLs—the dark fraction—non-radiative recombination is so fast that it outcompetes thermalization to the band-edge exciton state. The hot charge carriers can also cool to the band edge (2), from which there is a probability to recombine radiatively (prompt emission of photons) or get trapped (band-edge losses). Some NPLs trap charge carriers temporarily (3), i.e. they are subsequently de-trapped and eventually recombine from the lowest-energy exciton state (delayed photons). (b) The contributions of radiative recombination (prompt photons, yellow area), band-edge losses (green area) and dark-fraction losses (blue area) of our four samples of NPLs. The red-shaded area denotes band-edge trapping that is followed by de-trapping and delayed emission. Comparing the untreated and treated samples, it is evident that chemical treatment with PbBr₂ suppresses band-edge trapping while the dark-fraction is hardly influenced.

5.5e,f, thus making delayed emission less likely. This balance between competing effects is well captured by the model we show in Figures 5.5e,f (see also Appendix Figure A5.4). This model shows that while the delayed-emission fraction of the total emission always decreases with treatment (Figure 5.5e,f), the absolute intensity of delayed emission may or may not increase if the NPLs become significantly brighter overall (Figure 5.6b).

We showed with our analysis method that the PLQY is increased because of reduced band-edge losses. However, the treatment procedure still does not yield CsPbBr₃ NPLs with unity PLQY. Our results indicate that the defect chemistry of perovskite nanomaterials is complex, and that the main factor that needs to be tackled in order to reach unity PLQY values for this interesting class of materials, is the dark fraction of NPLs within the ensemble. Future research into the atomic-scale structural details^{27, 39} of treated and untreated NPLs may shed further light on the microscopic nature of the defects responsible for the various distinct non-radiative pathways. Our approach of combining picosecond streak camera and TCSPC measurements provides a platform to disentangle and understand radiative and non-radiative processes in luminescent materials, which serves as input for the rational design of highly emissive nanomaterials with unity PLQY.

5.4 Conclusions

We have elucidated the non-radiative processes in CsPbBr₃ nanoplatelets by probing the excited-state dynamics with a combination of photoluminescence streak camera and TCSPC measurements. This combination of spectroscopic techniques allowed us to probe the excited-state dynamics of CsPbBr₃ nanoplatelets over six orders of magnitude in time. We have found that chemical treatment with PbBr₂ suppresses the non-radiative processes associated with charge-carrier trapping from the lowest-energy

exciton state and therefore enhances the prompt emission. The dark fraction of NPLs—the nonemissive subpopulation of nanocrystals within the ensemble—is unaffected by the chemical treatment with PbBr_2 . Furthermore, we find that the contribution of delayed emission due to trapping–de-trapping events to the total emission decreases upon surface treatment. This is consistent with a reduction of band-edge trapping and non-radiative recombination. We have identified charge-carrier trapping processes that limit the PLQY (non-radiative recombination) and those that do not (delayed emission). Furthermore, using the definition of quantum yield density provides a framework to test and optimize synthesis procedures or post-synthetic chemical treatments on a variety of fluorescent nanocrystals.

5.5 Acknowledgements

This chapter is based on a collaboration with Utrecht University. I want to thank Ward van der Stam, Sander Vonk and Freddy Rabouw especially for their large input into this chapter. Ward van der Stam prepared all the materials investigated and Sander Vonk and Freddy Rabouw did the nanosecond time-correlated single-photon counting measurements as well as performing large parts of the analysis.

5

References

1. Becker, M. A.; Vaxenburg, R.; Nedelcu, G.; Sercel, P. C.; Shabaev, A.; Mehl, M. J.; Michopoulos, J. G.; Lambrakos, S. G.; Bernstein, N.; Lyons, J. L.; Stöferle, T.; Mahrt, R. F.; Kovalenko, M. V.; Norris, D. J.; Rainò, G.; Efros, A. L., Bright Triplet Excitons in Caesium Lead Halide Perovskites. *Nature* 2018, 553 (7687), 189-193.
2. Utzat, H.; Sun, W.; Kaplan, A. E. K.; Krieg, F.; Ginterseder, M.; Spokoyny, B.; Klein, N. D.; Shulenberg, K. E.; Perkinson, C. F.; Kovalenko, M. V.; Bawendi, M. G., Coherent Single-Photon Emission from Colloidal Lead Halide Perovskite Quantum Dots. *Science* 2019, 363 (6431), 1068-1072.
3. Bodnarchuk, M. I.; Boehme, S. C.; ten Brinck, S.; Bernasconi, C.; Shynkarenko, Y.; Krieg, F.; Widmer, R.; Aeschlimann, B.; Günther, D.; Kovalenko, M. V.; Infante, I., Rationalizing and Controlling the Surface Structure and Electronic Passivation of Cesium Lead Halide Nanocrystals. *ACS Energy Lett.* 2019, 4 (1), 63-74.
4. Kovalenko, M. V.; Protesescu, L.; Bodnarchuk, M. I., Properties and Potential Optoelectronic Applications of Lead Halide Perovskite Nanocrystals. *Science* 2017, 358 (6364), 745-750.
5. Protesescu, L.; Yakunin, S.; Bodnarchuk, M. I.; Krieg, F.; Caputo, R.; Hendon, C. H.; Yang, R. X.; Walsh, A.; Kovalenko, M. V., Nanocrystals of Cesium Lead Halide Perovskites (CsPbX_3 , $X = \text{Cl, Br, and I}$): Novel Optoelectronic Materials Showing Bright Emission with Wide Color Gamut. *Nano Lett.* 2015, 15 (6), 3692-3696.
6. Akkerman, Q. A.; Rainò, G.; Kovalenko, M. V.; Manna, L., Genesis, Challenges and Opportunities for Colloidal Lead Halide Perovskite Nanocrystals. *Nat. Mater.* 2018, 17 (5), 394-405.

7. Swarnkar, A.; Ravi, V. K.; Nag, A., Beyond Colloidal Cesium Lead Halide Perovskite Nanocrystals: Analogous Metal Halides and Doping. *ACS Energy Lett.* 2017, 2 (5), 1089-1098.
8. Koscher, B. A.; Bronstein, N. D.; Olshansky, J. H.; Bekenstein, Y.; Alivisatos, A. P., Surface- vs Diffusion-Limited Mechanisms of Anion Exchange in CsPbBr₃ Nanocrystal Cubes Revealed through Kinetic Studies. *J. Am. Chem. Soc.* 2016, 138 (37), 12065-12068.
9. Yu, Y.; Zhang, D.; Kisielowski, C.; Dou, L.; Kornienko, N.; Bekenstein, Y.; Wong, A. B.; Alivisatos, A. P.; Yang, P., Atomic Resolution Imaging of Halide Perovskites. *Nano Lett.* 2016, 16 (12), 7530-7535.
10. Creutz, S. E.; Crites, E. N.; De Siena, M. C.; Gamelin, D. R., Anion Exchange in Cesium Lead Halide Perovskite Nanocrystals and Thin Films Using Trimethylsilyl Halide Reagents. *Chem. Mater.* 2018, 30 (15), 4887-4891.
11. Tong, Y.; Bladt, E.; Aygüler, M. F.; Manzi, A.; Milowska, K. Z.; Hintermayr, V. A.; Docampo, P.; Bals, S.; Urban, A. S.; Polavarapu, L.; Feldmann, J., Highly Luminescent Cesium Lead Halide Perovskite Nanocrystals with Tunable Composition and Thickness by Ultrasonication. *Angew. Chem. Int. Ed.* 2016, 55 (44), 13887-13892.
12. Nedelcu, G.; Protesescu, L.; Yakunin, S.; Bodnarchuk, M. I.; Grotevent, M. J.; Kovalenko, M. V., Fast Anion-Exchange in Highly Luminescent Nanocrystals of Cesium Lead Halide Perovskites (CsPbX₃, X = Cl, Br, I). *Nano Lett.* 2015, 15 (8), 5635-5640.
13. Brandt, R. E.; Poindexter, J. R.; Gorai, P.; Kurchin, R. C.; Hoyer, R. L. Z.; Nienhaus, L.; Wilson, M. W. B.; Polizzotti, J. A.; Sereika, R.; Žaltauskas, R.; Lee, L. C.; MacManus-Driscoll, J. L.; Bawendi, M.; Stevanović, V.; Buonassisi, T., Searching for “Defect-Tolerant” Photovoltaic Materials: Combined Theoretical and Experimental Screening. *Chem. Mater.* 2017, 29 (11), 4667-4674.
14. Houtepen, A. J.; Hens, Z.; Owen, J. S.; Infante, I., On the Origin of Surface Traps in Colloidal II–VI Semiconductor Nanocrystals. *Chem. Mater.* 2017, 29 (2), 752-761.
15. Kirkwood, N.; Monchen, J. O. V.; Crisp, R. W.; Grimaldi, G.; Bergstein, H. A. C.; du Fossé, I.; van der Stam, W.; Infante, I.; Houtepen, A. J., Finding and Fixing Traps in II–VI and III–V Colloidal Quantum Dots: The Importance of Z-Type Ligand Passivation. *J. Am. Chem. Soc.* 2018, 140 (46), 15712-15723.
16. van der Stam, W.; du Fossé, I.; Grimaldi, G.; Monchen, J. O. V.; Kirkwood, N.; Houtepen, A. J., Spectroelectrochemical Signatures of Surface Trap Passivation on CdTe Nanocrystals. *Chem. Mater.* 2018, 30 (21), 8052-8061.
17. Krieg, F.; Ochsenbein, S. T.; Yakunin, S.; ten Brinck, S.; Aellen, P.; Süess, A.; Clerc, B.; Guggisberg, D.; Nazarenko, O.; Shynkarenko, Y.; Kumar, S.; Shih, C.-J.; Infante, I.; Kovalenko, M. V., Colloidal CsPbX₃ (X = Cl, Br, I) Nanocrystals 2.0: Zwitterionic Capping Ligands for Improved Durability and Stability. *ACS Energy Lett.* 2018, 3 (3), 641-646.
18. Bohn, B. J.; Tong, Y.; Gramlich, M.; Lai, M. L.; Döblinger, M.; Wang, K.; Hoyer, R. L. Z.; Müller-Buschbaum, P.; Stranks, S. D.; Urban, A. S.; Polavarapu, L.; Feldmann, J., Boosting Tunable Blue Luminescence of Halide Perovskite Nanoplatelets through Postsynthetic Surface Trap Repair. *Nano Lett.* 2018, 18 (8), 5231-5238.

19. Liu, F.; Zhang, Y.; Ding, C.; Kobayashi, S.; Izuishi, T.; Nakazawa, N.; Toyoda, T.; Ohta, T.; Hayase, S.; Minemoto, T.; Yoshino, K.; Dai, S.; Shen, Q., Highly Luminescent Phase-Stable CsPbI₃ Perovskite Quantum Dots Achieving Near 100% Absolute Photoluminescence Quantum Yield. *ACS Nano* 2017, 11 (10), 10373-10383.
20. Dutta, A.; Behera, R. K.; Pal, P.; Baitalik, S.; Pradhan, N., Near-Unity Photoluminescence Quantum Efficiency for All CsPbX₃ (X=Cl, Br, and I) Perovskite Nanocrystals: A Generic Synthesis Approach. *Angew. Chem. Int. Ed.* 2019, 58 (17), 5552-5556.
21. Pradhan, N., Journey of Making Cesium Lead Halide Perovskite Nanocrystals: What's Next. *J. Phys. Chem. Lett.* 2019, 10 (19), 5847-5855.
22. Wang, Y.; Zhi, M.; Chang, Y.-Q.; Zhang, J.-P.; Chan, Y., Stable, Ultralow Threshold Amplified Spontaneous Emission from CsPbBr₃ Nanoparticles Exhibiting Trion Gain. *Nano Lett.* 2018, 18 (8), 4976-4984.
23. De Roo, J.; Ibáñez, M.; Geiregat, P.; Nedelcu, G.; Walravens, W.; Maes, J.; Martins, J. C.; Van Driessche, I.; Kovalenko, M. V.; Hens, Z., Highly Dynamic Ligand Binding and Light Absorption Coefficient of Cesium Lead Bromide Perovskite Nanocrystals. *ACS Nano* 2016, 10 (2), 2071-2081.
24. Maes, J.; Balcaen, L.; Drijvers, E.; Zhao, Q.; De Roo, J.; Vantomme, A.; Vanhaecke, F.; Geiregat, P.; Hens, Z., Light Absorption Coefficient of CsPbBr₃ Perovskite Nanocrystals. *J. Phys. Chem. Lett.* 2018, 9 (11), 3093-3097.
25. Vale, B. R. C.; Socie, E.; Burgos-Caminal, A.; Bettini, J.; Schiavon, M. A.; Moser, J.-E., Exciton, Biexciton, and Hot Exciton Dynamics in CsPbBr₃ Colloidal Nanoplatelets. *J. Phys. Chem. Lett.* 2020, 11 (2), 387-394.
26. Henderson, B.; Imbusch, G. F., *Optical spectroscopy of inorganic solids*. Clarendon Press: Oxford 1989.
27. van der Stam, W.; Geuchies, J. J.; Altantzis, T.; van den Bos, K. H. W.; Meeldijk, J. D.; Van Aert, S.; Bals, S.; Vanmaekelbergh, D.; de Mello Donega, C., Highly Emissive Divalent-Ion-Doped Colloidal CsPb_{1-x}MxBr₃ Perovskite Nanocrystals through Cation Exchange. *J. Am. Chem. Soc.* 2017, 139 (11), 4087-4097.
28. Wang, Y.; Zhi, M.; Chan, Y., Delayed Exciton Formation Involving Energetically Shallow Trap States in Colloidal CsPbBr₃ Quantum Dots. *J. Phys. Chem. C* 2017, 121 (51), 28498-28505.
29. Rainò, G.; Becker, M. A.; Bodnarchuk, M. I.; Mahrt, R. F.; Kovalenko, M. V.; Stöferle, T., Superfluorescence from Lead Halide Perovskite Quantum Dot Superlattices. *Nature* 2018, 563 (7733), 671-675.
30. Chirvony, V. S.; González-Carrero, S.; Suárez, I.; Galian, R. E.; Sessolo, M.; Bolink, H. J.; Martínez-Pastor, J. P.; Pérez-Prieto, J., Delayed Luminescence in Lead Halide Perovskite Nanocrystals. *J. Phys. Chem. C* 2017, 121 (24), 13381-13390.
31. Whitham, P. J.; Knowles, K. E.; Reid, P. J.; Gamelin, D. R., Photoluminescence Blinking and Reversible Electron Trapping in Copper-Doped CdSe Nanocrystals. *Nano Lett.* 2015, 15 (6), 4045-4051.
32. Marchioro, A.; Whitham, P. J.; Nelson, H. D.; De Siena, M. C.; Knowles, K. E.; Polinger, V. Z.; Reid, P. J.; Gamelin, D. R., Strong Dependence of Quantum-Dot Delayed Luminescence on Excitation Pulse Width. *J. Phys. Chem. Lett.* 2017, 8 (17), 3997-4003.

33. Rabouw, F. T.; Kamp, M.; van Dijk-Moes, R. J. A.; Gamelin, D. R.; Koenderink, A. F.; Meijerink, A.; Vanmaekelbergh, D., Delayed Exciton Emission and Its Relation to Blinking in CdSe Quantum Dots. *Nano Lett.* 2015, 15 (11), 7718-7725.
34. Durisic, N.; Godin, A. G.; Walters, D.; Grütter, P.; Wiseman, P. W.; Heyes, C. D., Probing the “Dark” Fraction of Core–Shell Quantum Dots by Ensemble and Single Particle pH-Dependent Spectroscopy. *ACS Nano* 2011, 5 (11), 9062-9073.
35. Hinsch, A.; Lohmann, S.-H.; Strelow, C.; Kipp, T.; Würth, C.; Geißler, D.; Kornowski, A.; Wolter, C.; Weller, H.; Resch-Genger, U.; Mews, A., Fluorescence Quantum Yield and Single-Particle Emission of CdSe Dot/CdS Rod Nanocrystals. *J. Phys. Chem. C* 2019, 123 (39), 24338-24346.
36. Ebenstein, Y.; Mokari, T.; Banin, U., Fluorescence Quantum Yield of CdSe/ZnS Nanocrystals Investigated by Correlated Atomic-Force and Single-Particle Fluorescence Microscopy. *Appl. Phys. Lett.* 2002, 80 (21), 4033-4035.
37. Würth, C.; Geißler, D.; Behnke, T.; Kaiser, M.; Resch-Genger, U., Critical Review of the Determination of Photoluminescence Quantum Yields of Luminescent Reporters. *Anal. Bioanal. Chem.* 2015, 407 (1), 59-78.
38. Fu, M.; Tamarat, P.; Trebbia, J.-B.; Bodnarchuk, M. I.; Kovalenko, M. V.; Even, J.; Lounis, B., Unraveling Exciton–Phonon Coupling in Individual FAPbI₃ Nanocrystals Emitting Near-Infrared Single Photons. *Nat. Commun.* 2018, 9 (1), 3318.
39. Orfield, N. J.; McBride, J. R.; Keene, J. D.; Davis, L. M.; Rosenthal, S. J., Correlation of Atomic Structure and Photoluminescence of the Same Quantum Dot: Pinpointing Surface and Internal Defects That Inhibit Photoluminescence. *ACS Nano* 2015, 9 (1), 831-839.
40. Chen, J.; Messing, M. E.; Zheng, K.; Pullerits, T., Cation-Dependent Hot Carrier Cooling in Halide Perovskite Nanocrystals. *J. Am. Chem. Soc.* 2019, 141 (8), 3532-3540.

Appendix

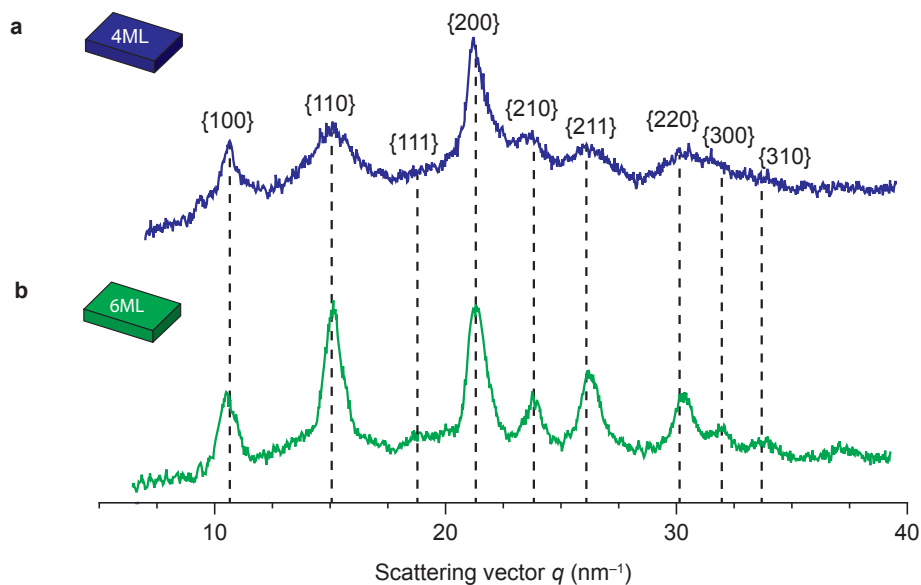


Figure A5.1 X-ray diffraction of CsPbBr₃ nanoplatelets. X-ray diffraction pattern of (a) 4ML and (b) 6ML NPLs. The dashed lines show the characteristic lattice planes of a cubic perovskite crystal structure with a lattice constant $a = 5.897 \text{ \AA}$.²⁷

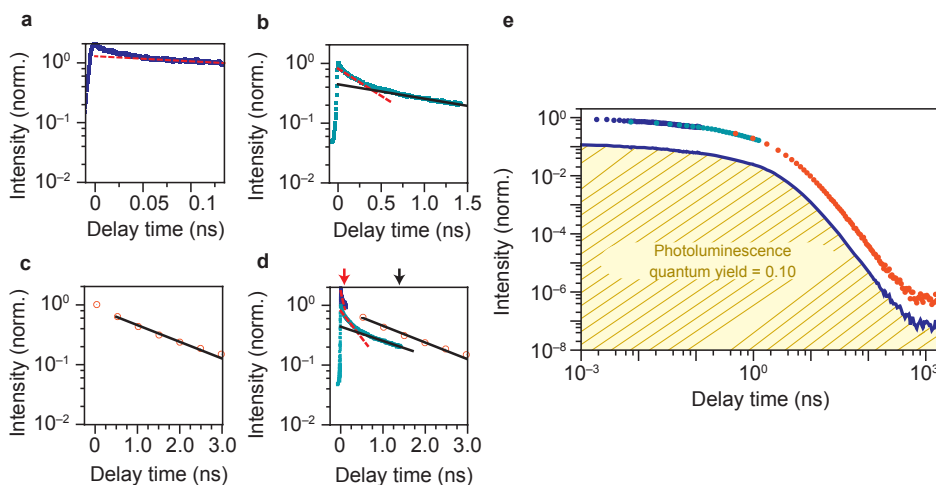


Figure A5.2 Stitching of streak camera and TCSPC measurements. (a) The high-resolution streak camera measurement was fitted to a single-exponential function $A(t)$ (red, dashed) for delay times $t > 75$ ps. (b) The low-resolution streak camera measurement was fitted to a single-exponential function on the domain $0.1 \text{ ns} < t < 0.18 \text{ ns}$ (red, dashed) and to a second single-exponential function $C(t)$ on the domain $t > 0.7 \text{ ns}$ (black). (c) The TCSPC measurement was fitted to a single-exponential function $D(t)$ on the domain $0.5 \text{ ns} < t < 3 \text{ ns}$. (d) We stitch the three measurements together by adjusting the relative intensity scales such that $A(133 \text{ ps}) = B(133 \text{ ps})$ (red arrow) and $C(1.43 \text{ ns}) = D(1.43 \text{ ns})$ (black arrow). (e) The stitching procedure yields the total decay curve ranging from the ps timescale of the streak camera to the μs timescale of the TCSPC measurement. To obtain the quantum yield density $\phi(t)$ we normalized the total area under the decay curve to the PLQY of the nanoplatelet samples.

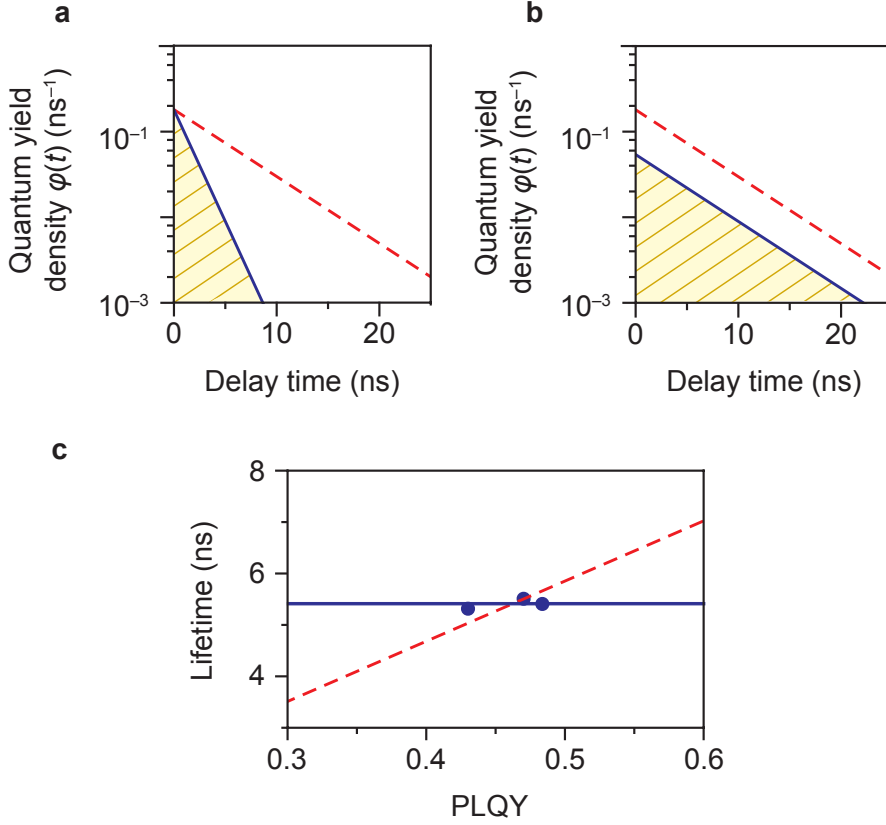


Figure A5.3 The dark fraction and determination of the radiative rate. Here, we consider two scenarios in which a sample of emitters, e.g. perovskite nanoplatelets, have non-unity PLQY but a quantum yield density $\phi(t)$ that is qualitatively different. (a) The first scenario we consider is a sample in which all emitters are identical. The quantum yield density is given by

$$\phi(t) = k_{\text{rad}} e^{-(k_{\text{rad}} + k_{\text{nr}}^{\text{B}})t}$$

where the amplitude $\phi(0)$ is equal to the radiative rate k_{rad} , the non-radiative rate of the bright fraction is k_{nr}^{B} and the PLQY is equal to $k_{\text{rad}}/(k_{\text{rad}} + k_{\text{nr}}^{\text{B}})$. The red dashed line shows the quantum yield density for a unity PLQY sample based on a radiative rate $k_{\text{rad}} = 0.18 \text{ ns}^{-1}$ and $k_{\text{nr}}^{\text{B}} = 0 \text{ ns}^{-1}$. A decrease of the PLQY (blue, $k_{\text{nr}}^{\text{B}} = 0.42 \text{ ns}^{-1}$ and PLQY = 0.3) in this scenario will make the excited-state dynamics faster but the amplitude is unchanged. (b) The second scenario is a sample in which we have two subpopulations, one with unity PLQY ($k_{\text{nr}}^{\text{B}} = 0 \text{ ns}^{-1}$) called the bright fraction and one with zero PLQY called the dark fraction. We can write the quantum yield density as

$$\phi(t) = f k_{\text{rad}} e^{-k_{\text{rad}} t} + (1 - f) k_{\text{rad}} e^{-(k_{\text{rad}} + k_{\text{nr}}^{\text{D}})t}$$

where f is the bright fraction and the PLQY equals the bright fraction f . The excited-state dynamics of the dark fraction are completely masked by the instrument response function (IRF) of the TCSPC and streak camera measurements because $k_{\text{nr}}^{\text{D}} \gg k_{\text{rad}}$, τ_{IRF}^{-1} which effectively lowers the amplitude of the quantum yield density to $\phi(0) = f k_{\text{rad}}$. The red dashed line shows the quantum yield density of a unity-PLQY sample based on a radiative rate $k_{\text{rad}} = 0.18 \text{ ns}^{-1}$ and $f = 1$. Here, a decrease of the PLQY (blue,

$f = 0.3$) corresponds to an increase of the dark fraction which lowers the amplitude of the quantum yield density. (c) To verify which of the scenarios describe our nanoplatelet samples we measured the lifetimes for three independently synthesized 4-monolayer nanoplatelet samples. The samples are nominally the same but differ slightly in PLQY. Based on the assumption that we have a dark fraction of nanoplatelets we expect that the measured lifetime $\tau = 1/k_{\text{rad}}$ is constant (blue) for the three samples and the PLQY is different only because of sample-to-sample variations of the bright fraction f . If we assumed one population of imperfect nanoplatelets, the $\text{PLQY} = k_{\text{rad}} \tau$ would scale linearly (red, dashed) with the radiative rate. We observe that the lifetime is constant with different PLQY and therefore we assign the non-unity PLQY to the presence of a dark fraction which lowers the PLQY and identify the fitted decay rate $k_{\text{rad}} = 0.18 \text{ ns}^{-1}$ as the radiative decay rate.

Delayed emission mechanisms with varying non-radiative rates

Temporary storage and release of excitonic charge carriers can result in photon emission with a relatively long delay time compared to direct radiative emission. From the quantum yield density $\phi(t)$ we observe slower and faster dynamics with respect to radiative recombination. These observations can be explained by two qualitatively different delayed-emission mechanisms. The first scenario is [1] hot-carrier trapping where one of the charge carriers is trapped from a hot-exciton state. The second mechanism is [2] cold-carrier trapping where the exciton cools down to the lowest-energy exciton state before a charge carrier is trapped. Here, we will discuss the influence of a chemical treatment—which changes the non-radiative processes—on the fraction of delayed emission to reveal the predominant delayed-emission mechanism in perovskite nanoplatelets. We will assume that radiative recombination from a stored charge carrier does not occur in our samples, because no trap-state emission is observed in the emission spectra (Figure 5.2c–d).

[1] In the scenario of hot-carrier trapping (Figure A5.4a) the trapping rate $k_{\text{trap}}^{\text{hot}}$ is in competition with hot-exciton cooling k_c . The probability that an absorption event leads to delayed emission

$$\eta_{\text{delayed}}^{\text{hot}} = \frac{f k_{\text{rad}}}{k_{\text{rad}} + k_{\text{nr}}} \frac{k_{\text{trap}}^{\text{hot}}}{k_{\text{trap}}^{\text{hot}} + k_c} \quad \text{A5.1}$$

is the product of the probability for hot-carrier trapping and the probability for photon emission after release. Because cooling rates are typically very fast 0.3 ps^{-1} , in this case $k_{\text{trap}}^{\text{hot}}$ must be similarly fast in order to compete with cooling.⁴⁰ The probability that an absorption event leads to prompt emission

$$\eta_{\text{prompt}}^{\text{hot}} = \frac{f k_{\text{rad}}}{k_{\text{rad}} + k_{\text{nr}}} \frac{k_c}{k_{\text{hot,trap}} + k_c} \quad \text{A5.2}$$

is the product of the probability for hot-exciton cooling and the probability for photon emission after cooling. From the two expressions above we observe that lowering of the non-radiative recombination rate k_{nr} increases both $\eta_{\text{prompt}}^{\text{hot}}$ and $\eta_{\text{delayed}}^{\text{hot}}$. However, both decay pathways to the ground state experience the non-radiative quenching only once. Therefore the contribution of delayed photons to the total emission

$$x_{delayed}^{hot} = \frac{\eta_{delayed}^{hot}}{\eta_{prompt}^{hot} + \eta_{delayed}^{hot}} = \frac{k_{trap}^{hot}}{k_{trap}^{hot} + k_c} \quad A5.3$$

is independent of k_{nr} . Figure A5.4b shows the contribution of delayed photons to the total emission before (PLQY = 0.10) and after (PLQY = 0.44) treatment with $PbBr_2$. The constant contribution of delayed photons to the total emission for hot-carrier trapping (red, dashed) does not match the measurements and therefore we exclude hot-carrier trapping as the dominant mechanism underlying delayed emission.

[2] In the scenario of cold-carrier trapping (Figure A5.4c and e) the trapping rate k_{trap}^{cold} is in competition with radiative and non-radiative recombination. The probability that an absorption event leads to prompt emission is

$$\eta_{prompt}^{cold} = \frac{fk_{rad}}{k_{rad} + k_{nr} + k_{trap}^{cold}} \quad A5.4$$

where k_{trap}^{cold} is the trapping rate of cold charge carriers. Similarly, we can define the contribution of delayed emission to the total decay. In this scenario charge carriers can cycle an arbitrary number of times between the trap state and the lowest-energy exciton state. To obtain the total probability for delayed emission we sum over all possible cycles $n \geq 1$ and multiply with the probability that a photon is emitted from the lowest-energy exciton state:

$$\eta_{delayed}^{cold} = \frac{fk_{rad}}{k_{rad} + k_{nr} + k_{trap}^{cold}} \sum_{n=1}^{\infty} \left(\frac{k_{trap}^{cold}}{k_{rad} + k_{nr} + k_{trap}^{cold}} \right)^n \quad A5.5$$

The infinite sum is a geometric series which we can simplify writing $\eta_{delayed}^{cold}$ in terms of all the rates as

$$\eta_{delayed}^{cold} = \frac{fk_{rad}k_{trap}^{cold}}{(k_{rad} + k_{nr} + k_{trap}^{cold})(k_{rad} + k_{nr})} \quad A5.6$$

Using the expressions of the prompt- and delayed-emission probabilities derived above gives the fraction of delayed emission

$$x_{delayed}^{cold} = \frac{\eta_{delayed}^{cold}}{\eta_{prompt}^{cold} + \eta_{delayed}^{cold}} = \frac{k_{trap}^{cold}}{k_{rad} + k_{nr} + k_{trap}^{cold}} \quad A5.7$$

We see that a large trapping rate k_{trap}^{cold} compared to radiative- and non-radiative recombination rates leads to a high fraction of delayed emission. Next, we distinguish between two possibilities of how the treatment affects the non-radiative rates. In the first possibility (Figure A5.4c), we assume that the treatment only affects the non-radiative recombination rate k_{nr} . In the second possibility (Figure A5.4e), we assume that both non-radiative recombination and the trapping rate are affected by the treatment.

[2A] In the first possibility where only non-radiative recombination is affected by the treatment (Figure A5.4c), we can use the relationship between the non-radiative recombination rate and the PLQY

$$PLQY = \frac{fk_{rad}}{k_{rad} + k_{nr}} \quad A5.8$$

to express the contribution of delayed photons to the total emission $x_{delayed}^{cold}$ in terms of the PLQY:

$$x_{delayed}^{cold} = \frac{1}{1 + \frac{fk_{rad}}{PLQYk_{trap}^{cold}}} \quad A5.9$$

In Figure A5.4d we compare equation A5.9 to the experimental relation between PLQY and $x_{delayed}^{cold}$. For a fitted trapping rate of $k_{trap}^{cold} = 5.6 \mu s^{-1}$ we observe an increase of the contribution of delayed photons to the total emission. Therefore we exclude this scenario to contribute to delayed emission.

[2B] In the second possibility for cold-carrier trapping, we assume that both the trapping rate k_{trap}^{cold} and the non-radiative recombination rate k_{nr} change to the same extent, i.e. by the same factor (Figure A5.4e). The contribution of delayed emission to the total emission is given by

$$x_{delayed}^{cold} = \frac{1}{1 + \frac{f}{a(f - PLQY)}} \quad A5.10$$

where a is the ratio between the trapping rate k_{trap}^{cold} and the non-radiative recombination rate k_{nr} . In Figure A5.4f we compare equation A5.10 to the experimental relation between PLQY and $x_{delayed}^{cold}$. For a fitted constant ratio $a = 0.039$ we observe a decrease of the delayed emission fraction as a function of the PLQY consistent with the experiments. We therefore conclude that cold-carrier trapping is the dominant trapping- and release mechanism for excitons in 4- and 6-monolayer perovskite nanoplatelets and that both trap states leading to non-radiative recombination and delayed emission are suppressed by the chemical treatment.

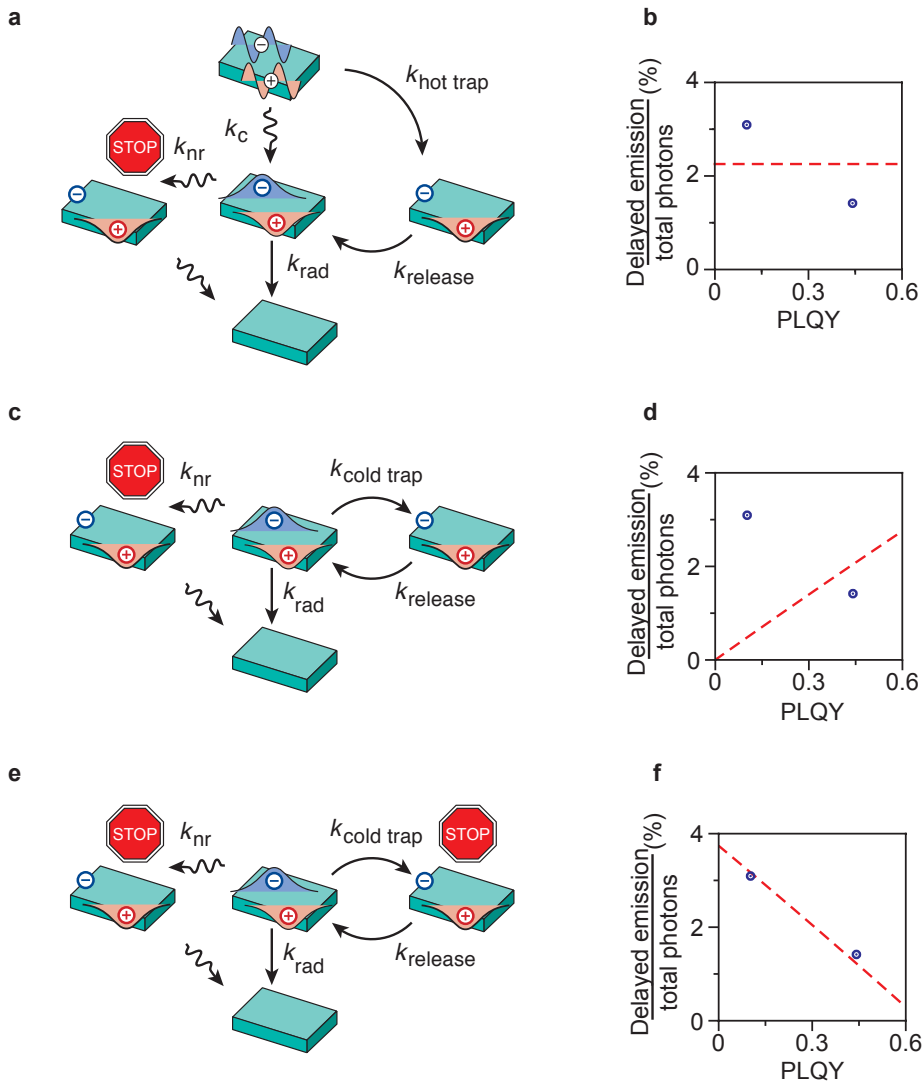


Figure A5.4 Mechanisms for delayed exciton recombination. (a) Scenario [1], in which hot-carrier trapping from a hot-exciton state leads to delayed emission of photons. The treatment suppresses non-radiative recombination from band-edge excitons. (b) Fraction of delayed emission $x_{\text{delayed}}^{\text{hot}}$ for 4-monolayer perovskite nanoplatelet sample before (PLQY = 0.10) and after (PLQY = 0.44) treatment with PbBr_2 . Assuming a constant trapping rate $k_{\text{trap}}^{\text{hot}}$ and varying non-radiative recombination rate k_{nr} (equation A5.3) yields a constant delayed emission fraction as a function of the PLQY. (c) Scenario [2A], in which cold-carrier trapping from a band-edge exciton leads to delayed emission of photons. The treatment suppresses non-radiative recombination from band-edge excitons. (d) Same as b, but now plotting the calculated $x_{\text{delayed}}^{\text{cold}}$ in scenario [2A] (equation A5.9, $k_{\text{trap}}^{\text{cold}} = 5.6 \mu\text{s}^{-1}$). (e) Scenario [2B], in which cold-carrier trapping from a band-edge exciton leads to delayed emission of photons. The treatment suppresses both non-radiative recombination from band-edge excitons as well as non-radiative temporary trapping. (f) Same as b, but now plotting the calculated $x_{\text{delayed}}^{\text{cold}}$ in scenario [2B] (equation A5.10, $a = 0.039$)

Timescale between trapping and emission

To determine the timescale between trapping and emission of a delayed photon we have to solve the rate equations for the population of the excited state $N_E(t)$ and the trap state $N_T(t)$:

$$\dot{N}_E(t) = -(k_{rad} + k_{trap})N_E(t) + k_{rel}N_T(t) \quad A5.11a$$

$$\dot{N}_T(t) = -k_{rel}N_T(t) + k_{trap}N_E(t) \quad A5.11b$$

Here the excited-state population $N_E(t)$ decreases in time due to radiative recombination k_{rad} and trapping k_{trap} and the population increases by release of charge carriers k_{rel} by the trap state. The trap-state population $N_T(t)$ decreases in time by release of charge carriers k_{rel} and increases by trapping k_{trap} . We can calculate expressions for both populations in time assuming that all initial population is in the trap state ($N_E(0)=0$ and $N_T(0)=1$). We obtain the population dynamics of the exciton state

$$N_E(t) = \frac{2k_{rel}e^{-Kt/2} \sinh(\sqrt{K^2 - 4k_{rad}k_{rel}} t/2)}{\sqrt{K^2 - 4k_{rad}k_{rel}}} \quad A5.12$$

where $K=k_{rad}+k_{trap}+k_{rel}$. We can use these dynamics to calculate the average time $\langle \tau \rangle$ for a charge carrier to de-trapped

$$\langle \tau \rangle = \frac{\int_0^\infty t N_E(t) dt}{\int_0^\infty N_E(t) dt} = k_{rad}^{-1} + k_{rel}^{-1} + \frac{k_{trap}}{k_{rad}k_{rel}} \quad A5.13$$

where the average time between trapping and emission is equal to $\langle \tau \rangle = k_{rad}^{-1} + k_{rel}^{-1}$ when we assume that a charge carrier is only trapped once, or $k_{trap} \ll k_{rad}, k_{rel}$.

Summary

During the last decade perovskite materials have rapidly emerged, and are currently among the most promising candidates as materials for solar cells and other opto-electronic applications. Although our knowledge related to these materials has advanced rapidly in last few years there are still many unknown aspects and many challenges remain. These challenges include a solid understanding of the relation between the composition of the materials and their structural and the photophysical processes that occur on charge excitation. In addition, there are many challenges related to the synthesis of pure-phase, defect free materials, the stability in presence of oxygen and water, and the replacement of toxic elements such as lead. In his thesis we try to shine a light on some of these unknown aspects using a combination of computational techniques such as molecular dynamics simulations and experimental techniques measuring photoluminescence. Using molecular dynamics simulations, we study the relation between the composition of the material and the static and dynamic structural properties of the individual parts of the structures. This gives insight into the effect of reduced dimensionality or introduction of aromatic molecules has on the structure. In addition, this also gives new insight in the origin of the low temperature phase transition that occurs in some perovskite materials. Experimentally we look at non-radiative pathways in perovskite nanoplatelets and how we can overcome them. Ultimately, the results presented in this thesis give some new design guidelines for perovskite materials to optimize their properties for specific applications.

In **Chapter 2** we study the cause-effect relationship between the rotation of the small organic cation in three-dimensional perovskites, and the low temperature phase transition that occurs in these materials. This is done for both methylammonium lead iodide and formamidinium lead iodide. In order to achieve this, we perform several model simulations on both materials which differ in the interactions that are taken into account and in the dynamic freedom of the structure. The simulations are performed at various temperatures and for each simulation we track the rotation of the organic molecule, as well as their preferred orientations. For both materials we see, as expected, that the flexibility of the inorganic lead cage plays an important role, where the decreased rate of rotation observed during the phase transition is severely hampered without it. However, even when the inorganic lead-iodide layer is not allowed to deform, we see a slower rotation rate for the organic molecules and that certain orientations of the molecules become favorable at lower temperatures. This happens mostly due to hydrogen bonding between the molecules and the iodides in the inorganic structure although in the case of methylammonium, dipole-dipole interaction also play a role. This indicates that the low-temperature phase transition

occurs due to a subtle interplay between a few factors: Dipole-dipole interactions between the organic cations, specific (hydrogen bonding) interactions between the organic cation and the lead-iodide lattice, and deformation of the lead-iodide lattice in reaction to the reduced rotational motion of the organic cations.

In **Chapter 3** we turn our attention to two-dimensional perovskite materials with methylammonium as the small organic cation and n-butylammonium as the large organic cation. We have performed molecular dynamics simulation with a varying number of inorganic layers ranging from $n = 1$ to $n = 4$ at temperatures ranging from 50 K to 300 K. Our simulations show that changing the number of inorganic layers has a large effect on the structure and dynamics of both the inorganic and the organic part of the material. Some of these effects are predictable, such as increased rigidity of the inorganic layers in the material when the number of inorganic layers grows. Other effects are more surprising, for instance a low temperature phase transition with clear octahedral tilting is observed for some of the materials, but not all. Furthermore, this octahedral tilting affects the rotational freedom of the methylammonium ion negatively for some materials but positively for others.

The attention stays on two-dimensional perovskite materials in **Chapter 4** where we study single layer perovskite structures ($n = 1$) with varying large organic cations to gain insight in the relation between the intermolecular interactions in the organic and the inorganic parts of the material. The large organic cations studied are n-butylammonium, phenylethylammonium and pyrene-o-butylammonium. These organic cations differ both in aromaticity and in the length of the flexible linker that connects the ammonium group to the remainder of the molecule. As in previous chapters, the approach of choice is classical molecular dynamics simulation performed at a range of temperatures. The results show that both the aromaticity and the length of the flexible linker have a substantial effect on the structure and dynamics of the materials. The introduction of an aromatic part results in a more rigid organic layer. In the case of a short flexible linker consisting of an ethyl bridge, this increased rigidity is transmitted to the inorganic framework. Expanding the alkyl linker to a butyl is shown to introduce enough flexibility so that the effect of the strongly interacting aromatic units is not transmitted to the inorganic layer. This highlights the importance of the nature of the organic cation when designing a two-dimensional perovskite.

With previous chapters all revolving around computational simulations on either three- or two-dimensional perovskites, in **Chapter 5** the attention switches to the photophysical properties. In this chapter we experimentally investigate the non-radiative charge-carrier decay channels in CsPbBr_3 perovskite nanoplatelets with and without additional chemical treatment by PbBr_2 . These nanoplatelets are two-dimensional perovskite materials but differ from the ones previously discussed in several ways. Instead of an organic cation (methylammonium or formamidinium) there is a cesium, bromide is used instead of iodide and instead of free large organic cations there are stabilizing organic surface ligands consisting of a mixture of oleic acid and oleylamine. The photoinduced emission from these nanoplatelets is studied by a combination of picosecond streak camera measurements and nanosecond time-correlated single-photon counting measurements.

This combination allows us to study the photoluminescence from the platelets over six orders of magnitudes in time. From these measurements we conclude that 40% of the nanoplatelets are nonfluorescent and cannot be turned fluorescent through chemical treatment. The remainder of the nanoplatelets show fluorescence but charge-carrier trapping occurs, leading to emission losses. This trapping can be partially prevented by the chemical treatment. Interestingly, even without chemical treatment, some emission losses due to trapping are mitigated because trapped carriers spontaneously de-trap on nanosecond-to-microsecond timescales. This shows that there are multiple non-radiative pathways in these nanoplatelets and furthermore shows the advantages of using multiple techniques that cover a wide time-range when investigating processes such as this.

Samenvatting

Gedurende de afgelopen tien jaar hebben perovskiet-materialen zich erg snel ontwikkeld en ze behoren momenteel tot de meest veelbelovende nieuwe materialen voor zonnecellen en andere opto-elektronische toepassingen. Hoewel de kennis met betrekking tot deze materialen de afgelopen jaren snel is gegroeid zijn er nog veel onbekende aspecten en er blijven veel uitdagingen. Een van deze uitdagingen is een gedegen begrip van de relatie tussen de samenstelling van de materialen en hun structurele en fotofysische processen die plaatsvinden bij ladingsexcitatie. Bovendien zijn er veel uitdagingen met betrekking tot de synthese van materialen in een pure fase, het voorkomen van defecten, de stabiliteit in aanwezigheid van zuurstof en water, en de vervanging van giftige elementen zoals lood. In dit proefschrift proberen we een aantal van deze onbekende aspecten op te helderen met behulp van een combinatie van computationele technieken zoals moleculaire dynamica simulaties en experimentele technieken om fotoluminescentie te meten. Met behulp van moleculaire dynamica simulaties bestuderen we de relatie tussen de samenstelling van het materiaal en de statische en dynamische structurele eigenschappen van de afzonderlijke delen van de materialen. Dit geeft inzicht in het effect van de dimensionaliteit van de materialen of van de introductie van aromatische moleculen op de structuur. Daarnaast geeft dit ook nieuw inzicht in de structurele faseovergang die optreedt bij sommige perovskietmaterialen bij lage temperatuur. Experimenteel kijken we naar niet-stralende vervalprocessen in zogenaamde perovskiet nanoplatelets en exploreren we hoe deze vervalprocessen kunnen worden overwonnen. Uiteindelijk leiden de resultaten die in dit proefschrift worden gepresenteerd enkele nieuwe ontwerprichtlijnen voor perovskietmaterialen om hun eigenschappen voor specifieke toepassingen te optimaliseren.

In **Hoofdstuk 2** beschouwen we de relatie tussen de oorzaak en het gevolg van het effect van rotatie van het kleine organische kation in driedimensionale perovskieten op de faseovergang bij lage temperatuur die optreedt in deze materialen. Dit doen we voor zowel methylammoniumloodjodide als formamidiniumloodjodide. Om dit te bewerkstelligen, zijn een aantal modelsimulaties uitgevoerd, waarbij verschillende interacties en verschillende vrijheidsgraden worden meegenomen. De simulaties zijn uitgevoerd bij een aantal verschillende temperaturen en voor elke simulatie volgen we de rotatiesnelheid van het organische molecuul, evenals de voorkeursoriëntaties. Voor beide materialen zien we, zoals verwacht, dat de flexibiliteit van het anorganische loodjodide rooster een belangrijke rol speelt. Hierbij blijkt dat de verminderde rotatiesnelheid van het organische die wordt waargenomen tijdens de faseovergang een stuk minder is voor

een rigide loodjodide structuur, in vergelijking met een flexibele structuur. Echter, zelfs als de anorganische lood-jodide laag volledig rigide is wordt een lagere rotatiesnelheid voor de organische moleculen waargenomen. Hierbij zijn er ook specifieke oriëntaties die bij lagere temperaturen het meest gunstig zijn. Dit gebeurt voornamelijk door de vorming van waterstofbruggen tussen de moleculen en de jodide-ionen in de anorganische structuur, hoewel in het geval van methylammonium ook dipool-dipool-interactie tussen de organische kationen een rol speelt. Dit laat zien dat de faseovergang die bij lage temperaturen optreedt een gevolg is van een subtiel samenspel tussen een aantal factoren: de dipool-dipool-interacties tussen de organische kationen, specifieke (waterstofbrug) interacties tussen het organische kation en het lood-jodide-rooster, en de vervorming van het loodjodide rooster als reactie op de verminderde rotatiebeweging van de organische kationen.

In **Hoofdstuk 3** richten we onze aandacht op twee-dimensionale perovskietmaterialen met daarin methylammonium als het kleine organische kation en n-butylammonium als het grote organische kation tussen de anorganische lagen. Om de dynamische eigenschappen van deze materialen te bestuderen zijn moleculaire dynamica simulaties uitgevoerd bij temperaturen tussen 50 K en 300 K, waarin het aantal anorganische lagen varieert van $n = 1$ tot $n = 4$. Deze simulaties laten zien dat het aantal loodjodide anorganische lagen tussen de organische lagen een groot effect heeft op de structuur en dynamica van zowel het anorganische als het organische deel van deze materialen. Sommige van deze effecten zijn voorspelbaar, zoals een grotere rigiditeit van de anorganische lagen in het materiaal wanneer het aantal anorganische lagen toeneemt. Andere effecten zijn meer verrassend, zo wordt bijvoorbeeld een faseovergang bij lage temperatuur met een duidelijke octaëdrische kanteling waargenomen voor sommige materialen, maar niet voor alle. Bovendien beïnvloedt deze octaëdrische kanteling de rotatievrijheid van het methylammonium-ion negatief voor sommige materialen, maar positief voor andere.

We blijven kijken naar tweedimensionale perovskietmaterialen in **Hoofdstuk 4** waar perovskietstructuren met één anorganische laag ($n = 1$) worden bekeken voor verschillende grote organische kationen. Dit heeft als doel om inzicht te krijgen in de relatie tussen de intermoleculaire interacties in de organische laag en de structuur en dynamica van de anorganische delen van het materiaal. De grote organische kationen die zijn onderzocht, zijn n-butylammonium, fenylethylammonium en pyreen-o-butylammonium. Deze organische kationen verschillen zowel in aromaticiteit als in de lengte van de flexibele linker tussen de ammoniumgroep en de rest van het molecuul. Net als in voorgaande hoofdstukken wordt gebruik gemaakt van klassieke moleculaire dynamica simulaties die worden uitgevoerd bij verschillende temperaturen. De resultaten laten zien dat zowel de aromaticiteit als de lengte van de flexibele linker een substantieel effect hebben op de structuur en dynamica van de materialen. Het introduceren van een aromatisch deel leidt tot een stijvere organische laag. Wanneer er een korte flexibele linker aanwezig is, bestaande uit een ethylbrug, wordt deze verhoogde stijfheid overgedragen op het anorganische raamwerk. Het uitbreiden van de alkyl linker tot een butyl blijkt voldoende flexibiliteit te introduceren om de overdracht van deze rigiditeit in het organische deel van het materiaal op de anorganische laag te voorkomen. Dit benadrukt het belang van de precieze details van de structuur van het organische kation bij het ontwerpen van een

twee-dimensionale perovskieten.

Waar het in de vorige hoofdstukken steeds ging om computersimulaties van de structuur van, ofwel voor drie- of tweedimensionale perovskieten, verschuiven we in **Hoofdstuk 5** de aandacht naar de fotofysische eigenschappen. In dit hoofdstuk onderzoeken we experimenteel het niet-stralende ladingsverval in CsPbBr_3 perovskiet nano-platelets, met en zonder aanvullende chemische behandeling door PbBr_2 . Deze nanoplatelets zijn tweedimensionale perovskietstructuren, maar ze verschillen van de eerder besproken materialen. In plaats van een organisch kation (methyllumonium of formamidineum) is er een cesium ion in de structuur opgenomen, er wordt bromide gebruikt in plaats van jodide, en in plaats van vrije grote organische kationen zijn er stabiliserende organische oppervlakteliganen bestaande uit een mengsel van oleic acid en oleylamine. De foto-geïnduceerde emissie vanuit deze nanoplatelets wordt bestudeerd door een combinatie van picoseconde streak camerametingen en nanoseconde 'time-correlated single photon counting' metingen. Deze combinatie maakt het mogelijk om de fotoluminescentie van de platelets over zes ordes van grootte in de tijd te bestuderen. Uit deze metingen concluderen we dat 40% van de nanoplatelets niet fluorescerend is en niet fluorescerend kan worden gemaakt door chemische behandeling. De rest van de nanoplatelets vertonen fluorescentie, maar er kan 'trapping' van ladingsdragers optreden, wat tot verliezen leidt. Deze 'trapping' kan gedeeltelijk worden voorkomen door de chemische behandeling. Het is interessant dat een deel van deze emissieverliezen als gevolg van trapping worden beperkt omdat de 'getrapte' ladingen spontaan weer vrijkomen op nanoseconde-tot-microseconde tijdschalen. Dit laat zien dat er meerdere paden zijn voor niet-stralend verval in deze nanoplatelets. Hiernaast worden de voordelen benadrukt van het gebruik van meerdere technieken die samen een zeer breed tijdsbereik hebben bij het onderzoeken van het verval van aangeslagen ladingen in zulke systemen.

List of publications

This thesis is based on the following publications

Maheshwari, S.; Fridriksson, M. B.; Seal, S.; Meyer, J.; Grozema, F. C., The Relation Between Rotational Dynamics of the Organic Cation and Phase Transitions in Hybrid Halide Perovskites. *J. Phys. Chem. C* 2019, 123 (23), 14652-14661;

Vonk, S. J. W.; Fridriksson, M. B.; Hinterding, S. O. M.; Mangnus, M. J. J.; Van Swieten, T. P.; Grozema, F. C.; Rabouw, F. T.; van der Stam, W., Trapping & De-Trapping in Colloidal Perovskite Nanoplatelets: Elucidation and Prevention of Nonradiative Processes through Chemical Treatment *J. Phys. Chem. C* 2020, 124 (14), 8047-8054.

Fridriksson, M. B.; Maheshwari, S.; Grozema, F. C., Structural Dynamics of Two-Dimensional Ruddlesden-Popper Perovskites: A Computational Study. *J. Phys. Chem. C* 2020, 124 (40), 22096–22104

Fridriksson, M. B.; van der Meer, N.; de Haas, J.; Grozema, F. C., Tuning the Structural Rigidity of 2D Ruddlesden-Popper Perovskite Through the Organic Cation. *J. Phys. Chem. C* Accepted for publication.

Other publications

Gélvez-Rueda, M. C.; Fridriksson, M. B.; Dubey, R. K.; Jager, W. F.; van der Stam, W.; Grozema, F. C., Overcoming the exciton binding energy in two-dimensional perovskite nanoplatelets by attachment of conjugated organic chromophores. *Nat. Commun.* 2020, 11 (1), 1901.

Philip, A. M.; Hsu, C. C.; Wei, Z.; Fridriksson, M. B.; Grozema, F. C.; Jager, W. F., Directing charge transfer in perylene based light-harvesting antenna molecules. *J. Chem. Phys* 2020, 153 (14), 144302

Curriculum Vitae

Magnús Borgar Friðriksson was born in Reykjavík, Iceland on the 8th of March 1992. He obtained his Bachelor degree in Chemistry with emphasis on chemical engineering from the University of Iceland in 2014. Thereafter he moved to the Netherlands and enrolled in a Master program in chemical engineering in Delft University of Technology. He graduated with cum laude in 2016 with a thesis titled Orientation of Methylammonium Ions in Methylammonium Lead Iodide Perovskite and their Effect on the Electronic Structure under the supervision of Dr. Ferdinand Grozema.



Afterwards Magnús started as a PhD student in the group of Dr. Ferdinand Grozema. There he specialized in molecular simulations and spectroscopy on perovskite semiconductors. Along with his studies he has been actively involved in developing and teaching the course Numerieke Technieken that teaches python programming and numerical techniques to 3rd year bachelor students.

In his spare time Magnús is an avid sport fan, with especial love for football. He is a keen runner and is the co-founder of the running group JACO that is composed of people working at the chemical engineering department at Delft University of Technology and has a weekly Wednesday run.